2018

Mechanistic Contributions To Geomorphic Changes Of State

Dylan Bentley Lee

University of Pennsylvania, dylanlee@sas.upenn.edu

Mechanistic Contributions To Geomorphic Changes Of State

Abstract

Transitions abound in geomorphology. Be it the transition from static to dynamic or the shift in a dune field from one dune morphology to another, many questions involve changes of state. This dissertation empirically studies state changes over three scales with an emphasis placed on contributing mechanical factors. First, we examine the transition from static to dynamic at the grain scale in bedload transport (hopping, rolling, and skipping of grains along a riverbed). Transport of grains is continuous at high rates but becomes unpredictable near the threshold of motion. Results show that this unpredictability is similar to how avalanches occur in a sandpile. Transport events are similar in size and merge as transport increases. Grain displacement in the system appears governed by mobile grain-bed kinetic energy exchange. Next, we study the static to dynamic transition at the scale of many grains by examining how soil mechanical properties influence the threshold of motion. Sandbed experiments indicate that, when moisture is the primary variable, shear strength is proportional to the threshold of motion. Finally, we examine a landscape scale pattern transition that arises from the physics of sediment transport interacting with vegetation in a dune field. The onset of vegetation destroys a fluid instability that is fundamental for maintaining the dune pattern prevalent in the dune fields center. Plants destroy the mechanism maintaining the dune field pattern which helps give rise to a qualitative shift in dune morphology. This work highlights the continued relevance of physically informed experiments and field studies for understanding geomorphic transitions from the grain to the landscape scale.

Degree Type
Dissertation

Degree Name
Doctor of Philosophy (PhD)

Graduate Group
Earth & Environmental Science

First Advisor
Douglas J. Jerolmack

Keywords
bed load, dunes, intermittency, robotic platform, sediment transport

Subject Categories
Geology | Geomorphology

MECHANISTIC CONTRIBUTIONS TO GEOMORPHIC CHANGES OF STATE

Dylan Bentley Lee

A DISSERTATION

in

Earth and Environmental Science

Presented to the Faculties of the University of Pennsylvania

in

Partial Fulfillment of the Requirements for the

Degree of Doctor of Philosophy

2018

Supervisor of Dissertation

_____

Douglas J. Jerolmack
Associate Professor, Earth and Environmental Science

Graduate Group Chairperson

_____

David L. Goldsby
Associate Professor, Earth and Environmental Science

Dissertation Committee

Paulo E. Arratia, Professor, Mechanical Engineering and Applied Mechanics

David L. Goldsby, Associate Professor, Earth and Environmental Science

Ileana Pérez-Rodríguez, Assistant Professor, Earth and Environmental Science

MECHANISTIC CONTRIBUTIONS TO GEOMORPHIC CHANGES OF STATE

Dedicated to Clare Specht and Bethany Teigen

ACKNOWLEDGEMENTS

Throughout the past five years Doug has constantly made fun of my 'monotone style.' Yet despite this, reflecting on the support I've received over this long process leaves me feeling anything but neutral. I'm deeply grateful to all of the people who have made my doctoral work possible and would like to extend thanks to those mentioned below as well as others I have been unable to list.

I would like to thank all of my fellow graduate students, colleagues, and the friends I've made during my stay in Philadelphia. I thank Liz Coward, Nicole Khan, Chris Thom, Tina Dura, Brandon Hendrick, Vanessa Boschi, Rachel Valleta, Maddie Stone, Bing Xu, John Sime, Travis Hager, Tierra Moore, Emma Harrison, Steven Jasinski, Erynn Johnson, Mike OShea, and Priya Sharma. Special thanks to Aja Carter for having the courage to be my most immediate office mate. I Thank Gille Brocard for his friendship, scientific advice, and zest for life. During my time in Philadelphia I have also been fortunate enough to meet many amazing people. I thank Pat George and the entire Zen Center of Philadelphia for helping me keep practicing. I thank Thom Bartlett for helping me stay sane. I thank Kael Dougherty. I thank Bethany Teigan for being there even when I'm at my most incorrigible. I couldn't have done it without her.

Joan Buccili, Arlene Mand and Audrey Caputa have helped tremendously in navigating the logistical complexities of graduate life at Penn. As graduate group coordinator, Joan's generosity and compassion has always amazed me. I would also like to thank Jason Seta, Rebecca Perry, Dawn Sabella, and Gus Hartman in the business office for helping me with purchasing. I thank Buddy Borders for his help and advice in the machine shop.

I would like to thank my committee for their valuable feedback and guidance as well as making the time to read this dissertation. David Goldsby has been a steadfast, light-humored presence whose outlook and perspective on life and experimental science remains refreshing. Paolo Arratia provided me with many suggestions for analysis that ultimately

many others. I would especially like to thank Dr. James Channell. He was my original scientific role model and I will always be grateful for his patience, the help he gave me, and the lessons he taught me.

I would like to thank my family for their continued support. Our love may not always be perfect, but that would be boring anyway. My sisters Madison, Noah, and Corrin mean the world to me and I am a lucky brother to have them in my life. I would like to thank Noah for putting up with me during that late night drive. I'm sorry I snapped. I was fortunate to have Pam Majors and Mimi in my life. I still miss both of them. I thank Edward and Anne Lee for all of their sacrifice and support. I thank Dad. I thank Robert Powers and Pops. The deepest thanks goes out to my mother. Without her I wouldn't be able to read, much less complete graduate level work. The sacrifice and courage she displayed over the years to provide for her children will always be an inspiration. I want to thank her for everything.

Finally, I would like to thank Doug Jerolmack, my mentor and advisor. Who has been able to combine a large amount of energy with an equally large amount of patience. He is one of the most dynamic individuals I have ever had the pleasure to meet and I will carry the lessons I learned from him for the rest of my life. I still have no idea what science is, but much of what I do know he taught me. Thanks Doug for teaching me how to collect a shitload of data and average the hell out of it.

ABSTRACT

MECHANISTIC CONTRIBUTIONS TO GEOMORPHIC CHANGES OF STATE

Dylan Bentley Lee

Douglas J. Jerolmack

Transitions abound in geomorphology. Be it the transition from static to dynamic or the shift in a dune field from one dune morphology to another, many questions involve changes of state. This dissertation empirically studies state changes over three scales with an emphasis placed on contributing mechanical factors. First, we examine the transition from static to dynamic at the grain scale in bedload transport (hopping, rolling, and skipping of grains along a riverbed). Transport of grains is continuous at high rates but becomes unpredictable near the threshold of motion. Results show that this unpredictability is similar to how avalanches occur in a sandpile. Transport events are similar in size and merge as transport increases. Grain displacement in the system appears governed by mobile grain-bed kinetic energy exchange. Next, we study the static to dynamic transition at the scale of many grains by examining how soil mechanical properties influence the threshold of motion. Sandbed experiments indicate that, when moisture is the primary variable, shear strength is proportional to the threshold of motion. Finally, we examine a landscape scale pattern transition that arises from the physics of sediment transport interacting with vegetation in a dune field. The onset of vegetation destroys a fluid instability that is fundamental for maintaining the dune pattern prevalent in the dune fields center. Plants destroy the mechanism maintaining the dune field pattern which helps give rise to a qualitative shift in dune morphology. This work highlights the continued relevance of physically informed experiments and field studies for understanding geomorphic transitions from the grain to the landscape scale.

TABLE OF CONTENTS

CHAPTER 1 : Introduction

Landscapes are complex systems whose spatial and temporal evolution arises from the multi-scale interaction of tectonics, sediment transport, climate, and biotic factors. One way to conceptualize this evolution is as a system undergoing transitions from one state to another. Here geomorphic state is defined generally as the configuration of the system (*Phillips and Van Dyke*, 2017). In a landscape, a state can be thought of as a snapshot of the morphology of the system. Much work in geomorphology assumes that the landscape tends towards a state of dynamic equilibrium (*Hack*, 1975; *Willett and Brandon*, 2002). That is, the morphology of the landscape approaches one quasi-steady state with variability occurring around this mean state. Over longer timescales landscapes are often thought to evolve from one state of dynamic equilibrium to another (*Bishop*, 2007). Though it is sometimes the case that this evolution happens as a gradual shift, abrupt shifts from one state to another are also possible (*Brunsden and Thornes*, 1979). These shifts often occur when a threshold is reached that induces a qualitative shift in the landscape. For example, Schumm developed the geomorphic threshold concept as applied to 'metamorphosing' river channels (*Schumm*, 1979; *Nadler and Schumm*, 1981). Where he posited that changes in slopes, discharge, and sediment supply above given threshold values introduce transitions of channels from braided to sinuous and meandering. Stability diagrams were developed for different channel states based off of the physical parameters governing the channel (such as grain size, Froude number, discharge) (*Schumm*, 1985).

Changes of morphological state can be governed purely by physical factors. However, strong feedbacks can exist between biota and sediment transport that modulate landscape pattern. In wetlands, there is a strong bidirectionality between vegetation and flow conditions that introduce feedbacks which can lead to dramatic shifts in morphology (*Larsen and Harvey*, 2010). The influence of vegetation is also an area of active study in aeolian environments. The presence of vegetation on dune surfaces tends to slow down or stop dune migration through the introduction of increased form drag around the plant bodies that reduces the

effective stress on the sand (*Durán and Herrmann*, 2006b). Disturbance of vegetative communities on dunes has the potential to 'reactivate' previously immobile dunes (*Barchyn and Hugenholtz*, 2013). In coastal dunes, vegetation sets the maximum size that dunes can achieve (*Durán and Moore*, 2013). Workers have also documented that the competition between the deposition rates of a migrating dune and plant growth rates leads to a state change in dune morphology due the progressive inversion of crescent shaped barchan dunes to parabolic dunes (*Durán and Herrmann*, 2006b; *Reitz et al.*, 2010).

In addition to large, qualitative shifts in morphology, much of the small scale dynamics of landscapes are also characterized by changes of state around a threshold. At the grain scale, dynamic states can be defined and transitions between states determined using observations of grain kinematics. Perhaps one of the most well known examples of a change of state at a threshold is the entrainment of coarse grains from an approximately static population to a moving bed load population. Here bed load is defined as the rolling, skipping, and hopping motions of grains near a sediment bed. In streams, the effects of this grain scale threshold percolate up to the channel scale through the organization of coarse grained channel geometry to values near the threshold of motion (*Phillips and Jerolmack*, 2016; *Parker et al.*, 2007). Because naturally occurring gravel channels predominantly exist near this threshold state, the threshold of motion is an important factor controlling the geomorphic response of landscapes to transport events (*Phillips and Jerolmack*, 2016).

Though it is a crucial geomorphic parameter, the threshold of motion for bedload is notoriously difficult to predict. Empirically derived formulations for the bed load flux can have prediction errors up to order of magnitude near the threshold of motion (*Recking*, 2010). Much of this difficulty in prediction arises from large, intermittent fluctuations in transport in both time and space (*Ancey et al.*, 2008a; *Singh et al.*, 2009; *Ancey and Heyman*, 2014; *Heyman et al.*, 2013). These fluctuations arise from both variability in the turbulent driving stress as well as granular factors. It is well documented that turbulent bursts above the mean fluid stress can be responsible for entrainment (*Diplas et al.*, 2008; *Schmeeckle*

and Nelson, 2003; *Papanicolaou et al.*, 2001). Recently, the role of the disordered granular bed in contributing to these fluctuations has become increasingly acknowledged (*Frey and Church*, 2011a). It has been found that the transition of grains into bedload bears many of the hallmarks of what granular physicists call a jamming transition (*Houssais et al.*, 2015; *Maurin et al.*, 2016; *Houssais et al.*, 2016). This transition has been found to govern the dynamics of the shift from static to flowing in many granular systems and is characterized in part by a dramatic growth in the variance of grain motion upon the approach to jamming (*Liu and Nagel*, 2010). Given that the complex, heterogeneous dynamics observed at the jamming transition are similar to bedload transport, an improved understanding of the relationship between the threshold of motion and this transition holds the promise of placing the phenomena of bed load transport within a more general framework.

Whether ultimately arising from turbulence, granular effects, or a mixture of both; the stochastic variations of bed load flux at the particle scale give rise to several unique behaviors. Both the waiting times between transport events and grain hop distances display statistics that deviate significantly from the behavior one would expect if entrainment/disentrainment events were independent of one another and time independent. This statistical behavior appears to have its basis in phenomena such as anomalous diffusion that are controlled by the underlying dynamics (*Martin et al.*, 2012; *Tucker and Bradley*, 2010; *Phillips et al.*, 2013). An understanding of the basis for this behavior is relevant because ultimately grain scale mechanics percolate upwards in scale and find expression in the landscape (*Stark et al.*, 2009; *Mariotti et al.*, 2013; *Voller and Paola*, 2010).

The dynamics that govern transport near the threshold of motion make accurate predictions of transport difficult. This difficulty is further enhanced in the field by additional factors because conditions can introduce large variability in the threshold of motion that do not have their origin solely in grain dynamics. In the field, variability in the threshold of motion is induced by the collusion of physical and biotic factors. Among them soil moisture (*Jackson and Nordstrom*, 1997), microbial activity (*Belnap and Gillette*, 1998; *Fang et al.*, 2014),

vegetation (*Lancaster and Baas*, 1998), compaction (*Webb*, 1983), and others. Patterns of variability in the threshold of motion affect the erosive response of the land to wind events and influence larger scale patterns of ecology and morphology in the landscape (*Webb and Strong*, 2011; *Okin et al.*, 2006; *Barchyn and Hugenholtz*, 2013). At the global scale, our ability to accurately model dust emissions is hampered by the sensitivity of emissions to estimates of the threshold of motion that are poorly constrained (*Kok et al.*, 2014). Inaccurate predictions of these emissions confound our ability to accurately model the dust cycles contribution to climate change or anticipate the human health implications of different land use patterns (*Cakmur et al.*, 2006; *Watanabe et al.*, 2011; *Goudie*, 2014). We currently have a poor grasp on the real world heterogeneity of the threshold of motion due to the difficulty associated with acquiring the number of measurements that would be necessary to provide adequate constraints.

This dissertation examines the mechanics of sediment transport near changes of state at three distinct scales: landscape scale feedbacks between transport dynamics and vegetation; the relationship between a soils mechanical properties and its threshold of motion; and grain scale dynamics as the threshold of motion is approached. For both field and lab measurements, an emphasis is placed on implementing methods that allow for empirical observations that provide a foundation for inferences about the physical processes involved in the observed state changes.

Chapter 2 considers bed load transport as the rate of transport is decreased from near continuous to close to the threshold of motion. Due to bed load transports stochastic nature, probabilistic approaches that build off of the original work of *Einstein* (1950) are one of the primary ways bedload transport is modeled (*Papanicolaou et al.*, 2002; *Ancey et al.*, 2008a; *Heyman et al.*, 2013). Further incorporation of the underlying physics governing bed load has the potential to improve existing statistical mechanical models as our understanding improves (*Furbish et al.*, 2017). A recent example is the growing awareness of the role grain-bed impacts play in entrainment (*Pähtz and Durán*, 2017; *Vowinckel et al.*, 2017). Despite

their success, direct observation of key parameters introduced by some probabilistic models has proven challenging. One model parameter that is difficult to quantify directly are collective 'bursts' of entrainment of many grains at once. Collective entrainment is thought to be a key cause for the large variances around mean transport typical of bed load (*Gomez and Phillips*, 1999; *Nikora et al.*, 2002; *Singh et al.*, 2009). In an attempt to examine the effects of collective entrainment on transport we perform experiments that allow us to track the trajectories of individual grains. A key feature of the experimental design is that we can precisely control the frequency with which grains are fed into the system. Transport rates are varied from intermittent transport close to threshold to near continuous at high transport rates. We directly observe collective entrainment as well as the behavior of the length scale of collective motion as a function of the range of transport rates studied. These experiments allow us to explore the relative contribution of collective entrainment and the waiting times between transport events to the observed growth in transport intermittency. In addition, the data is used to assess the role of grain-bed collisions on observed entrainment.

Chapter 3 examines variability in the threshold of motion itself. Similar to chapter 2, coarse grained transport is studied, though here the emphasis is placed on sub-aerial transport. Constraining the variation of the threshold of motion in arid environments remains a challenge (*Kok et al.*, 2014). While parametric models that attempt to relate variations to factors such as surface moisture, drag partitioning, and other environmental factors are useful, they require tuning constants for each field site (*Zender et al.*, 2003). Historically, in-situ attempts to measure variations in the threshold of motion have used portable wind tunnels or been reliant on natural wind speeds to trigger saltation measurable by saltation sensors (*Gillette*, 1978; *Shao et al.*, 1993; *Wiggs et al.*, 2004; *Stout*, 2007). Portable wind tunnels provide on demand estimates of the threshold of motion, but they are large (typical lengths of 5 meters), and the logistics involved in obtaining a large number of measurements can be formidable (*Van Pelt et al.*, 2010). A new device, the Portable In Situ Wind ERosion Laboratory (PI-SWERL), has highlighted the applicability of more rapidly performable tests of erodibility (*Etyemezian et al.*, 2007; *Goossens and Buck*, 2009). In this spirit, we

develop a new mechanical test of a soils surface shear strength that has the potential to be deployed by the semi-autonomous robotic platform recently described by *Qian et al.* (2017). We then examine the ability of the newly developed test to provide an estimate of the threshold of motion by comparing the measured shear strength with estimates of the threshold of motion provided by the PI-SWERL. The possibility of using this test along with other robotically deployable, in situ tests of a soils mechanical response to provide a fuller characterization of erosive response is discussed.

Chapter 4 zooms out to examine the interaction between sediment transport and vegetation at the scale of a dune field. Dunes are dynamic features of the landscape that are inherently out of equilibrium. Interestingly, though individual dunes are unstable, interactions between dunes are thought to maintain some dune fields in a state of dynamic equilibrium (*Elbelrhiti et al.*, 2008, 2005). A fundamental mechanism controlling this equilibrium is a fluid instability on the order of tens of meters that arises on the gently sloping, stoss surfaces of dunes (*Elbelrhiti et al.*, 2005; *Ping et al.*, 2014). This instability leads to the formation and emission of new dunes from existing dunes and counteracts the tendency of dunes to grow bigger as a result of collisions (*Hersen and Douady*, 2005). Near the boundaries of pattern stable regions of dune fields, the role of plants in contributing to morphological shifts in dunes is well established (*Durán and Herrmann*, 2006b; *Reitz et al.*, 2010; *Barchyn and Hugenholtz*, 2012; *Yan and Baas*, 2015). Plants are thought to slow down the rate of dune migration by: reducing boundary shear stress due to form drag (*Durán and Herrmann*, 2006b; *Lancaster and Baas*, 1998); binding and consolidation of sand by roots (*Waldron*, 1977); and facilitating the formation of sand-stabilizing soil crusts. Though the role of plants in modifying rates of migration is undeniable, it is likely that they have other effects on transport that help disrupt dune field pattern. Chapter 4 explores how plants interact with the fluid instability that helps regulate the dynamic equilibrium of dune fields. We do this using remote sensing data acquired at White Sands National Monument in Mexico to directly relate information about dune kinematics and morphology to estimates of how the fraction plant cover varies throughout the dune field.

A unifying theme of this dissertation is that, regardless of scale, shifts in landscapes often occur as abrupt changes of state around a threshold as one state of dynamic equilibrium gives way to another. This work focuses on the role that sediment transport, a fundamental driver of earth surface evolution, plays in these changes of state. Both the dynamics of transport itself as well as the interaction of those dynamics with other shapers of the landscape. Through seeking to contribute to our understanding of this interaction, this dissertation continues the work of relating grain scale physics to larger scale morphology.

CHAPTER 2 : Scales of collective entrainment and intermittent transport in collision-driven bed load

Abstract:

Fluvial bed-load transport is notoriously unpredictable, especially near the threshold of motion where stochastic fluctuations in sediment flux are large. A general statistical mechanics framework has been developed to formally average these fluctuations, and its application requires an intimate understanding of the probabilistic motion of individual particles. Laboratory and field observations suggest that particles are entrained collectively, but this behavior is not well resolved. Collective entrainment introduces new length and time scales of correlation into probabilistic formulations of bed-load flux. We perform a series of experiments to directly quantify spatially-clustered movement of particles (i.e., collective motion), using a steep-slope 2D flume in which centimeter-scale marbles are fed at varying rates into a shallow and turbulent water flow. We observe that entrainment results exclusively from particle collisions and is generally collective. In contrast, particles deposit independently of each other. The size distribution of collective motion events is roughly exponential and constant across sediment feed rates. The primary effect of changing feed rate is simply to change the entrainment frequency, although the relation between these two diverges from the expected linear form in the slowly-driven limit. The total displacement of all particles entrained in a collision event is proportional to the kinetic energy deposited into the bed by the impactor. The first-order picture that emerges is similar to generic avalanching dynamics in sandpiles: "avalanches" (collective entrainment events) of a characteristic size relax with a characteristic timescale regardless of feed rate, but the frequency of avalanches increases in proportion to the feed rate. The transition from intermittent to continuous

bed-load transport then results from the progressive merger of entrainment avalanches with increasing transport rate. As most bed-load transport occurs in the intermittent regime, the length scale of collective entrainment should be considered a fundamental addition to any probabilistic bed-load framework.

2.1. Introduction

Bed load, the motion of particles along a stream bed by rolling, hopping and sliding, is the dominant mode of transport in rivers for particles larger than 10mm (*Parker et al.* (2007); *Dade and Friend* (1998); *Jerolmack and Brzinski* (2010)). Bed-load flux equations lose their predictive power as fluid stress decreases toward the threshold of motion (*Recking* (2010)), where sediment transport becomes increasingly intermittent and exhibits fluctuations across a wide range of length and time scales (*Ancey et al.* (2008a); *Singh et al.* (2009); *Ancey and Heyman* (2014); *Heyman et al.* (2013)). Gravel-bed rivers organize their bank-full geometry such that they are always near threshold (*Parker et al.* (2007); *Phillips and Jerolmack* (2016)). There are two potential causes of intermittency in near-threshold bed load: (i) variability in the driving stress due to turbulent eddies near the bed (*Nelson et al.* (1995); *Papanicolaou et al.* (2001); *Sumer et al.* (2003); *Diplas et al.* (2008); *Schmeeckle and Nelson* (2003)); and (ii) variability in the resistive force of the bed due to structural arrangements of the grains (*Charru et al.* (2004); *Martin et al.* (2014); *Prancevic and Lamb* (2015); *Yager et al.* (2007)). The role of turbulence has received the most attention, though granular contributions to bed-load dynamics are increasingly being recognized (*Frey and Church* (2011a); *Houssais et al.* (2015); *Maurin et al.* (2016)). One of the defining features of granular systems is a continuous transition from flowing to static regimes known as the jamming transition. On approach to jamming, particle motion becomes progressively slower and more heterogeneous; the variance in fluctuations of particle displacements grows rapidly (*Keys et al.* (2007); *Liu and Nagel* (2010)). Experiments show that the onset of bed-load transport has the hallmarks of a jamming transition (*Houssais et al.* (2015); *Maurin et al.* (2016); *Houssais et al.* (2016)). Near-threshold transport rates exhibit strong correlations and intermittency, while fluxes at rates far above threshold are uncorrelated and smooth (*Singh et al.* (2009)). As most gravel-bed rivers exhibit bank-full fluid stresses only marginally above threshold (*Parker et al.* (2007); *Phillips and Jerolmack* (2016)), this implies that these channels exist near the jammed state (*Frey and Church* (2011b); *Houssais et al.* (2016)). The stress distribution along a river bed is expected to exhibit a complicated

structure, making the granular response to an applied fluid stress highly unpredictable (*Albert et al.* (2000)). Moreover, particle motion is expected to be highly localized and to exhibit nontrivial fluctuations.

Given these challenges, and the many-body nature of the problem, one sensible approach is to examine bed-load transport in a probabilistic framework after *Einstein* (1950). Einstein defined a bed-load flux function of the form $q_x = E\bar{L}_x$. In this formulation of bed-load flux q_x, the entrainment rate function E assumes a fixed timescale for the exchange of an inactive particle with an active one. More importantly, it assumes that both entrainment and deposition of particles are a time independent, Poisson process and that particles do not interact. With these assumptions, the probability of entrainment is dependent only on flow conditions and the intensity of bed-load transport in an area of the bed. $\bar{L}_x$ is the mean hop length. The discussion above, however, indicates that bed-load transport has characteristics that deviate from the time-independent, non-correlated process assumed by Einstein. Indeed, experimental and field observations have revealed extreme fluctuations in particle activity/flux above the mean (i.e. extreme variance) (*Gomez and Phillips* (1999); *Nikora et al.* (2002); *Singh et al.* (2009); *Ancey et al.* (2008a)), collective grain motion (*Drake et al.* (1988); *Dinehart* (1999); *Ancey et al.* (2008b)), and anomalous diffusion of particles (*Ganti et al.* (2010); *Tucker and Bradley* (2010); *Phillips et al.* (2013)). Starting with *Ancey et al.* (2008b), a series of models for bed-load transport have been proposed that posit that particles are often entrained collectively rather than individually at low mean transport rates. These models propose modifications of Einstein's entrainment function that take this correlated behavior into account through the introduction of a collective entrainment rate, μ, that leads to a characteristic correlation length , l_c (*Ancey et al.* (2008b); *Heyman et al.* (2013); *Ma et al.* (2014); *Heyman et al.* (2014)). As the mean transport rate is lowered, the relative contribution of μ derived from the models must increase in order to reproduce the observed growth in variance of bed-load activity (i.e., the number density of moving grains). Collective entrainment is thus hypothesized to be the primary driver of observed intermittent and correlated bursts in bed-load transport near threshold; however,

11

it has not been directly observed and quantified. *Furbish et al.* (2017) has taken a more generalized approach to modeling stochastic bed-load transport, by viewing all probabilistic formulations of bed-load flux that incorporate diffusivity as an approximation of a Master equation that exactly conserves both probability and mass. One key to making this approximation effective is a deep understanding of the underlying assumptions used to construct the effective diffusivity of the particles. *Einstein* (1950) and others have assumed that bed load transport could be modeled as a Brownian process, though there are important differences between bed load and Brownian motion. These can lead to major departures in how the diffusion approximation is to be applied and interpreted in the context of bed-load transport. For example, recently *Fathel et al.* (2016) showed that the apparent anomalous behavior in the diffusivity of bed load particles at short times is actually a byproduct of the nonlinear growth in the variance of particle hop lengths as particle travel times are shortened. Furbish and colleagues' statistical mechanics framework is the most general model for bed-load transport; given knowledge of the microscopic and probabilistic motions of particles, one may derive continuum-like expressions for the macroscopic behavior. Collective particle motion could be incorporated into this framework, but this requires an intimate understanding of the associated scales and correlations.

The probabilistic approach has proven valuable for describing the nature of transport near threshold. Ultimately it is vital to link this approach to a description of the physical origins of the stochastic behavior. If collective entrainment is the primary cause of bed load flux intermittency then what leads to it? One possible mechanism for collective motion is collisional impulses. Collisions are widely recognized as drivers of bed load transport in aeolian systems where separate thresholds for entrainment without collision, the fluid threshold, and with collisions, the impact threshold, have been defined (*Bagnold* (1941); *Martin and Kok* (2016)). In aeolian systems these collisions are accompanied by dramatic 'splash' events where numerous particles are ejected at once (i.e. collectively). Recently, it has been proposed that entrainment in sub-aqueous systems has a significant collisional component as well especially in the case of large Stokes numbers (*Pähtz and Durán* (2017)).

The Stokes number is the ratio of a particle's inertial forces to the viscous forces of the fluid and, for binary collision between same-sized spheres, is given by (*Schmeeckle et al.* (2001)): $St = (\frac{1}{9})\frac{RDu_s}{\nu}$. Here, R is the submerged specific density, u_s is particle velocity, ν is fluid viscosity, and D is particle diameter. For $St > 10^2$, viscous damping of collisions is negligible (*Schmeeckle et al.* (2001)) and thus collisions from saltation are expected to impart significant momentum to both the bed and neighboring particles for $D \geq 10^{-2}m$. Thus, it is likely that in coarse gravel streams, colliding particles cause a subdued 'splash' similar to aeolian systems. If the analogy with aeolian systems holds then this splash entrainment will involve many particles becoming entrained at once. This hypothetical, collision-induced collective entrainment could be strong enough to be a primary driver of burstiness in bed-load flux near threshold.

There are other physical systems examined previously that organize themselves near a threshold, and display intermittent mass flux; the behavior of avalanching sand and rice piles comes to mind (*Rajchenbach* (1990); *Lemieux and Durian* (2000)). These systems have been extensively studied and display intermittent transport in the limit where they are slowly driven past a threshold (in this case a critical angle). In the intermittent regime, the size and duration of avalanches is indeterminate (*Frette et al.* (1996)). As the sand pile is driven harder this intermittent regime gives way to continuous flow down the heap with an approximately constant flux. *Hwa and Kardar* (1992) showed how this transition into continuous flow can be viewed as a merger of the intermittent, avalanching events. Might bed load fit into a class of more generic avalanching systems that transition from intermittent to continuous transport as they are taken from slowly driven to continuously driven?

In this paper we use the slowly to continuously driven limits as end members to explore how the nature of particle activity in an idealized bed-load experiment changes as the frequency of mean transport is varied. Control of the mean transport rate is achieved by using a system that allows for precise control of the sediment feed rate while slope and

fluid discharge are held constant. During the experiment particle motion is tracked using sequential images. The imposed feed rate is analogous to a driving frequency. We replicate the previously observed growth in the intermittency of transport as the imposed sediment feed rate/driving frequency is slowed. Our major contribution is the direct observation of collective entrainment, which reveals that collisions release spatially-grouped clusters from the bed that are analogous to avalanches. We relate the scales of collective entrainment to the kinetic energy deposited into the bed by colliding saltators. This assumption lends credence to the hypothesis that saltator-bed collisions play a large role in entrainment (both collective or otherwise). In our experiments, the growth in intermittency in bed-load transport appears to arise primarily from the non-linear growth in the waiting times between transport events as the driving rate is slowed.

2.2. Methods

2.2.1. Experimental setup

The experiments are conducted using a narrow, quasi 2-dimensional (2D) flume in which all the grains in the subsurface and surface can be monitored. The flume channel is 2.3 meters long and 20 mm wide. For all experiments, two different sized spherical glass beads, 12mm and 16mm in diameter, are fed into the channel in an even mixture. The two different sizes are chosen to ensure a randomly packed bed. The "quasi 2D" nature of the experiment arises from the fact that the small glass beads have significant overlap with one another along the axis orthogonal to the viewing window. All experiments are conducted in a flume slope of 6%, and a fixed discharge of 37.9 liters per minute, while the feed rate at which the particle mixture is introduced to the channel is varied. The feed rate is the control parameter used in the experiments, and throughout the rest of the paper will be referred to as the driving frequency. The driving frequencies used for the experiment were: 40, 60, 80, 160, and 200 marbles per minute. Throughout the paper the abbreviation MPM will be used for marbles per minute.

14

At the flow rate used, all flows in the channel are turbulent with Reynolds numbers greater than 10^4. Flow depths were found to be uniform with the exception of 10-15 cm near the inlet and outlet of the flume. The flow is supercritical with Froude numbers greater than one, though any bedforms that would be present at these flow conditions are suppressed due to the narrowness of the channel. Experiments are in the high Stokes number regime where collisions are expected to be important, in order to mimic the conditions of gravel-bed rivers. Although collision velocities vary (they are quantified below), they scale roughly with settling velocity; using terminal fall velocity as a scale parameter, $St > 10^2$ for all experiments. Details about the flow parameters observed during the experiments are given in table 2.1. Only mean flow parameters are listed as the flow parameters are kept approximately constant across experiments. The assumption of approximately constant flow conditions was verified during the experimental runs where the range of flow conditions that occurred during a single experiment was similar to the variability in conditions seen across experiments. This flume is thought to represent the simplest possible physical model of bed-load transport. A diagram of the experimental setup can be seen in figure 2.1. The experiment is very similar to that used by Ancey (*Ancey et al.* (2008b)). This similarity is intentional so that their results can guide the current study and the findings can be compared to their data.

A camera is situated approximately 100 cm downstream of the flume inlet. The viewing window of the camera is 35 cm for all experiments. This section of the flume is back-lit using a white LED panel array that outputs at 300 lumen. This arrangement produces a sharp silhouette of all the grains in the viewing window that can then be used to acquire approximate particle centers. Images are acquired at a rate of 120 fps and streamed continuously to a computer. This acquisition rate is necessary to adequately capture the trajectories of individual particles as they move through the viewing window.

2.2.2. Data acquisition and analysis

Once images are acquired, approximate particle centers are located using a hybrid form of the algorithms outlined in *Khan and Maruf* (2013) and *Parthasarathy* (2012). Using this method it is possible to obtain particle centers that are accurate to better than 1 mm. However, the method is highly sensitive to the degree of occlusion that the particles in the bed experience, and therefore centers can sometimes be less accurate. Once particle centers are obtained, particles are linked together from image to image to obtain particle trajectories using the method outlined by Crocker and Grier (*Crocker et al.* (1996)). An example trajectory that is the final output of this process can be seen in figure 2.2.

With a particle trajectory affixed to each particle that enters and leaves the viewing window, it becomes possible to analyze the dynamics of mobile particles over a wide variety of timescales. Emigration events sampled in the viewing window are also simple to obtain from these trajectories. Emigration series are obtained by choosing a fixed along-stream distance, x, to sample along the viewing window for all experiments in question. If a particle center crosses this position in the downstream direction it is counted as a positive emigration event. If it crosses this position in the upstream direction it is counted as a negative emigration event. This definition is identical to that used in *Ma et al.* (2014). To study the active particles within the viewing window it was necessary to set a threshold for particle mobility. To do this particle trajectories were analyzed over 1/10 of a second. If the particle displaced 2.4 mm within this time window then the particle was deemed mobile.

One approach to estimating the intermittency of the series of emigration events obtained during an experiment (see figure 2.4) is to look at how long one needs to sample to arrive at a threshold standard deviation. In the case of a uniform, low intermittency time series this sampling timescale will be very short, whereas in the case of a highly intermittent series a long sampling time will be needed. This timescale is referred to throughout the rest of the paper as t_{conv}. It is computed directly from the obtained emigration series for all of the driving frequencies studied, by incrementally increasing the time, τ, used to

sample from the emigration series. For a given τ, 500 samples from the emigration series are randomly re-sampled from the emigration series in question using a "bootstrap" technique. The standard deviation of these samples is then computed and normalized by the mean emigration rate for the samples taken from the series. As τ grows, the standard deviation approaches the value chosen as the threshold standard deviation, t_{conv}. When the threshold standard deviation is reached this value is interpreted as t_{conv}. This approach is identical to that used in *Houssais et al.* (2015).

Waiting times are sampled from the emigration series as well. They are interpreted to be the time periods in between active emigration events over position x. A waiting time period is started after an emigration event over position x occurs, and ends when the next emigration event happens.

Activity within the whole viewing window sampled in the experiments is characterized in the paper through two different event-based metrics. One type of event is referred to specifically as a "collective entrainment event". This event is defined as a group of one or more mobile particles (mobility was determined using the criteria above) moving within one large-grain diameter of each other. This analysis is a simplified version of that used to identify mobile clusters in *Keys et al.* (2007). An example of a collective entrainment event is given in figure 2.3. In this example, the 4 large grains that are in color would be considered a collective entrainment event. Collective entrainment events were identified directly from analysis of the mobile particle trajectories sampled in the viewing window for a given experiment. For a given time step all N mobile grain trajectories were identified. For $i = 1$ to $i = N$, the distance of the ith mobile grain to all the rest of the mobile grains was computed. A clustering algorithm was then employed to identify clusters of grains that were within a threshold distance of one another. This algorithm is capable of identifying an arbitrary number of mobile clusters occuring at the same time within the viewing window. A single mobile cluster of grains is defined as a collective entrainment event. This cluster analysis was performed for the entirety of the time steps available for a given experiment.

17

This method allowed us to gather statistics of all of the collective entrainment events that occurred in the viewing window for a given experiment.

The other type of event is a "transport event"; it is more general, and contains collective entrainment events within it as a subset. It is defined as a time period where there is at least one mobile grain within the viewing window. As long as this situation is the case, an event is said to be taking place. Once there are no mobile grains within the viewing window then the transport event has stopped. A portion of a transport event is pictured in figure 2.3. Here all the grains that are colored are considered to be part of the current transport event that is taking place. It is possible to see there are time instances in figure 2.3 where collective motion is not occurring but particle activity is still ongoing. These time instances with no collectively moving particles would be counted as part of a transport event, but not as part of a collective motion event.

To analyze the effects of impacts during events, saltating grains were separated from the rest of the mobile population for a given event. The trajectories of the saltators were then numerically differentiated twice to obtain acceleration series of the trajectories. A change-point detection algorithm was then employed to identify the spikes in the acceleration series representative of impact events.

2.3. Results

All of our experiments exhibited intermittent particle activity (figure 2.4). This intermittency confounds efforts to determine the time needed to arrive at an average activity or flux for a given rate of transport, Δt_{conv}. We computed Δt_{conv} for all driving rates used in the present study, and found that it declines monotonically with increasing feed rate (figure 2.5A). A naive expectation for the decrease in the averaging time is that it should be proportional to the inverse of the driving frequency; that is, $\Delta t_{conv} = a/Q_i$, where a is a scaling parameter that depends on the percent standard deviation threshold chosen to determine t_{conv}. This relation can be thought of as marking the growth in time required

to count a fixed number of particles emigrating past a line if driving frequency were the only factor that mattered. Strong driving frequency dependence should be the case at high transport rates where we expect smoother transport; accordingly, we choose $a = 110$ such that the relation matches the observed data for the highest feed-rate experiment. We see that the naive relation describes the convergence time reasonably well for the three highest feed-rate experiments (figure 2.5). For the two slowest feed rates in the study, however, the actual increase in averaging time with a reduction in Q_i is more rapid than this expectation.

The waiting times between all observed emigration events for a given experiment were sampled, and used to compute empirical complementary cumulative distributions (figure 2.6A). We compare these distributions to a Poisson distribution with a value $\lambda = 1$, which is on the order of the mean waiting times seen in the experiments. The Poisson distribution was chosen for comparison because of the extensive body of literature showing its fitness for modeling uncorrelated random processes (*Lawler and Limic* (2010)). If the waiting times are uncorrelated and truly random they should follow a Poisson distribution; however, the measured waiting times decay much more slowly (figure 2.6A). As expected, the waiting times between emigration events seem to be a function of the driving frequency. When the former are non-dimensionalized by the latter, the variance among the experiments is significantly reduced (figure 2.6B). Moderate dispersion remains among the different experiments, however, indicating that driving rate is not the only factor controlling the waiting times. We compute the average waiting time for each experiment; the naive expectation is that this waiting time is precisely the inverse of the driving frequency. The data follow this expectation for the three highest driving frequencies; however, the mean waiting times for the two slowest-driven experiments are significantly larger than expected (figure 2.7).

The above results demonstrate that driving frequency has a strong effect on the timing of emigration events, and the timescale required for averaging. To determine if this frequency also effects how particles are transported, it is necessary to examine the particle kinematics during times when particle activity is present. We examine here the complementary cumu-

19

lative distributions of particle speed for all experiments (figure 2.8). The tails of the speed distributions do not vary strongly as a function of driving frequency. This observation is sensible as the slow speeds (< 0.1 mm/s) are associated with essentially immobile particles, whereas the fast speeds (> 100 mm/s) are almost exclusively associated with saltators. As the fluid discharge is kept constant across experiments, we do not expect to see large differences in the speed of saltating grains. We do detect an effect of driving frequency, however, for the intermediate speeds (figure 2.8). As the driving frequency declines, the transition between mobile (fast) and immobile (slow) particles appears to grow more abrupt; this transition is manifest as a growing kink in curves. In other words, the distribution of particle speeds is more continuous at high driving frequencies, and becomes more bimodal at low driving frequencies as motion separates more distinctly into slow and fast particles.

Thus far we have examined the motion of individual particles. Here we consider collective entrainment events — in particular, the size distribution of particles that have been determined to be moving together. These mobile clusters are analogous to avalanches in other granular systems. Interestingly, the distribution of mobile clusters does not vary significantly with driving frequency (figure 2.9). All experiments show a roughly exponential distribution of cluster sizes, with a mean size that varies only slightly with driving frequency.

We observe qualitatively that almost all entrainment is associated with impacts. However, the exact nature of this relationship is extremely difficult to untangle for individual entrainment events. Entrainment can happen immediately after an event, or after an unpredictable time delay. In addition, because the disordered bed absorbs and transmits momentum in a complex way, a particle can be entrained as a result of an impact that happened a significant distance ($>> D$) upstream. To avoid these issues, while still gaining insight on the effects of impacts on entrainment, an attempt to look at all impacts for a given period of particle activity in the observational window of an experiment was performed. An event was defined as a period where at least one particle was always mobile. Once all particles in the observation window become immobilized, the event is deemed over (see above). For a

given event we computed: (i) the amount of kinetic energy (KE) deposited into the observed section of the bed; (ii) the cumulative displacement of all mobilized particles; and (iii) the number of particles mobilized. Deposited KE was determined by identifying the points in time when an entrained saltator collided with the bed. The saltator velocity immediately before the collision and the velocity immediately after the collision was used to obtain the difference in KE of the saltating particle that occurs as a result of the collision. This difference in KE was interpreted as occurring because of the inelastic collision of the saltator with the bed, and can be interpreted as being the kinetic energy transferred (or deposited) by the saltator into the bed. The KE deposited, cumulative displacement, and the number of particles mobilized was compiled for all events and for all driving rates, in order to determine the extent to which particle mobility may be understood from collision energetics. The data reveal a remarkably clear, linear relation between the total KE deposited and the cumulative displacement of mobile particles (figure 2.10A). Also the number of mobilized particles systematically increases with KE deposited, though there is significant variability (figure 2.10B).

2.4. Discussion and conclusion

For all driving frequencies, both the magnitude of collective entrainment events (figure 2.9) and the speed of saltating (fast) particles (figure 2.8) are similar. This determination indicates that collision dynamics do not vary significantly across the range of sediment feed rates probed here. Roughly, the intermittency of transport is controlled by the growth in the mean waiting time as the driving frequency is slowed (see figure 2.7). Changing the driving rate appears to primarily affect how quickly events happen, and not the fundamental nature of entrainment. In the slowly driven limit, (collective) entrainment events are infrequent and may be considered as discrete bursts in transport. As the system is driven at higher feed frequencies, events occur more frequently and begin to overlap with one another. At the fastest driving rates, events become indistinguishable from one another and continuous transport emerges. This picture aligns with behavior seen in avalanching systems that

display an intermittent to continuous transition (*Hwa and Kardar* (1992); *Rajchenbach* (1990)). A sand pile model by *Hwa and Kardar* (1992) showed that overlapping avalanches may interact, introducing correlations in the flux output of the system. The observed changing distribution of particle speeds with driving rate in our experiments may be an indication of this kind of complex behavior.

Much of the difference in entrainment rate and intermittency can be related simply to the driving rate, though some of it cannot. In particular, at low driving rates we see waiting and averaging times that are significantly longer than expected, suggesting that the first-order kinematic avalanching model described above is incomplete. One timescale that has not been considered is the relaxation time of avalanches, which for our experiments would be the deposition timescale of mobile clusters following an entrainment event. This timescale may not be independent of driving rate, and it becomes impossible to measure when avalanches overlap in time. Another complicating factor at low driving rates is the influence of creep, which has been demonstrated to drive bursty bed-load transport in the viscous flow regime (*Houssais et al.* (2015)). Movies of our experiments reveal the presence of slow creep also, but quantifying the significance of this phenomena is beyond the scope of the present paper.

Indeterminate, complex behavior (such as the possible scenario outlined above) is often an inherent feature of many-bodied, driven and strongly dissipative systems (*Regev et al.* (2013)). For the system of a turbulent fluid driving marbles that collide with a bed, it is not possible to predict the response of a collision. Some collisions result in a strong rebound of the saltator and no (observable) response of the bed; others drive an immediate splash as several grains are entrained; and yet others lead to a delayed response, in which a large number of grains become destabilized and slowly accelerate to become entrained. Knowledge of the kinetic energy of an impact is not sufficient to understand entrainment, due to the complicated nature of energy dissipation. Knowledge of energy dissipation, however, allows for significant predictive power. The strong relations between energy deposited, and the size and cumulative displacement of entrained particles, provide some mechanistic basis for

understanding collective entrainment and burstiness in collision-driven bed load.

The similarity of collective entrainment events between driving rates shows that, while collective entrainment is present, its associated length scale does not vary as a function of intermittency. It is likely that collision-induced momentum transfer into the bed is what sets the scale of collective entrainment, though more analysis remains to be done. Fluid discharge did not vary in our experiments, therefore the velocity of saltating grains (and hence impact energy) remained roughly constant for all driving rates. The approximately constant exponential trend (figure 2.9) aligns with the expectation that momentum transfer due to saltator-bed impacts should be a primary driver of entrainment in this system. *Ancey et al.* (2008b) were correct in positing a length scale for collective entrainment; we see definite evidence for a length scale of particle motion that is larger than that of a single particle. While this length scale does not vary in these experiments, it is challenging to extrapolate to other systems. At smaller Stokes numbers, collisions are damped and turbulence becomes an important driver of collective entrainment (*Nelson et al.* (1995); *Papanicolaou et al.* (2001); *Sumer et al.* (2003); *Diplas et al.* (2008); *Schmeeckle and Nelson* (2003)). The shapes and size distributions of natural particles, and roughness of the river bed (e.g., bed forms), will also likely influence collective entrainment in ways that are difficult to anticipate. Nevertheless, collision-driven entrainment should be the norm for gravel-bed rivers (*Jerolmack and Brzinski* (2010)), and collective entrainment has already been observed in the field (*Drake et al.* (1988)). Incorporating this length scale into the general probabilistic framework proposed by Furbish (e.g. *Furbish et al.* (2012, 2017)) will be important in the effort to build statistical-mechanical models of bed-load transport, that start with correct assumptions of the underlying dynamics that govern bed-load particle trajectories. Understanding the scales of bursty bed-load transport will also inform the requisite times for bed-load sampling in the field and laboratory (*Singh et al.* (2009)).
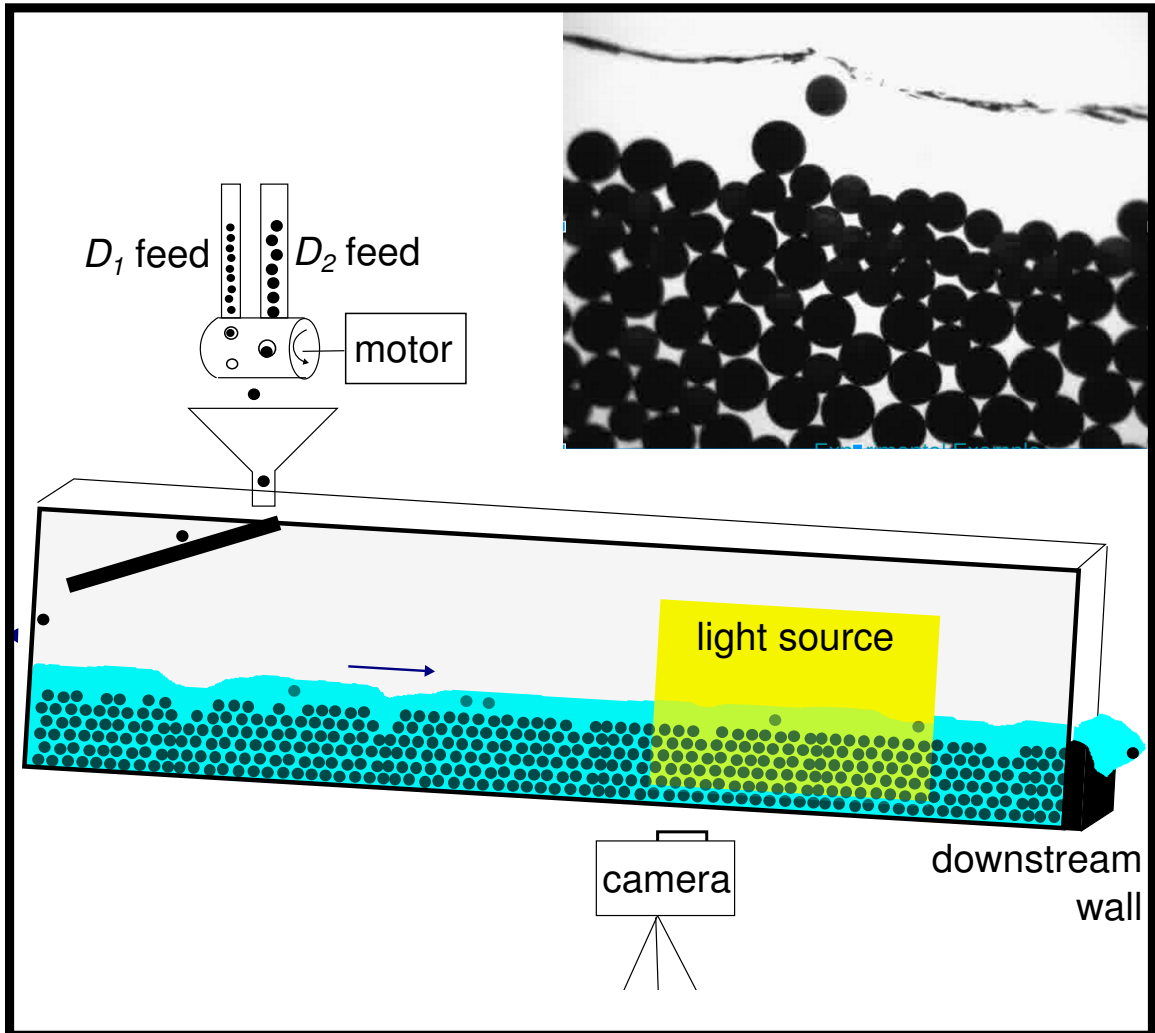
Figure 2.1: Schematic of the experimental setup. The system is 2.3 meters long and 20 mm wide. This quasi-two dimensional channel is fed at a constant water discharge for all experiments. The slope is kept constant at 6 %. The sediment feed is uncoupled from the fluid discharge, and is introduced from above using a custom designed feeder built at the PennSed laboratory. A viewing window on the order of 35 cm is selected two thirds of the way down the flume. The window is back-lit and the resulting images can be seen in the figure inset.
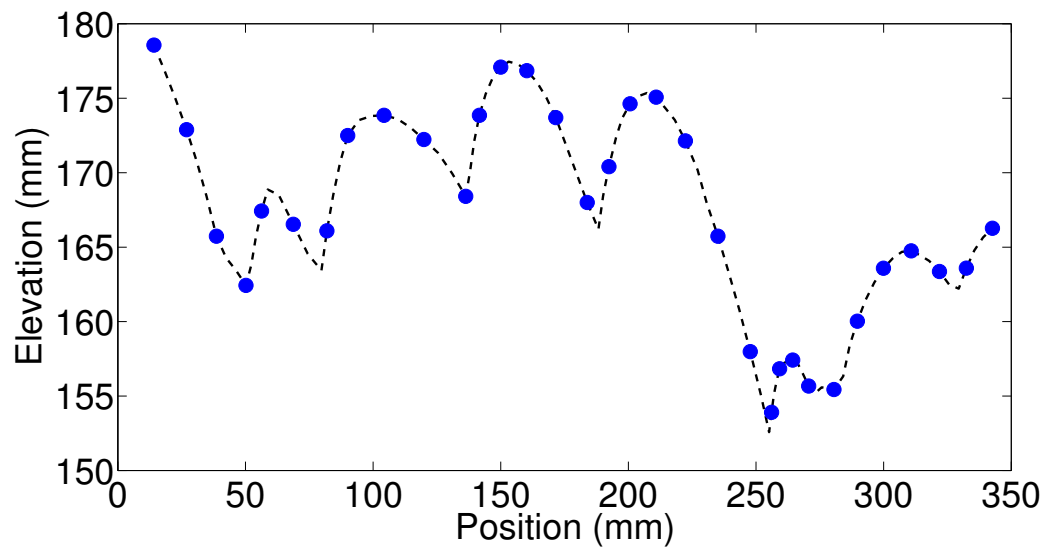
Figure 2.2: An example saltator trajectory obtained during one of the experimental runs. Trajectories are created for all particles present in the sampling area of the experiment.
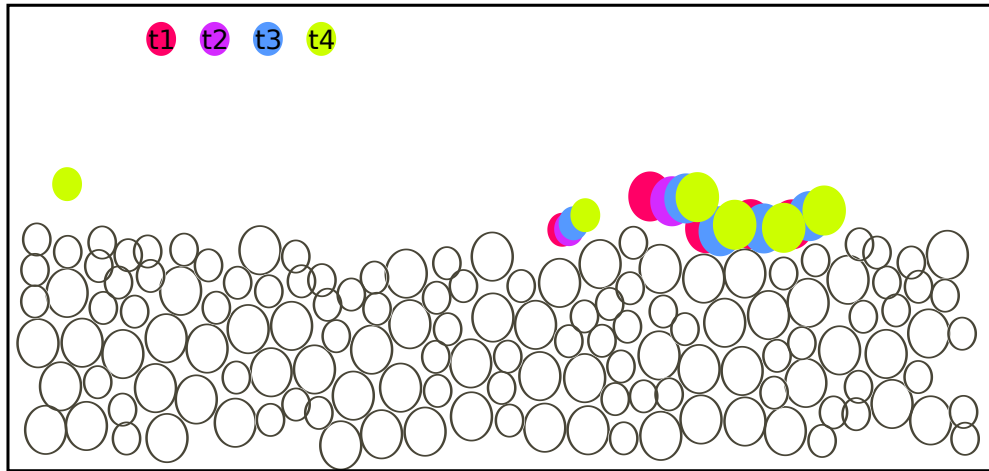
Figure 2.3: An example of a collective motion event sampled at 4 different times during the event. The particles that are displacing actively during the event are color coded according to their position at the time step (t1, t2, and so on) associated with a given color. At t1 only two particles are moving. The large particle collides with three particles on the bed at t2 and these three particles displace at t3 and t4. The four large particles would be classified as moving together collectively.
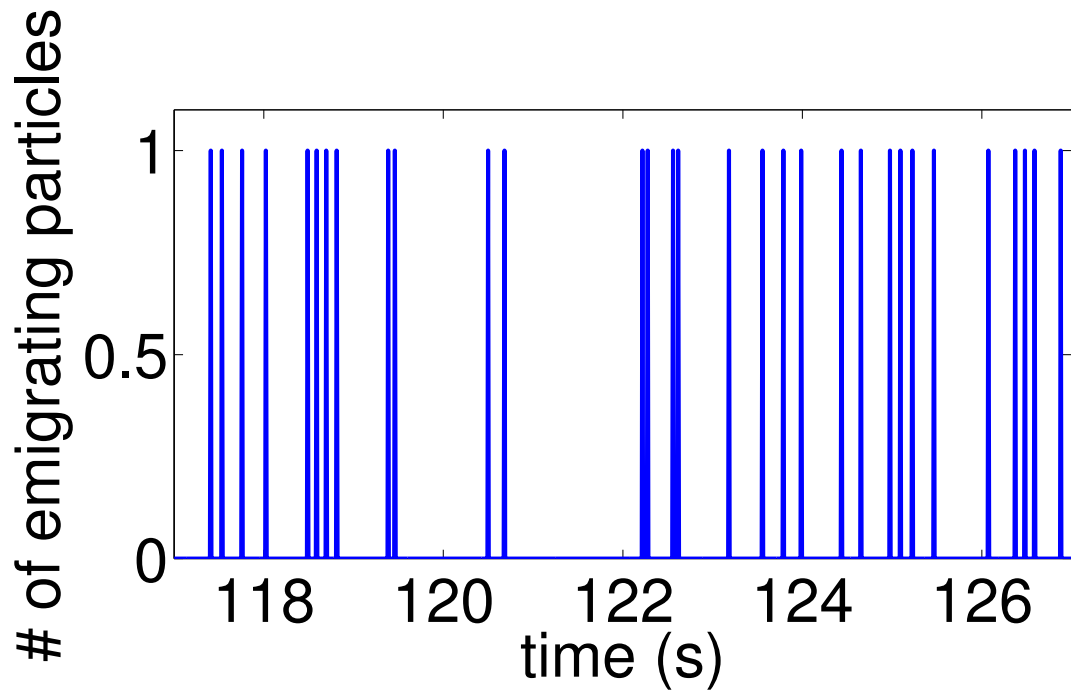
Figure 2.4: Example time series of emigration events for $Q_i = 40$ MPM. A position x along the bed viewing window (as seen in Figure 2.1) is monitored during the experimental runs. When a particle passes position x it is considered an emigration event. This is a simple measure of particle activity that can be converted to a time-averaged flux. Time series of emigration sampled at a fixed position x along the bed were determined for all experimental runs.
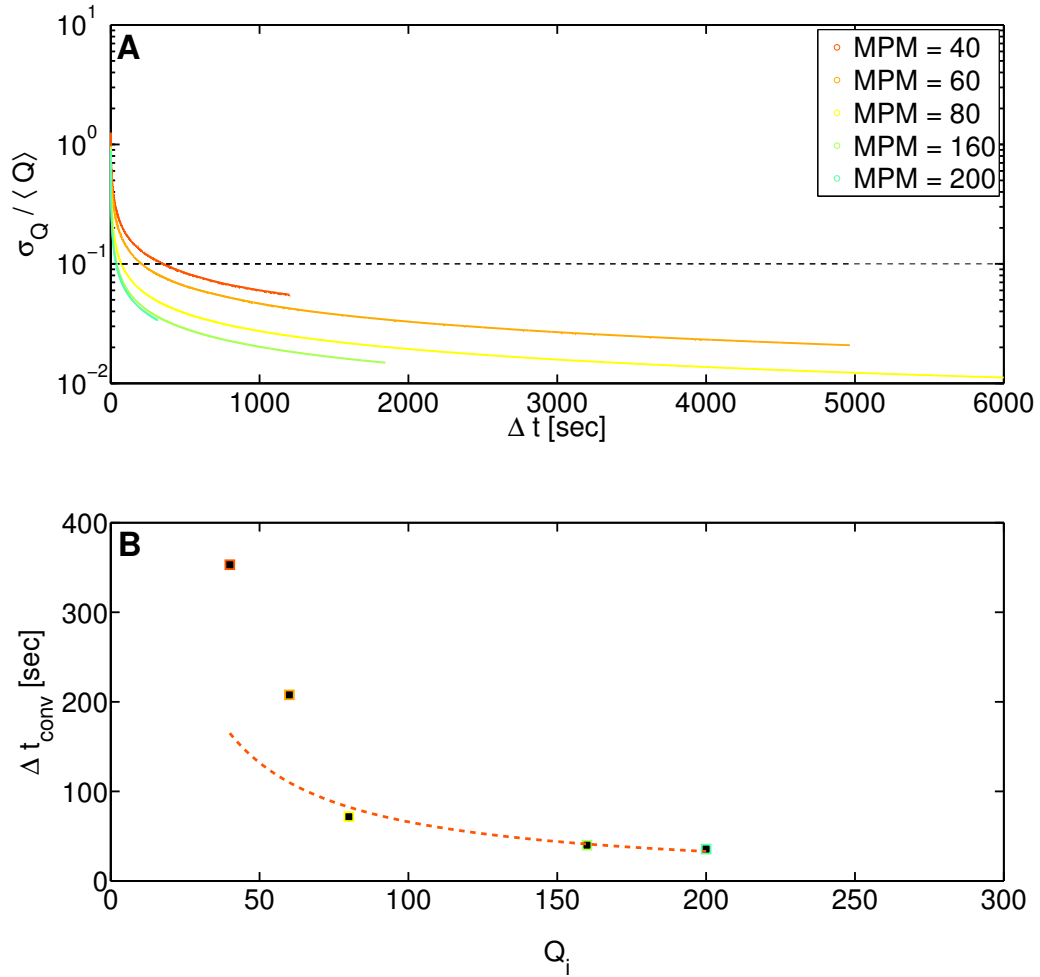
Figure 2.5: Determination of convergence time for experiments at all driving rates. (A) Standard deviation of an ensemble of samples over a given Δt. As Δt grows the the standard deviation decreases and approaches the threshold standard deviation. This value of Δt is interpreted to be the convergence time t_{conv}. The standard deviation is normalized by the mean emigration rate Q. Legend indicates feed rate in marbles per minute (MPM). (B) The time Δt_{conv} necessary for flux measurements to converge to a threshold standard deviation of 10 percent, as a function of the driving frequency in number of marbles per minute. The dotted markers are the actual observed convergence times, while the dashed red line displays the trend that one would expect the convergence time to take if it were simply a function of the feed frequency ($\Delta t_{conv} = 110/f_{input}$; see text for details).
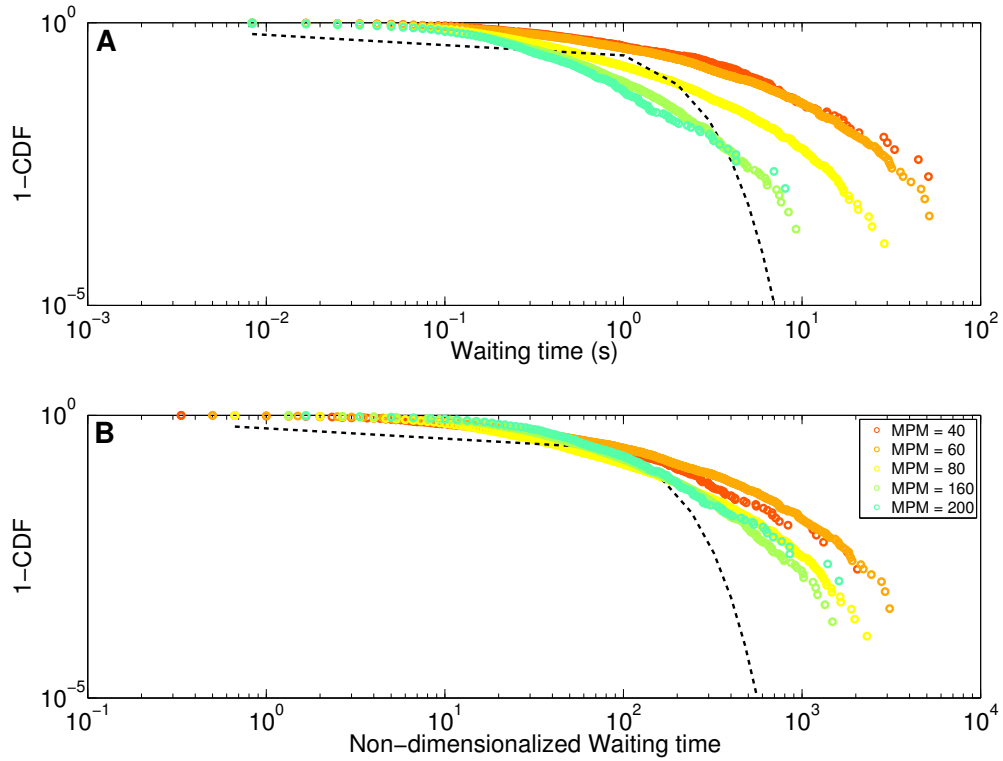
Figure 2.6: Complementary cumulative probability plots of waiting times between emigration events; (A) data for all experiments, and (B) the same data normalized by the driving frequency of each respective experiment. Expectation from a Poisson distribution is shown for comparison with dashed line. Legend as in figure 2.5.
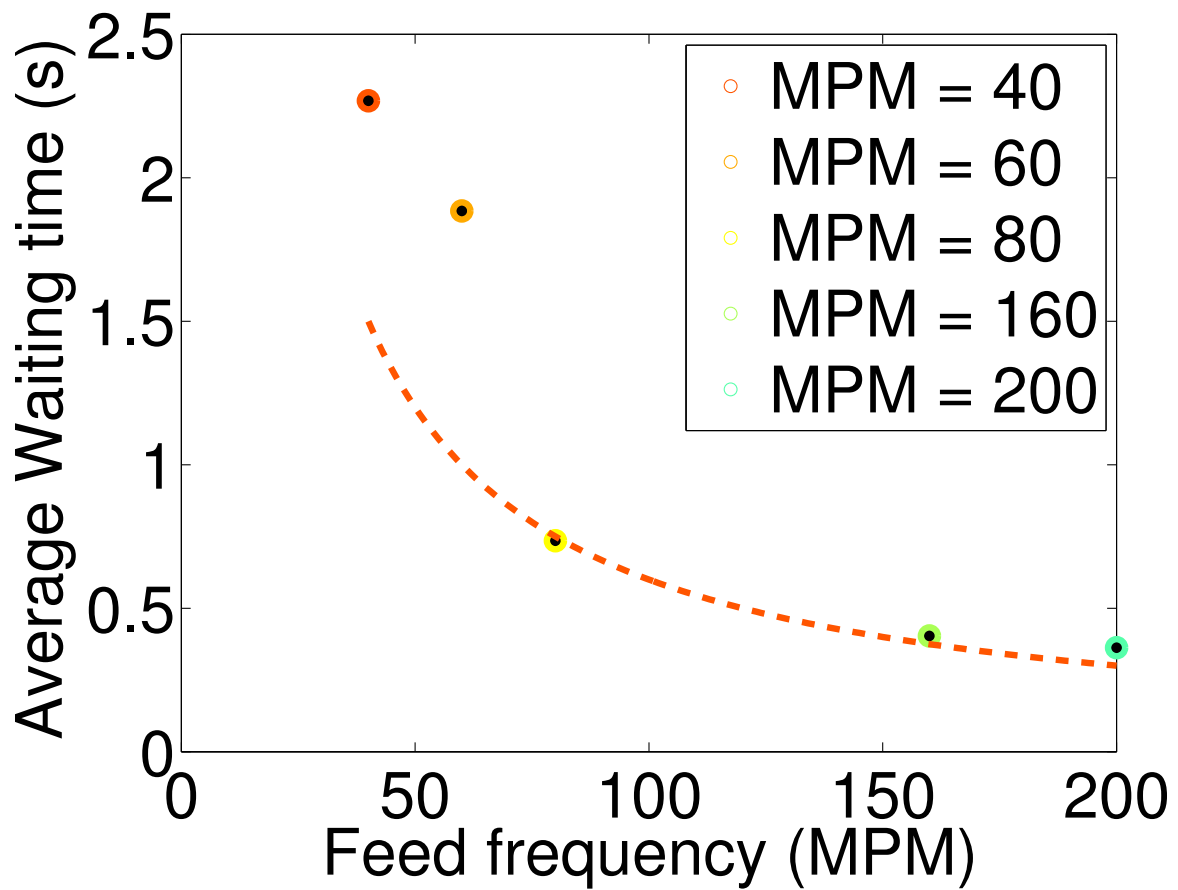
Figure 2.7: Relationship between the driving frequency f_{input}, and mean waiting time between observed emigration events W, for each experimental run. Dashed red line shows the expected relation that the mean waiting time is the inverse of the driving frequency, $W = 1/f_{input}$.
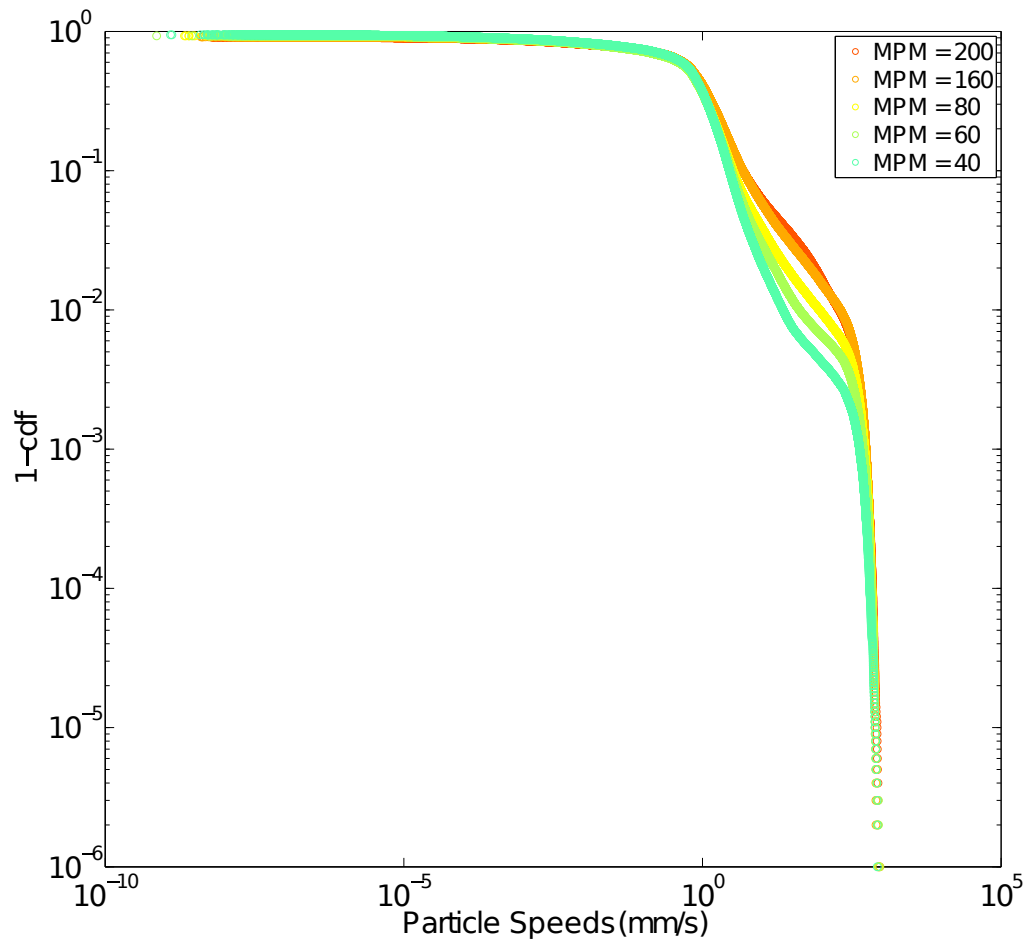
Figure 2.8: Complementary cumulative distributions of active particle speeds for all experiments. Legend as in figure 2.5.
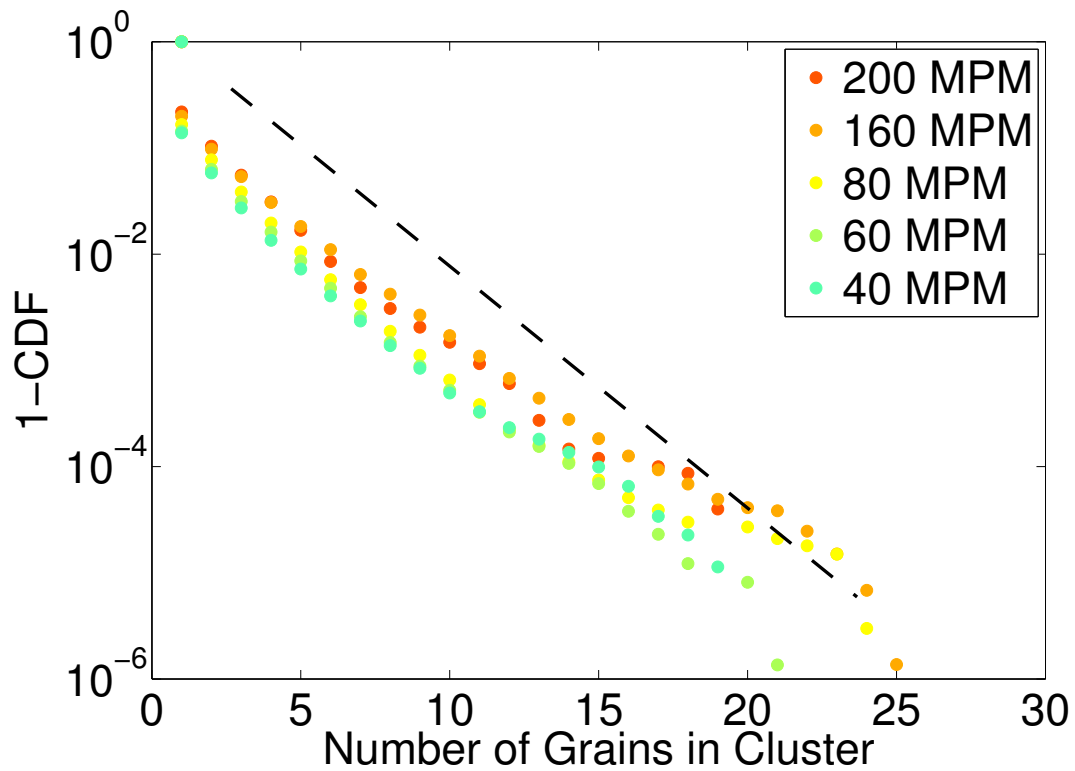
Figure 2.9: Cumulative complementary distributions of mobile cluster sizes, for each experiment at a different driving frequency. A cluster is defined as a group of mobile particles moving together in space. The dashed black line is an exponential trend, plotted for the sake of comparison. Note logarithmic y axis.
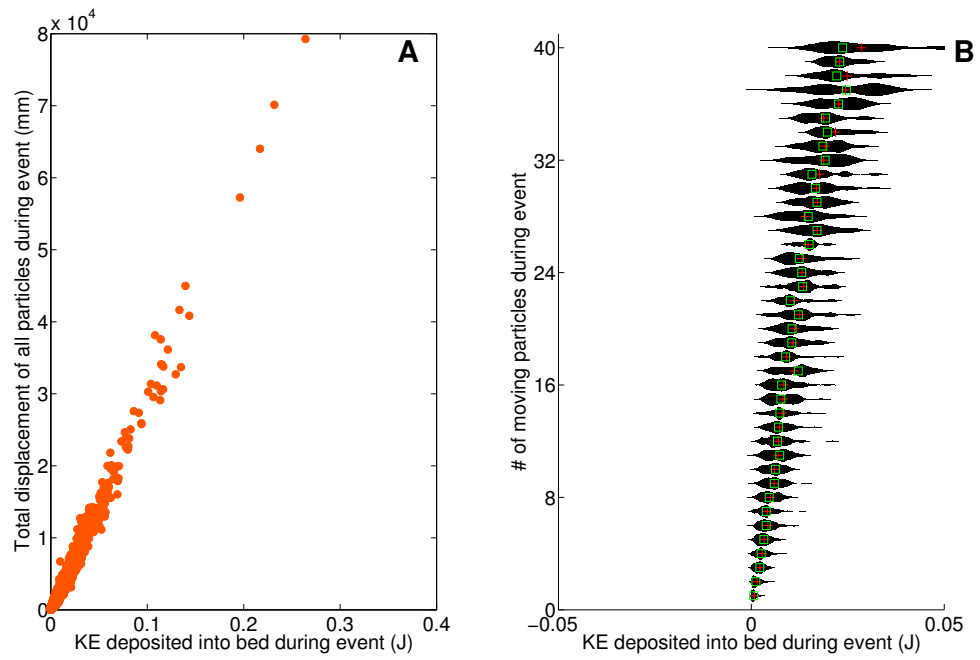
Figure 2.10: Particle mobility as a function of kinetic energy (KE) deposited into the bed for an event. (A) Cumulative displacement for all mobile particles during an event increases linearly with KE deposited. (B) Probability distribution of the amount of deposited KE necessary to entrain a given number of mobile particles. The mean of the distribution is displayed as a red cross, and the medians are shown as green squares.

Experimental flow parameters						
h (mm)	slope(%)	$\bar{u}_f$(m/s)	Sh	Fr	Re	St
33.6	8.5	.73	.14	1.3	10.7E3	>1000

Table 2.1: Mean flow conditions observed during the experiments. All values are means taken around the range of flow conditions observed over all experiments. h is the mean flow depth, $\bar{u}_f$ is the mean flow velocity, Sh is the Shields number, Fr is the Froude number, Re is the Reynolds number, and St is the Stokes number of the large diameter grains. St for the small diameter grains is also much larger than the viscously damped limit.

CHAPTER 3 : Correspondence between surface shear strength and critical shear stress in unconsolidated sand: lab measurements and potential field applications

Chapter to be submitted for publication as:

Lee, D.B., Qian, F., Nikolich, G., Koditschek, D., Jerolmack, D.J.: Correspondence between surface yield strength and critical shear stress in unconsolidated sand: lab measurements and potential field applications, Journal of Geophysical Research: Earth Surface, in prep, 2018

Abstract:

A soils response to wind stress is a multivariate function of grain-size, soil moisture, and compaction state among other factors. Understanding the spatial variation in this response is a problem that has been difficult to address due to the difficulty obtaining in situ measurements using portable wind tunnels. As a result, most models of dust and sand transport in aeolian environments still use a single value for the critical shear stress necessary for entrainment. New technologies such as the PI-SWERL wind erosion device and robotic platforms for measuring aeolian processes hold the promise of dramatically improving our understanding of the site specific variability affecting arid sediment transport. This work focuses on the potential of mechanical tests performable by semi-autonomous robots to rapidly provide maps of a soils susceptibility to wind erodibility over large areas. To accomplish this goal, a necessary first step is developing an understanding of the relationship between the mechanical response of a soil and its response to fluid shear. We develop a new test of a soil surfaces shear strength and empirically relate the soils mechanical response to its critical shear stress. This is done by varying a sand beds surface moisture and then testing the surfaces' threshold shear stress and shear strength. The relationship between the two is found to be roughly linear between 0-5 % moisture. At values higher than ~5 % we can only provide lower bounds on both threshold stress and shear strength. The increase in both measurements is hypothesized to be due to state transitions in the soil saturation

state. The results of this test demonstrate the feasibility of using robotic platforms to estimate variability in critical shear stress in a field setting.

3.1. Introduction

Human activities have accelerated the pace of desertification in many parts of the earth as a consequence of anthropomorphic climate change and land use patterns (*Dai*, 2013; *Wu and Ci*, 2002; *Reich et al.*, 2001; *Yong-Zhong et al.*, 2005). Increasing aridity increases the severity of dust storms, affects the biogeochemical cycle, and reduces the net ecological productivity of the earths land surface (*Schlesinger et al.*, 1990; *Rosenfeld et al.*, 2001; *Loye-Pilot et al.*, 1986; *Goudie and Middleton*, 2001; *Dregne and Chou*, 1992). In turn, these effects profoundly influences human health (*Watanabe et al.*, 2011). Determining how changes in arid landscapes will affect the sand and dust flux through a region is an important objective both scientifically and from a resource management perspective. Workers have documented documented that land use patterns can have an effect on dust emissions at both the site and regional scale (*Hoffmann et al.*, 2008; *Celik*, 2005; *Yang et al.*, 2003; *Neff et al.*, 2008; *Macpherson et al.*, 2008). In large part, human activity affects dust emissions in arid and semi-arid landscapes by changing soils erosive potential (*Bakker et al.*, 2008; *Yang et al.*, 2003). Part of this change comes from altering the response of the soil to fluid stress. The geomorphic changes arising from disturbance that have the potential to alter this response include compaction, changes in soil water content, alteration of infiltration patterns and a decrease in vegetation (*Liddle and Grieg-Smith*, 1975; *Webb*, 1983; *Webb and Wilshire*, 2012; *Kutiel et al.*, 1999)). For example, disturbing the extent of desert crust cover in an area can dramatically lower the threshold wind speed needed to transport sediment (see figure 3.1 and *Belnap and Gillette* (1998)).

Landscape scale heterogeneity introduced by topography, life, soil type, and soil state introduces multiple feedbacks to the sand and dust transport dynamics of an area (*Okin et al.*, 2006; *Yan and Baas*, 2017). Our understanding of the nature and extent of these feedbacks is still incomplete. In part, this incompleteness is because of the multi-faceted nature of the problem. Another issue is that patch scale dynamics are still poorly constrained and highly variable. Transports site dependent nature means that collecting the large amount of field

37

data necessary to constrain the problem remains challenging; though recent developments hold the promise of remedying this issue by enabling more rapid data collection (*Qian et al.*, 2017; *Vrieling*, 2006; *Etyemezian et al.*, 2007). One area where notable progress has been made is the effect of vegetation on wind. Plants raise the threshold wind speed needed for sand and dust transport (*Lancaster and Baas*, 1998; *Wolfe and Nickling*, 1993, 1996). These studies have been able to relate the aerodynamics of various plant types and communities to variability in the shear experienced by the soil surface. Being able to predict vegetation induced wind shear stress modifications is a crucial step and an important addition to models of a landscapes erosive potential (*Kimura and Shinoda*, 2010).

However, the soils response to this modified stress is another important factor that hasn't received as systematic a treatment. Initiation of transport is often modeled using a single threshold criterion for the critical shear stress (τ_c). This assumption neglects the real world variability in τ_c for different types of desert soils (*Shao et al.*, 1993). Figure 3.1 illustrates that fluid velocities associated with transport initiation can vary by as much as a factor of two (and possibly more) even for samples that have similar grain size distributions. In this case, the difference in erodibility comes from the extent of soil crustal development, but the erosive response to fluid shear is also likely to co-vary with moisture, compaction state, and other factors that display high heterogeneity in the real world. As a strong filter on transport, the threshold of motion is a key component of erodibility. Figure 3.1 as well as the work of *Gillette et al.* (1980) and others also point to the threshold of motion showing a large degree of variability in the field.

Understanding the spatial variation in soil erodibility, as well as the factors controlling this variation, is necessary to accurately model sediment transport dynamics in real world environments (*Webb and Strong*, 2011; *Cornelis and Gabriels*, 2003). Traditionally, aeolian scientists use in-situ wind tunnels to perform erosion tests (*Gillette*, 1978; *Gillette et al.*, 1980; *Shao et al.*, 1993). This method is inherently limited in spatial resolution primarily due to a lack of portability. To ensure reasonable turbulent stresses, the tunnels are large,

and this factor leads to a high time cost in the installation, deployment, and size of these devices. In addition, the wind tunnel averages over a length scale of the terrain that itself might contain significant variability. New devices to assess a surfaces susceptibility to wind erosion have started to be explored (*Etyemezian et al.*, 2007; *Sweeney et al.*, 2008; *Goossens and Buck*, 2009). These devices offer the advantage of reduced size, greater portability, and automated detection of the wind speed at which course and fine size fractions begin to move.

A crucial next step lies in being able to assess erodibility at fine resolution over a large area in a field setting. Beyond giving some indication of a locations susceptibility to wind erosion, it is also important to indicate how the soil surface is likely to respond to the mechanical disturbances that are a common component of human land use. If enough of this data was gathered, a soils geomorphic response to different types of disturbance could begin to be modeled. The data would allow us to measure feedbacks between the response of a soil, the time evolution of its erodibility, and the net erosion that occurs in a field site under different conditions. Maps of soil erodibility could also be coupled to knowledge of the distribution and types of plant communities in an area. This coupling would allow the feedbacks between plants, soil, elevation, and aeolian processes to be studied over a large spatial extent.

Autonomous and semi-autonomous data collection methods hold great promise for allowing us to create these maps. Recently, a semi-autonomous robotic platform known as RHex has demonstrated a capability for gathering rapid, high-resolution data in aeolian settings (*Qian et al.*, 2017; *Roberts et al.*, 2014a,b). Figure 3.2 shows RHex in active deployment. It has recently been shown that RHex can be used to estimate a soils erosive response to mechanical disturbance by examining the resistive force of the soil in response to a probe undergoing constant displacement (*Qian et al.*, in prep). The rapidity with which different types of mechanical tests can be performed, the large range of spatial scales that can be mapped, and the promise of full autonomy provides a strong motivation to more fully

explore the potential of using RHex to map variations in erodibility.

A confounding factor in the use of RHex or another robotic platform to assess the threshold of motion is the non-obvious relationship between mechanically probing a soil and the soils response to turbulent fluid shear stresses. There has been some work examining the relationship of τ_c and shear strength. Existing studies are conducted in highly cohesive, fully saturated sediments and look at the relationship between subaqueous stresses and shear strength among completely different soil types in the lab, or in-situ where natural variation in soil state and type is to be expected (*Léonard and Richard*, 2004; *Meng et al.*, 2012; *Kimiaghalam et al.*, 2016). A review by *Léonard and Richard* (2004) found that linear scaling between critical grain shear stress and shear strength in cohesive soils is common.

The linear relationship between τ_c and shear strength in the cohesive setting of rills and mudflats, along with the possibility of relating the two stresses for soil types found in aeolian settings has motivated the present work. In this study, an empirical attempt to test the relationship between the threshold of motion due to wind stress and a test of a soil surfaces shear strength is performed. We develop a test of shear strength that can be performed by a robotic probe similar to the one previously deployed by RHex. The tests are performed in the lab using a consistent grain-size with the surface moisture of the soil being the control variable. We present the observed relationship between τ_c and surface shear strength and discuss future field applications of the newly established method.

3.2. Methods

Moisture was used as the primary control variable on the erodibility. One advantage of using moisture is its long recognized importance as a variable affecting soil erodibility in the field, particularly in arid areas (*Chepil*, 1956; *Fécan et al.*, 1998). To isolate the control of soil moisture on erodibility, we performed laboratory experiments with a controllable mister system that allows us to systematically vary soil moisture on the sand surface. The mister system, shown in figure 3.3, was mounted on a linear actuator and swept back and forth

to prevent variance in the spatial distribution of surface moisture. Tests were performed to ensure the misting system generated sand beds with a consistent enough moisture. Before wetting, beds of sand were prepared by pouring sand into the bed and then leveling the surface with a straight edge. After each misting cycle, we measured the soil moisture using a Decagon capacitive moisture sensor. Figure 3.7A shows the soil moisture distribution after various numbers of misting cycles in the sandbox used for the shear strength tests. Figure 3.7B shows the average soil moisture across the entire sandbox as the number of misting cycles increases. The Decagon moisture sensor (and other capacitive moisture probes) integrate over the depth of the probe. Although this was not an obstacle when determining the spatial homogeneity of the misting device, in the actual experiments, it was decided that a non-depth integrated moisture that represents moisture as close to the surface as possible was desired. As such, a Speedy$^®$ moisture tester was used to measure surface moisture during the experiments. For each moisture test, six grams of sample was scraped as close to the surface as possible and then tested. The act of disturbing the surface introduces a degree of uncertainty into the measurement that was found to vary from 0 - 0.5 % moisture. Throughout the rest of the paper, moistures are reported as percent wet weight.

The foundation of the proposed method used to characterize soil erodibility is the hypothesis that soil susceptibility to erosion and stability under external perturbations (such as vehicle disturbance, wind shear, or other disturbance) can be characterized through measurements of the shear strength of the substrate. To test this hypothesis, we examined a potential correspondence between a soil surface's shear strength and its threshold shear stress. The measurement of the shear strength was conducted using an idealized probe (pictured in figure 3.3) inserted into a bed of sand of medium grained sand (grain size distribution is shown in figure 3.6) scored with a predetermined groove to ensure a consistent contact geometry. The sand bed was 30 cm long by 11 cm wide. The probe was inserted into the center of the box to avoid boundary conditions. This probe was a 37 mm long cylinder 12 mm in diameter attached through a 17.5 cm lever arm to a direct drive motor provided by Ghost Robotics. The direct-drive motor didn't have gearboxes so it responded sensitively to

external torques and forces. The motor design allowed for the resistive force of the sand in response to the applied torque of the motor to be measured. The resistive force is modeled as being normal to the surface area of the cylinder that is in contact with the sand bed. This force is converted into a stress by dividing by the effective surface area of the probe that is in contact with the bed at the moment of failure.

The protocol for applying force to the sand bed and determining a shear strength was as follows: First, the probe tip was submerged 4 mm relative to the sand surface. The probe was positioned strictly normal to the sand at position $pi/2$ defined by the referenced frame pictured in figure 3.4. A groove in the sand surface ensured that there were no compressive forces on the probe. This corresponds to the 'Time A' schematic in the subpanel of figure 3.4. After positioning, the force output of the motor was gradually increased. The sand deformed, though only slightly, in response to this force and the probe shifted off being strictly vertical by 0-.1 rad. Eventually, the force output reached a peak that represented the peak resistive force of the sand before failure. An example can be seen in the 'Time B' schematic of figure 3.4. Next, a sudden failure of the sand bed occurred and the probe 'kicked out' of its approximately vertical position. An example can be seen in the 'Time C' schematic of figure 3.4. This test was then repeated for different soil surface moistures ranging from 0-18 % percent (soil moisture is reported in the study as percent wet weight of soil sample). Because the test was a destructive test of the sand surface, after each test a new, dry bed of sand was prepared and brought up to a given percent moisture within the range being tested.

In practice, a more sophisticated probe design, such as a modified version of the leg described by *Kenneally et al.* (2016) and pictured in figure 3.2 is likely to be employed in the field. This allows for the robot to control the specifics of the probe entry into the sand surface and gives the robot the flexibility to perform other mechanical tests, such as those described in *Qian et al.* (in prep). However, for our purposes, the probe design we used in the present study was deemed sufficient to conduct the shear strength test described above.

Given that the quantity desired (surface peak shear strength) was a highly local value in an unconsolidated, low-cohesivity soil under virtually no confinement, our definition of the shear strength is by necessity a working definition. However, we believe it captures the key feature of a peak shear strength (namely the loss of rigidity of the area being probed). It is worth noting that the test developed here appears to work well for the pure sand used in the study. This result is not the case with in-situ vane testers which are traditionally only used in soils which exhibit a high clay content. The sensitivity of the new test is possibly because the design of the motor allows for low magnitude, controlled forces to be applied to the surface and read out from the motor at high resolution in comparison to hand deployed shear vanes. This resolution and range allows for small differences in the peak shear before failure to be reliably detected in the sandy soils used.

We compared the results of our measurement to estimates of τ_c necessary to initiate saltation. These estimates were obtained by the Portable In Situ Wind Erosion Laboratory (PI-SWERL) described in (*Etyemezian et al.*, 2007). Figure 3.3 shows the PI-SWERL situated on the 1 x 1 x .15 m sand bed used for the wind shear testing. Given the large volume of sand involved in creating a testing bed for the PI-SWERL and the minimal disturbance that the short-time ramping protocol had on the bed surface compared to the shear strength test, the sand in these tests was only replaced after the surface was deemed to have been disturbed enough from all the previous tests. The sand used in this bed was the same as that used in the shear strength tests (see figure 3.6 for the grain size distribution). The version of the PI-SWERL employed was outfitted with two optical gate sensors near the annular ring that generates shear inside the device. Peak voltages generated by the optical gate occur when saltating grains occlude the gate above a threshold area. Optical gate peak area is then obtained by integrating the area of observed optical peaks over 1 second. Shear stress was increased within the PI-SWERL by gradually increasing the RPM the annular ring shearing the sand surface. The RPM ramp protocol is shown in figure 3.5. Past a certain RPM/shear stress the optical gate peak area increases dramatically (figure 3.5). This dramatic increase was interpreted as the beginning of sustained saltation. The

RPM value associated with the optical gate peak area value of 5 was interpreted to be τ_c. A sensitivity analysis revealed that within the parameter range 5-17 for the optical gate area, the observed trend in τ_c was relatively invariant. The RPM associated with this threshold optical gate area was then converted to shear stress using the empirical relation given in the PI-SWERL manual:

$$\tau = -4.05 \times 10^{-12} R^3 + 5.35 \times 10^{-8} R^2 - 2.20 \times 10^{-5} R + .0351 \qquad (3.1)$$

where τ is the friction velocity and R is RPM. It is important to note that τ_c estimated by the PI-SWERL may not be strictly analogous to the estimate provided by a straight line wind tunnel (*Sweeney et al.*, 2008). Though the fluid stress generated by the PI-SWERL is not strictly 'natural,' it was deemed appropriate enough for this study. This conclusion is not unreasonable considering that we were concerned with the shear associated with the onset of transport of the saltating layer and not the equilibrium transport conditions that would be most heavily affected by the deviation of the PI-SWERL's design away from that of a straight line wind tunnel. The shear stress values generated by the PI-SWERL were sufficient to explore the existence of a relationship between mechanical and turbulent fluid stresses.

Inherent in misting an initially dry surface is the infiltration that will occur as added water seeps into the bed. The sensitivity of the measurements to the amount of time that added water has been allowed to infiltrate onto an existing sand bed of a given moisture was tested. This test was done using the PI-SWERL by taking τ_c for beds of sand where added water had been allowed to infiltrate for ninety minutes or greater. These shear stress values were then compared to τ_c observed in beds of sand where added water was only allowed to infiltrate for five to ten minutes before taking the measurement. Figure 3.8 shows the existence of what appear to be two distinct groupings for measured τ_c as a function of surface moisture that is dependent on the amount of infiltration time that samples were

allowed to undergo before measurement with the PI-SWERL. To remove this effect reported measurements for both τ_c and the shear strength were all conducted a maximum of fifteen minutes after the most recent misting cycle.

3.3. Results

Figure 3.9 shows the observed trend in both shear strength and τ_c. From 0-5 % surface moisture both quantities appear to increase linearly with increasing surface moisture. After 5 % surface moisture, both τ_c and the shear strength continue to increase. However, there appears to be more variance associated with the increase in τ_c past 7 % surface moisture. This variance is possibly an effect of the large interrogation area of the PI-SWERL being able to probe patches of fine sand on the surface. These patches would be associated with a lower τ_c on average and lead to local scour patterns. Above 5 % surface moisture there appears to be a distinct jump in the shear strength with a clustering of values from 5 % to 7 %.

There is another dramatic jump in the shear strength at ∼7 % surface moisture. This jump in the shear strength is consistent with previously proposed transitional zones between the capillary and funicular states in partially saturated soils (*Schubert*, 1975). The large increase in shear strength at values above 7 % made it untenable to gather data for higher percent moistures because the torque output of the motor reached its limit. Two attempts to measure the shear strength of the soil near 7 % moisture were stopped near the upper limit of the torque output of the motor. These points are color-coded red in figure 3.9 and represent a lower limit for the shear strength at this percent moisture rather than an actual value for shear strength. A similar increase in τ_c also caused us to exceed the upper limit of the shear stress generatable by the PI-SWERL at roughly 7 % moisture. The majority of measurements taken at the higher % moistures do not represent actual values for τ_c but bound the lower limit for τ_c. There were two values above 10 % surface moisture where τ_c was successfully measured. The reemergence of two quantifiable values at moistures above 10-12 % is likely an artifact of uncontrolled for variations in the sand bed preparation protocol, the

45

large interrogation area of the PI-SWERL, and the large fluctuations in turbulent stresses associated with the highest stress the PI-SWERL is capable of generating.

As the surface approaches complete saturation the shear strength was observed to approach a value similar to the dry condition. This finding is consistent with observations of how bulk tensile stresses in granular piles rapidly decline as saturation is approached (*Schubert*, 1975). One significant qualitative difference was observed between the two conditions upon failure of the sand surface. In the dry case, the 'kick out' of the probe from submergence in the sandbed is associated with grains leaving the bed surface. In the fully saturated case, the 'kick out' is only associated with a puddling of grains near the location where the probe leaves the surface. Conducting a similar test of completely saturated conditions was not possible with the PI-SWERL. Even if significant grain motion occurred at the surface, if it was similar to that observed during the shear strength test, there would be no grains leaving the film of sand and water at the surface. This observation means attaining saltation measurable by the optical gate is not possible.

It was observed that the stress applied to each grain in contact with the probe at yield appears to be of the same order as the grain scale τ_c estimate provided by the PI-SWERL. This can be seen by taking the average grain size (D_{50}) of the sand used in the study and calculating an average number of grains that would be expected to be in contact with the probe. An average per-grain stress at yield can then be obtained by dividing the shear strength by the average number of grains in contact. When this calculation is done for the dry case, the per grain stress at yield is .75 Pa. This result differs from the dry τ_c estimate reported in figure 3.9 by a factor of three.

3.4. Discussion

The roughly linearly increasing trend in surface shear strength at different degrees saturation in the pendicular (roughly 0-5% for grain sized used) and funicular (5-90%) regimes are consistent with the increases in tensile strength reported experimentally by *Lu et al.* (2007)

and *Schubert* (1975) for medium sand with a wide size distribution. This finding provides support that the increase in the strength of the sand comes from an increase in capillary pressure as the sand becomes more highly saturated. This increase arises first from an increase in the liquid bridge volume causing larger Laplace pressures in between bridged grains (*Scheel et al.*, 2008). In the pendicular regime, capillary pressures arising from bulk pressure gradients within the media are superimposed onto forces associated with liquid bridges leading to a further rise in strength (*Schubert*, 1975). Our observation of a return to near-dry shear strength values with total saturation is also consistent with this picture.

The large rise in threshold shear stress with moisture validates the observation of *Bisal and Hsieh* (1966) and *Wiggs et al.* (2004) that under most conditions soil above 4-5 % moisture is difficult to erode by wind. Our observed linear trend is also consistent with the empirical results reported for τ_c of coarse sands of various wetness by *McKenna-Neuman and Nickling* (1989). Though their reported trend only goes from 0-2 percent gravimetric moisture. This determination implies that moisture is the dominant factor controlling the observed increase in the shear stress rather than unaccounted for variations in compaction state or other factors. One difference between the τ_c measurements and the shear strength is that, near full saturation, the values for τ_c remain high. The difference is likely attributable to the absence of grains leaving the sand surface in the case of yielding in the fully saturated test. This absence would imply that the τ_c necessary to cause surface motion for fully saturated beds is similar to the dry case. However, additional force is required to introduce complete separation of the grains from the sandbed. In the fully saturated case, grains will experience increased viscous dissipation as well as a suction pressure that is generated as the grain begins to leave the film of sand and water. This is consistent with the behavior observed in spheres rebounding off of thin viscous films (*Barnocky and Davis*, 1988).

The proposed mechanism for the increase in both τ_c and mechanical strength of the soil with % moisture in the work discussed above is increasing capillary pressure. The correspondence between the two soil properties directly seen in this study lends further credence to the idea

that, in the case of soil moisture, both our shear strength test and τ_c are controlled by the same underlying physical cause. This hypothesis is further supported by our observation that the per-grain stresses experienced at the transition to dynamic behavior appear to be of the same order. The similarity in stresses would imply that, for the case of surface moisture, using a test of the near-surface shear strength as a proxy for τ_c is valid.

A possible reason for the larger variability in τ_c at higher percent moisture versus the shear strength measure is that the mechanical forcing that generates the shear strength has none of the variability associated with the turbulent forcing associated with the shear stress estimate. Given that fluctuations in boundary stress associated with turbulence are likely to affect entrainment (especially at the high Reynolds numbers associated with generating higher stresses in the PI-SWERL) it is likely that a growth in variance around the time-averaged turbulent stresses leads to increased scatter in any estimate for τ_c that relies on time-averaged flow velocities (*Diplas et al.*, 2008; *Durán et al.*, 2011; *Weaver and Wiggs*, 2011).

The influence of infiltration time on the observed trends in τ_c seen in figure 3.8 seem to support the idea proposed by *McKenna-Neuman and Nickling* (1989) that a soils matric potential could be a more important control of τ_c than actual moisture content. In this work, the surface moisture was used because it was considered to be more realistically attainable by the robotic platform that is the target for the deployment of the proposed shear strength test. Also, because of the challenges associated with measuring near-surface matric potential, most existing studies that examine the relationship between τ_c and moisture look at surface moisture rather than tension (*Bolte et al.*, 2011; *Wiggs et al.*, 2004). Further work to establish whether or not the response of the yield-strength test and measured τ_c remain consistent for different near-surface matric potentials is necessary.

It is an open question if surface shear strength and τ_c respond similarly to other variables that control soil state. For example, figure 3.1 and previous work point to the strong effect of desert crusts on the threshold of motion. Does the mechanical response of the

soils near-surface behave in a similar way to τ_c for desert crusts? Compaction also seems to play a large role in the erodibility of barchan dune surfaces (*Qian et al.*, in prep). Compaction has been hypothesized to influence the critical yield stress of bedload material in rivers (*Charru et al.*, 2004). It has also been documented that repeated compaction events can influence the rheology of granular materials (*Richard et al.*, 2005). Compaction can be controlled in the lab (*Gravish and Goldman*, 2014) and future work might look at the response of variably compacted materials to both wind stress and our test of surface shear strength. More detailed information into this relationship should allow us to begin to deconvolve the relative contributions of moisture and compaction state on the erosive response of unvegetated desert surfaces. Cohesivity is another important state variable that determines the mechanical response of a soil. The work establishing relationships between shear strength and τ_c in extremely cohesive sediments is encouraging (*Meng et al.*, 2012; *Léonard and Richard*, 2004). It is possible that the effect of cohesivity will remain similar under wind-stress and under partially saturated conditions.

Though further developments could extend the applicability of the proposed techniques to other settings (such as desert crusts or soils with significant organic matter), the existing data show that the method could already be applied at some field sites where soil moisture is hypothesized to be the dominant control of variability in the threshold stress, such as most beaches (*Jackson and Nordstrom*, 1997). Surface moisture is recognized as one of the primary control variables of τ_c in the field. However, the increase in τ_c associated with a given rise in moisture appears highly site dependent and difficult to model (*Webb and Strong*, 2011). Rapid, direct estimates of τ_c provided by RHex or a similar robotic platform could overcome this problem. Given the rapidity with which the shear strength test can be performed, one practical way to field verify its ability to assess changes in sediment flux related to variation in τ_c would be to attempt to relate variations in measured sand flux to changes in surface shear strength in the spirit of *Wiggs et al.* (2004).

Improvements to the probe used in *Qian et al.* (in prep) would enable the shear strength

test described here to be performed in conjunction with the constant displacement test that has already shown potential in being able to characterize the erosive response of different substrates in the field. Figure 3.10 shows the design of a probe that is capable of performing both types of soil tests. Modifications to the probe tip to more directly engage the sand surface rather than integrating the surface with several millimeters of sub-surface are also under consideration.

3.5. Conclusion

The main motivation for this study arises from the arrival of robotic platforms such as RHex that are capable of semi-autonomous deployment in aeolian field settings. These platforms enable rapid, high-resolution mobile data collection and have the potential to be a valuable tool in addressing under-constrained aspects of aeolian processes in the field. Soil erodibility is one such process and understanding variations in erodibility is crucial in creating accurate models of sediment transport (*Webb and Strong*, 2011). The ability of RHex to perform rapid in-situ tests of a soils mechanical properties has recently been demonstrated (*Qian et al.*, in prep). Coupling this ability to other environmental parameters obtainable by RHex (saltation flux, wind speed, vegetation extent) could lead to a greater understanding of the relationship between erodibility and observed sediment transport. Thus, it is highly desirable to develop rapidly performable tests of erosive response that can be performed by RHex.

This study presents the results of one newly developed test in the form of a proposed measure of a soil surface's shear strength. We compare a shear strength to the value of shear stress associated with incipient motion and find evidence for a similarity in scaling between the two properties. A linear relationship was observed for the two properties between 0-7 % moisture. After roughly 7 % moisture the ability of our measurement devices to measure both τ_c and shear strength is exceeded and only a lower limit can be provided. Upon approaching complete saturation the observed shear strength approaches that seen for dry values. The behavior of both measurements is consistent with the theory that they are

controlled by an increase in capillary pressure as the degree of saturation is increased. We believe that this test is the first demonstrating a relationship between τ_c and shear strength for sandy soil of different degrees of saturation.

| Loose sand: 4.6 m/s | Thin crust: 7.1 m/s | Thick crust: 8.7 m/s |
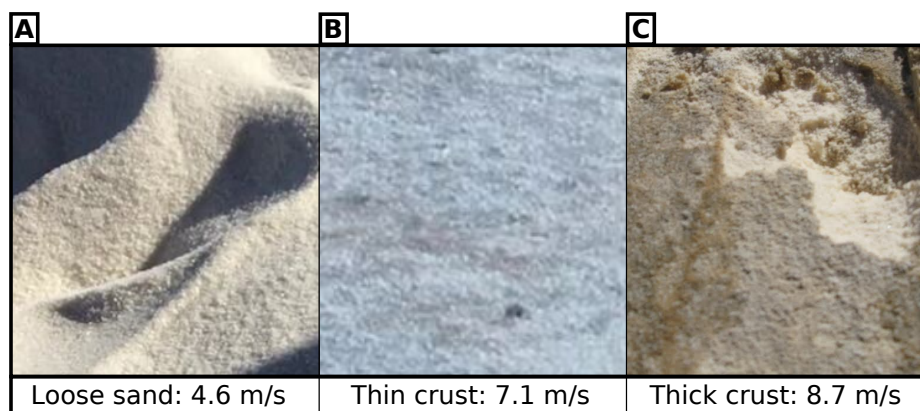
Figure 3.1: Height averaged wind speed measurements observed at the initiation of saltation for different types of sand cover in White Sands, NM. Measurements were collected at the outlet of a portable wind tunnel and are included for relative comparison. Here, the variation in observed wind speed appears determined by the extent of desert crust development on the surface. Loose sand (panel A) has the lowest wind speed associated with saltation. The requisite speed for saltation associated with a thick desert crust (Panel C) is higher by roughly a factor of two.

Figure 3.2: An example of the recently developed RHex robotic platform deployed in the field in White Sands, NM. The robot is outfitted with a probe assembly mounted near the front of the body. The probe uses force feedback from two motors to obtain force and position output that can be used to perform various mechanical tests of the sand surface.
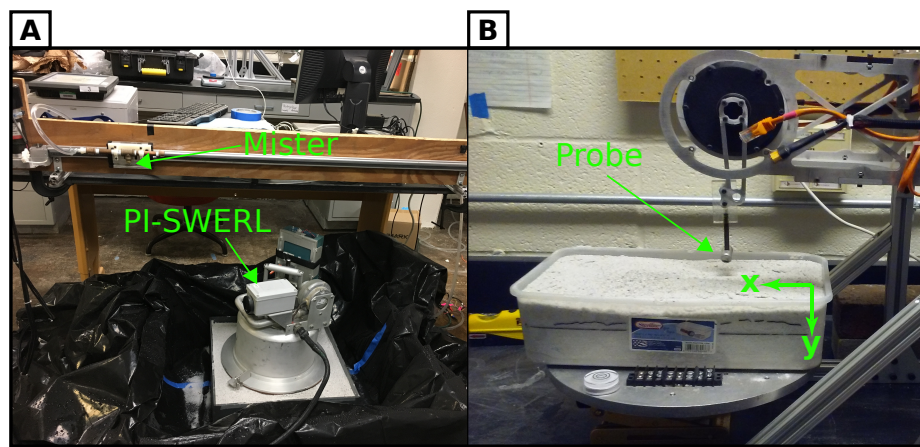
Figure 3.3: Photographs of the lab equipment used in the study. Panel A: the mister and the PI-SWERL. Mister is mounted to a linear rail and sprays sand beds at a constant rate to ensure a consistent surface moisture profile. PI-SWERL is shown sitting on the 1 x 1 x .15 m bed of sand that was used to estimate τ_c. Panel B: The probe used in the current study. The force output of the probe is given in the Cartesian reference plane inset into panel B. For a more in-depth schematic of this test see figure 3.4
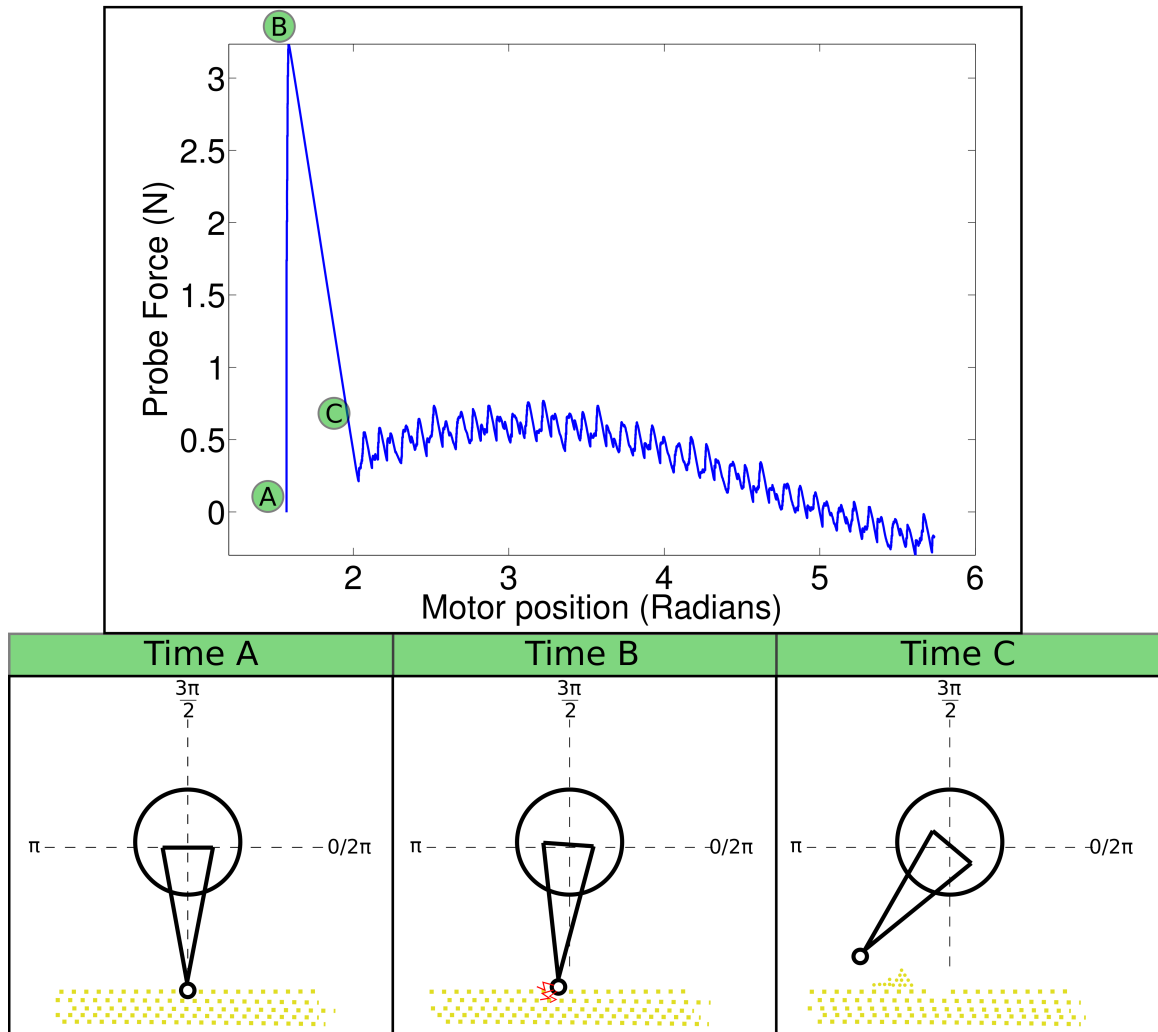
Figure 3.4: Top panel shows an example of the force output of the probe used in the current study. The A,B, and C labels inset into this output are linked to schematics in the bottom panel showing the probe output at times A,B, and C. At time A, approximately 1/3 of the probe tip is submerged at position $\pi/2$ and the force is beginning to ramp up. At time B, probe is slightly shifted away from $\pi/2$ because of deformation of sand (angle exaggerated). This time corresponds to peak force output by the probe in response to the resistive force of the sand. This peak force immediately before the sand bed fails is defined as the shear strength of the sand. At time C, the sand has failed and the probe tip has kicked out above the sand bed.
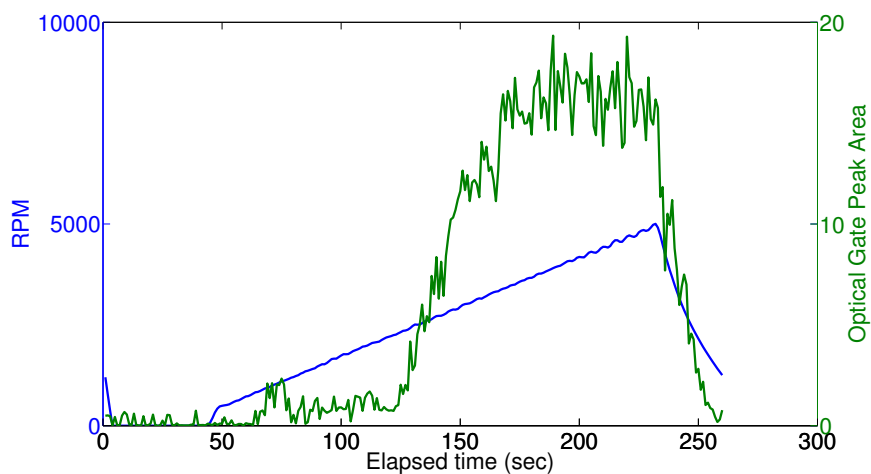
Figure 3.5: An example of the raw output of the PI-SWERL used to determine a threshold for saltation. As the RPM of the PI-SWERL increases past a threshold the integrated optical gate output from the PI-SWERL rises abruptly signifying saltation. Optical gate peak output above a threshold is integrated over 1 s to obtain the Optical Gate Peak Area pictured above.
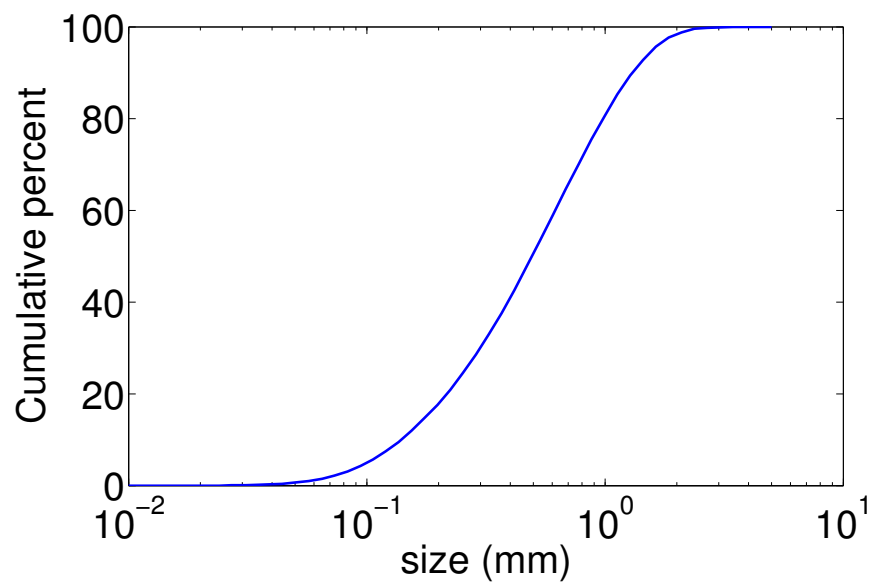
Figure 3.6: Cumulative grain sized distribution of the sand used in the current study ($D_{50} = 0.56mm$). Qualitatively, sand was fine to medium size with a small course size fraction overlying the main distribution.
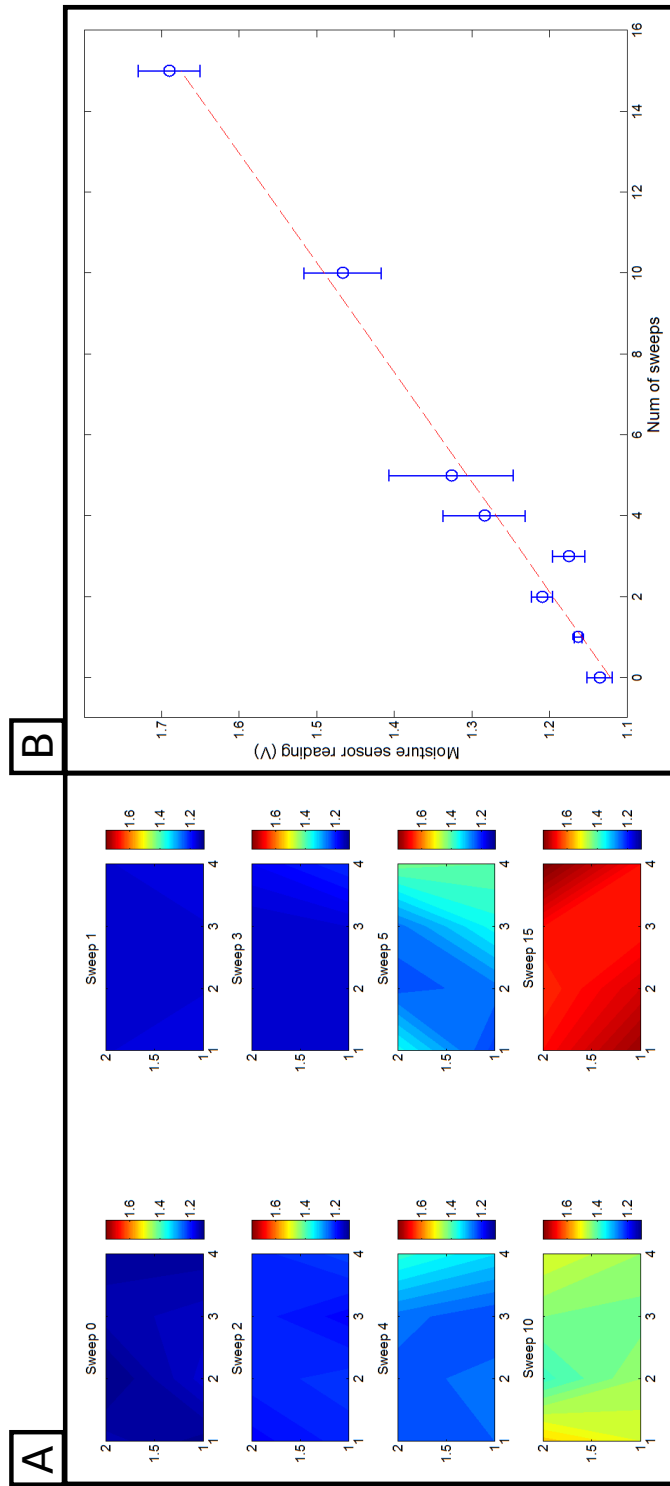
Figure 3.7: Left panel shows the spatial distribution of moisture interpolated from nine evenly spaced sample points distributed throughout a sample box filled with sand. The right panel shows the distribution of moisture measured by a resistive moisture probe for these points with output in volts. Moisture measured by the probe is proportional to the number of sweeps of the mister.
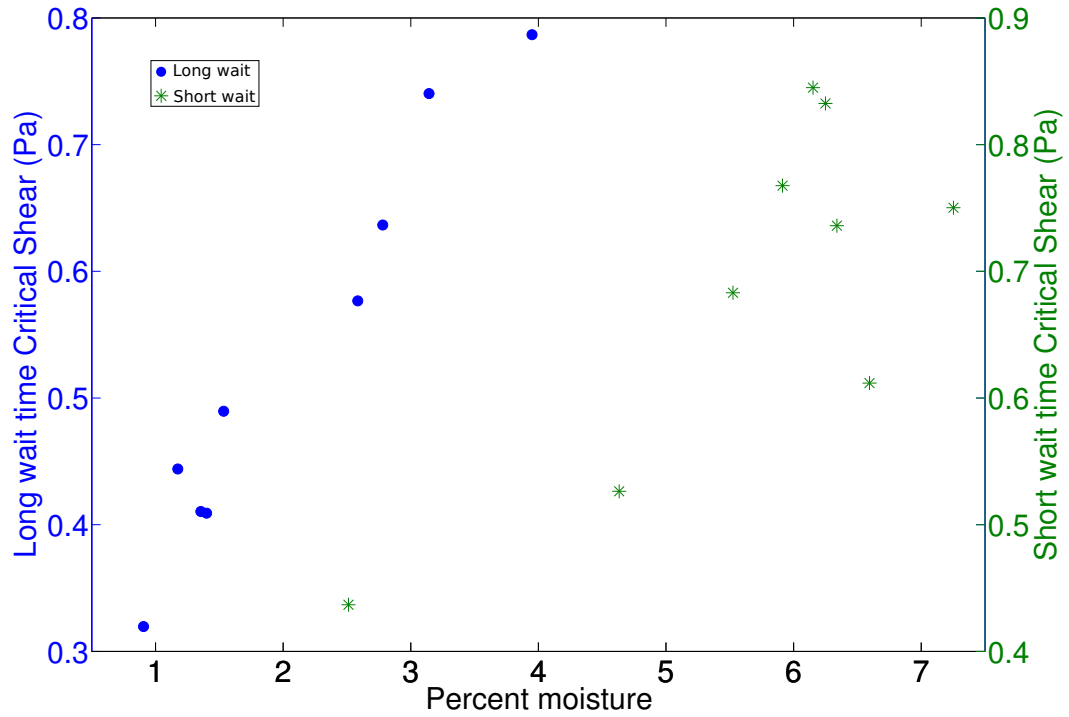
Figure 3.8: Infiltration time dependent differences in τ_c (estimated by the PI-SWERL) against surface moisture. Blue circles (long wait) depict τ_c for sand beds that have undergone infiltration times of 90 minutes or longer after wetting. Green stars (short wait) show τ_c for beds with infiltration times of 5-10 minutes. Distinct groupings of the two measurements suggest that τ_c of the sand surface is controlled by sub-surface saturation state as well as surface moisture.
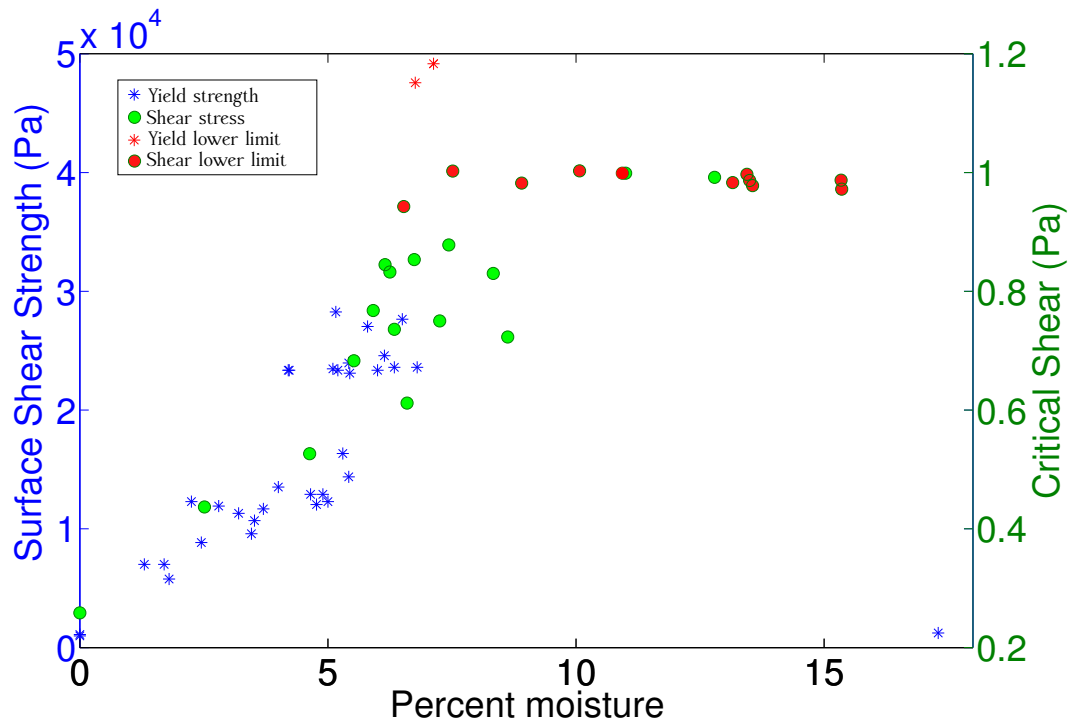
Figure 3.9: A comparison of surface shear strength as measured by the test described in figure 3.4 and the estimate of τ_c provided by the PI-SWERL. From 0-6% the two appear to be roughly proportional. There is a jump in both τ_c and shear strength above 6 % moisture. This result is evident by the lower limit points colored in red, which indicate that true measurements were unobtainable for the higher percent moisture values (except for outliers in τ_c at 11 and 13 %). At the percent moisture corresponding to full saturation of the surface, the measured shear strength approaches its dry value.
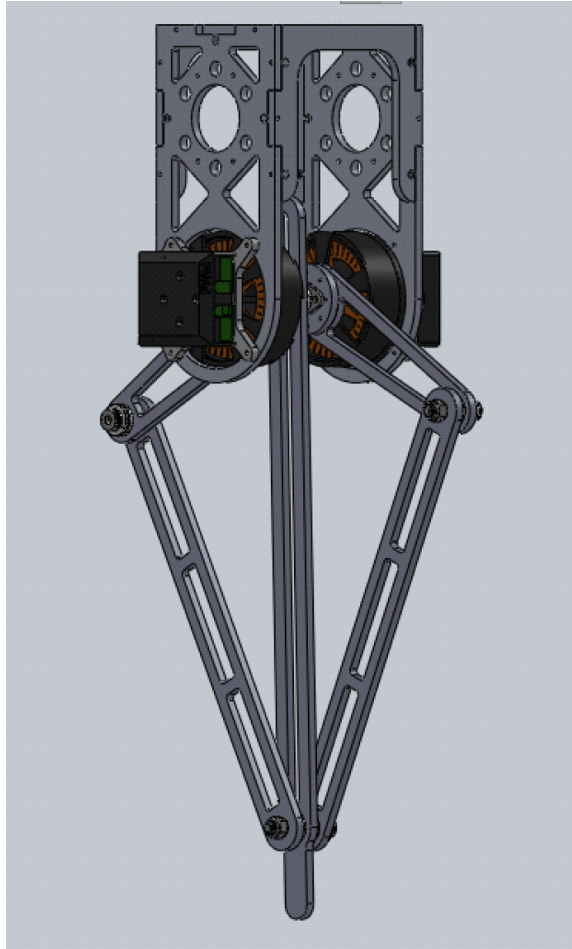
Figure 3.10: Future design of the field-deployable probe. Center bar would allow for probe tip to stay on the axis of radius of the motors controlling the probe motion. This design is capable of performing the test described here with the added flexibility of constant displacement tests and constant force tests.

CHAPTER 4 : The imprint of vegetation on desert dune dynamics

Abstract:

In this study we demonstrate the imprint of vegetation on the dynamics of parabolic dunes, which form when migrating barchan dunes become colonized by plants and invert their shape. We use topographic data to isolate translation and deformation of dune patterns, upwind of and across a sharp gradient of vegetation, at White Sands dune field, New Mexico. Barchan dunes are unstable due to an aerodynamic surface-wave instability. The dynamics of vegetated parabolic dunes are different; deformation becomes localized, and random, once plant density reaches a critical value associated with the barchan-parabolic transition. Plants stabilize dunes not only by slowing them down, but also by killing the fundamental mechanism that generates new sand waves and destabilizes dunes. Increasing plant density downwind increases vegetation-induced form drag and results in decreasing dune migration rate. Biological modulation of pattern-forming instabilities may also occur in other landscapes.

4.1. Introduction

Dunes in primarily unidirectional wind regimes act as downstream propagating waves of sand, but they are fundamentally unstable. Elevation perturbations along the crests of transverse dunes cause them to become sinuous, and eventually break up into barchans in sand-starved environments (*Parteli et al.*, 2011). Aerodynamic perturbations generate new surface waves on the backs of dunes at a wavelength λ of order 10s of meters (*Elbelrhiti et al.*, 2005; *Ping et al.*, 2014), causing barchans to emit smaller dunes from their horns. This phenomena counteracts collision-driven dune growth and leads to barchan fields that are stable in aggregate, even though individual dunes are unstable (*Elbelrhiti et al.*, 2005). Vegetation acts to slow dune migration, through three mechanisms: (i) reducing boundary shear stress τ_b due to form drag (*Durán and Herrmann*, 2006b; *Lancaster and Baas*, 1998); (ii) binding and consolidation of sand by roots (*Waldron*, 1977); and (iii) facilitating the formation of sand-stabilizing soil crusts (Fig. 4.1). In order for plants to gain a foothold, however, their growth rate must outpace the rate of burial by sand on the lee faces of dunes (*Durán and Herrmann*, 2006b; *Reitz et al.*, 2010; *Jerolmack et al.*, 2012; *Barchyn and Hugenholtz*, 2015) (Fig. 4.1). This growth occurs at a threshold dune migration rate, below which the stabilizing effects of plants result in a positive feedback that further slows dune migration (*Durán and Herrmann*, 2006b; *Baas and Nield*, 2007; *Pelletier et al.*, 2009). Stabilization typically occurs first at the low elevation horns because, because they have smaller deposition rates than the center. This initial pinning of the dune horns, while the rest of the dune continues to migrate, results in barchans inverting their shape to a parabolic form(*Durán and Herrmann*, 2006b; *Reitz et al.*, 2010) (Fig. 4.1).

The current understanding of how vegetation stabilizes dunes is essentially a kinematic picture; plants decrease erosion rate and ultimately pin the substrate in place (*Corenblit et al.*, 2011). Here we posit that plants disrupt the fundamental dune-forming instability by perturbing the sand flux (q_s) field — effectively shutting down the formation of surface waves, and the emission of smaller dunes from the horns of barchans. To test this idea

we examined dune dynamics at the White Sands National Monument (New Mexico, USA), a well-studied unidirectional gypsum dune field (*Reitz et al.*, 2010; *Jerolmack et al.*, 2012; *Langford*, 2003; *Kocurek et al.*, 2007; *Kocurek and Ewing*, 2005) that arises abruptly from a line source of sediment (downwind distance, $x = 0$). While not exact, a unidirectional approximation for both the dune migration direction and wind direction is reasonable. Wind speeds above threshold are strongly unimodal (from the Southwest) and the majority of dune migration occurs along these SW winds(*Pedersen et al.*, 2015; *Jerolmack et al.*, 2012). Previous research has identified three regions associated with differing sediment transport and dune dynamics (Fig. 4.2). Region *I* lies between the sediment source and $x \approx 2km$, where initially-transverse dunes break up into barchans and migration rate drops rapidly due to a topographically-induced downwind decline in τ_b (*Jerolmack et al.*, 2012; *Pelletier*, 2015). Downwind in Region *II*, τ_b approaches a stable value and there is a ~5 km long section where barchan dunes increase their spacing, but otherwise maintain a consistent size and migration rate (*Ewing and Kocurek*, 2010; *Baitis et al.*, 2014). Beginning around the location $x \approx 7km$, the barchans rapidly become colonized by vegetation and invert their shape — over a scale of 1 km — to a parabolic morphology (*Durán and Herrmann*, 2006b; *Reitz et al.*, 2010; *Jerolmack et al.*, 2012; *Barchyn and Hugenholtz*, 2015) (Fig. 4.1). Region *III* is associated with parabolic dunes that become increasingly vegetated, elongated, and slower moving as they progress downwind (*Jerolmack et al.*, 2012; *Pelletier*, 2015).

4.2. Results and Discussion

We make use of repeat aerial LIDAR topographic data (DOIs: 10.5069/G9ZK5DMD; 10.5069/ G97D2S2D) collected in September 2009 and June 2010, to construct digital elevation models (DEMs) with horizontal and vertical resolutions of 1 m and 0.1 m, respectively (see Methods). The dunes at White Sands have characteristic lengths of ~100 m, heights of several meters, and migration rates of several meters per year, so structure and dynamics are well resolved with this data set (*Pelletier*, 2015; *Barchyn and Hugenholtz*, 2015; *Xia and Dong*, 2016). We assume that the rates of dune migration for the 2009-2010 windy season

are typical of the migration that would occur in any other given year. In addition, we use high-resolution ($\sim$0.3 m/px) aerial photography from 2004, that is capable of resolving individual plants to quantify the spatial distribution of vegetation across the study area (Fig. 4.1). An implicit assumption is that the vegetation remained in a quasi-steady-state over the course of six years between images and topography data. Because we interpret vegetation density averaged over the width of the dune field in this study — and not at the scale of individual plants or dunes — we consider this a reasonable assumption; if the vegetated boundary migrated at the rate of individual dunes, this migration would result in a maximum offset of 20 m relative to the 2004 location. Anecdotally, vegetation communities have not changed notably over our ten years of field work in the dune field. The novelty of our approach is that we examine dune deformation — changes in both the profile and planform shape that are independent of net translation — to probe the dynamics of dune-pattern transitions and the influence of vegetation (Fig. 4.2). Profile deformation is quantified in the downwind (x) direction using a technique first developed for subaqueous bed forms (*McElroy and Mohrig*, 2009). Dunes are separated from the substrate, and the phase lag associated with maximizing correlation is used to determine a dune's migration rate V_c from the two DEMs; the residual elevation differences, $\prod$ [m/yr], represent deformation at each point on the dune. $\prod$ is defined as:

$$\prod = \frac{\eta\left(x + V_c, t_2\right) - \eta\left(x, t_1\right)}{\Delta t}, \tag{4.1}$$

where η is elevation and t indicates profiles separated by time Δt. We use the magnitude of $\prod$ throughout the paper instead of the rate itself. A different technique, though similar in spirit, is used to quantify deformation in the planform shape of dunes. A cloud of points that represent the footprint of a dune are tracked between the two surveys. The residual differences in the positions of these points, after subtracting V_c, are used to compute a quantity called D^2_{min} (units of m^2) and a measure of homogeneous strain we call D_{aff} (units of m^2) (Fig. 4.2; see Supporting Information). These metrics are commonly employed to

65

study the deformation of granular materials (*Utter and Behringer*, 2008). D^2_{min} quantifies the amount of non-affine deformation that a body under shear has undergone and is defined as:

$$D^2_{\min}(t, \delta t, r_c) = \sum_{i=1,...,N(r_c)} \left\| r'_i - r'^A_i \right\|^2 \tag{4.2}$$

where $N(r_c)$ is the number of dune sample points belonging to a cluster centered in r_c, r'_i is the current point being sampled and r'^A_i is the location that r'_i would be in if all deformation occurred along the affine deformation matrix A (see Supporting Information for further explanation). D_{aff} is computed from A in the course of finding D^2_{min}. We first examine qualitative patterns in the maps of profile-deformation ($|\prod|$) and planform deformation (D^2_{min}), in the context of the dune-pattern transitions (transverse to barchan, and barchan to parabolic) at White Sands. The most striking result is the presence of laterally-coherent stripes of large deformation rate in dune profiles, approximately 15-20 m in wavelength, which are pervasive on transverse and barchan dunes but nearly absent on parabolic dunes (Figs. 4.3; 4.14). Spectral analysis of the ($|\prod|$) map confirms the presence of a characteristic wavelength (15.1 m) for deformation on unvegetated dunes (see Fig. 4.14) that is consistent with the surface-wave instability proposed by Elbelrhiti (*Elbelrhiti et al.*, 2005). While field evidence for this instability has been documented in the structure of dune profiles (*Elbelrhiti et al.*, 2005; *Ping et al.*, 2014), it has not to our knowledge been observed from dune dynamics. In the parabolic region these stripes largely disappear; not only is deformation rate lower, but it is also visibly less coherent (Fig. 4.3). These findings provide a first confirmation that plants suppress the dune-forming instability. Turning to planform deformation, the most significant pattern is a zone of large D^2_{min} and D_{aff} in Region I compared to the rest of the dune field. Large values of planform deformation are associated with the initial upwind margin of the dune field, where proto-dunes are combining to form transverse dunes. This initial peak is followed by a consistent decline in D^2_{min} that follows the breakup of transverse dunes into barchans (see Fig. 4.4 panel

66

B). This behavior is consistent with the planform instability proposed by Parteli (*Parteli et al.*, 2011). There is also a second, more subtle change in D_{min}^2 and D_{aff} associated with changes in planform pattern across the barchan-parabolic transition. Taken together, data indicate that the transverse-barchan transition primarily involves planform deformation. We suggest that the dynamics of the barchan-parabolic transition can be described as an abrupt shutdown of the surface-wave instability and a gradual planform inversion, which are manifest as notable declines in profile deformation and modest increases in planform deformation.

To examine quantitative downwind trends in dune dynamics and vegetation, we compute width-averaged quantities of dune migration, affine deformation D_{aff}, and vegetation density ρ_{veg} which represents the area fraction of dunes that are covered in plants (Fig. 4.4). Here width-averaging refers to averaging in the cross wind direction. To ensure that the averaged trends rise above the error associated with our methods, we performed error analysis of quantities involved to confirm that associated error is second order or smaller (see Supporting Information for more detail). Dune migration data confirm previous findings that V_c declines rapidly in transverse Region *I*, is roughly constant in the barchan Region *II*, and then gradually decreases toward zero in the parabolic Region *III*. The latter spatial decrease in dune migration rate is roughly linear, and is mirrored by an approximately linear increase in vegetation density. The inverse correlation between V_c and ρ_{veg} also holds at the individual dune scale (Fig. 4.15). Because $V_c \propto q_s$, and $q_s \propto (\tau_b - \tau_c)$ where τ_c is the threshold entrainment stress (*Bagnold*, 2012; *Durán and Herrmann*, 2006a), the decline in dune migration rate is due to either a decrease in the boundary stress or an increase in the threshold entrainment stress (or both). In the unvegetated dunes of White Sands, it has been shown that the dominant winds produce a boundary stress approximately 1.6 times the threshold stress, i.e., $\tau_b/\tau_c \approx 1.6$ (*Jerolmack et al.*, 2011). Previous work has shown an inverse relation between vegetation density and boundary shear stress due to the form drag effect (*Durán and Herrmann*, 2006b):

$$\tau_b = \frac{\tau_0}{1 + m\beta\rho_{veg}/\sigma},\tag{4.3}$$

where τ_0 is the boundary stress in the absence of plants, $m = 0.16$ is a model parameter, β is the ratio of plant to surface drag coefficients, and σ is the ratio of basal to frontal area of a plant. Considering that plant density increases from $\rho_{veg} \approx 0$ to $\rho_{veg} \approx 0.02$ over the parabolic region, and utilizing parameter values found by Wyatt to be applicable to creosote desert shrubs ($\beta = 200$; $\sigma = 1.45$) (*Wyatt and Nickiing*, 1997), we would expect the excess boundary shear stress ($\tau_b - \tau_c$) to decrease by roughly a factor of five. This decrease is consistent with the magnitude and the trend of decreasing V_c, suggesting that vegetation-induced form drag may exert the greatest influence on declining migration rates of parabolic dunes.

In order to quantify coherent deformation patterns (Fig. 4.3) and relate them to plant density, we compute a "coherent deformation density" ρ_{CD}. We perform blob detection on the $|\prod|$ map of the entire study area, compute the ratio of blob to dune area for each dune in the dataset, and then perform width averaging to obtain a downwind profile of ρ_{CD} (see Methods). This quantity detects spatial coherence of dune profile deformation, even when magnitudes are low. There are two major features in the profile of ρ_{CD}: first, coherent deformation is highest at the upwind margin and gradually decreases downwind to the end of the barchan Region *II*; and second, there is a marked drop in coherent deformation at the barchan-parabolic transition, that corresponds to the location where vegetation density begins to increase. This drop provides quantitative support for the qualitatively distinct behaviors observed up- and down-wind of the barchan-parabolic transition (Fig. 4.3). The onset of vegetation in the parabolic region leads to a rapid loss of coherent deformation.

4.3. Conclusion

The current work has used the lens of deformation to examine two dune-pattern transitions at White Sands that are common in desert environments. This new approach demonstrates

that a proposed planform instability (*Parteli et al.*, 2011) is responsible for the breakup of transverse dunes into barchans. After this breakup, migration and deformation data indicate that the barchans evolve to a state of pattern stability that is maintained by the aerodynamic surface-wave instability, as proposed by Elbelrhiti (*Elbelrhiti et al.*, 2005). This instability is detected as coherent stripes of profile deformation, that are completely disrupted with the onset of vegetation. In the parabolic region, deformation becomes smaller in magnitude and more localized, while migration rate gradually slows due to the increase in plant density and its associated form drag. While it is well known that increasing plant density results in decreasing erosion (*Pelletier et al.*, 2009), the vegetation gradient at White Sands provides an unusually clear and quantitative demonstration of this effect. More fundamentally, this work shows how plants can drive a qualitative shift in the form and dynamics of a landscape pattern, by modulating an abiotic pattern-forming instability. A related example is the vegetation-induced transition from braided to single-thread river channels; by slowing the rate of bank erosion, plants prevent the formation of mid-channel bars (*Tal and Paola*, 2007; *Braudrick et al.*, 2009; *Gran and Paola*, 2001). There are few studies that have identified distinctive and quantifiable effects of life on the landscape (*Dietrich and Perron*, 2006; *Reinhardt et al.*, 2010; *Corenblit et al.*, 2011), and this study may provide guidance for that search.

4.4. Methods

Digital elevation models (DEMs) of the study area outlined in Fig. 4.1 were collected by the National Center for Airborne Laser Mapping (NCALM) (DOIs: 10.5069/G9ZK5DMD; 10.5069/G97D2S2D) in September, 2009 and June, 2010. For each DEM, 2D elevation profiles were sampled along the width of the study area along the time-averaged wind direction. For each elevation profile, individual dune profiles were identified for both DEMs. A unique V_c for each dune profile was then obtained by finding the spatial lag that maximized correlation between the sample years. The V_c for every dune profile in the study area was then subtracted from the June, 2010 DEM. This variably shifted DEM was then compared to

the 2009 data to obtain the values used to quantify both vertical and planform deformation: D_{aff}, $\prod$, and ρ_{cd}. The vegetation data used to calculate ρ_{veg} was produced from circa-2004 high-resolution aerial photography that covers the same area as the DEMs. For more information on methodology see Supporting Information.

4.5. Supporting Information

4.5.1. DEM preparation

Digital elevation models (DEMs) for September, 2009 and June, 2010 were prepared from LIDAR point cloud data downloaded from www.opentopography.org (DOIs: 10.5069/G9ZK5DMD; 10.5069/ G97D2S2D). These points clouds average 5.63 pts/m^2 and 4.62 pts/m^2 respectively. DEMs with a resolution of 1 m^2 per pixel were prepared using a protocol almost identical to that used by Pelletier [*Pelletier*, 2015]. The protocol involved downloading all available .LAZ files from the LIDAR surveys associated with the dune field for both years. For each year, the LAStools software suite was then used to stitch these files together into a contiguous point cloud. The software points2grid (available from www.opentopography.org) was used to create a .LAS formatted DEM from the lowest elevation return in every square meter. This DEM was then opened in GRASS GIS where the subset of the dune field DEM used in the study was selected and exported to .MAT format. Inside Matlab®, the 2009 DEM was shifted vertically by 0.34 meters so that both DEMs had the same mean elevation. For both the 2009 and 2010 DEMs, there were 5-10 anomalously low returns (<0.001 % of the dataset). These elevations were deleted and replaced with an average of the immediately surrounding elevations. The DEM matrices were then rotated by 25 degrees clockwise so that the horizontal axis of each matrix represented the predominate migration direction of the dune. As noted above, the area used in this study was a subset of the total DEMs available for both years obtained. The area was selected so that, for a given line drawn perpendicular to the dominant wind direction, any point sampled along this line would be roughly the same distance away from the upwind margin. This criteria was viewed as important to ensure consistency in the width-averaged trends displayed in

Fig. 4. The criteria restricted our analysis to an area of 1.2 km (transverse/across-wind direction) by 12.0 km (downwind direction).

4.5.2. Detecting Individual Dune Profiles

Once DEMs for both years were obtained and processed, elevation transects of the study area were sampled for every 1 m wide row in the DEM matrix along the predominant wind direction. A subset of one of these transects can be seen in Fig. 4.5. A modified peak detection algorithm was then used to estimate the start of the stoss side, the crest height, and the end of the lee side of the dune profiles found in each transect. More details about the original algorithm can be found in *Yoder* [2016]. This peakfinding algorithm was used to detect approximate dune peaks. Starting from this peak, a local, iterative search was performed both downwind and upwind of the peaks to determine the start and stop locations of the dune profile. This search assembles all of the local minimums below a threshold elevation in between the current peak, the downwind peak, and the upwind peak. This threshold was determined by adding a constant value to the global minimum between the current profile peaks and the neighboring peaks. A maximum elevation threshold ensured that only local minimums in the interdune or near-interdune were considered. The local minimum that was closest to the current profile peak on the downwind side was identified as the beginning of the stoss side. The local minimum closest to the peak on the upwind side was identified as the lee side. Once the stoss start and lee stop locations are determined, profile averaged quantities such as V_c are assigned to the middle of the profile's width.

A typical result of this procedure is demarcated for a number of dunes in Fig. 4.5. Error is associated with the method, though, in the majority of cases, the algorithm adequately demarcates each dune profile from its neighbors and separates dune profiles from: (1) shallow slope, interdune regions, and (2) masses of sand that are not tall enough to properly be called a dune. Individual dune profiles from the June, 2010 DEM are shifted back onto the 2009 data using the technique described in the next section. The performance of the method in both successfully evaluating dune profiles and the beginning of the profile stoss

71

side and end of the lee side is described below.

In assessing the accuracy of the dune profile detection algorithm, we were mainly concerned with the rate of successful identification of profiles and how well stoss and lee locations were detected. The performance of peak identification was largely ancillary as peaks are only used in the paper to obtain a starting point along the dune to search for the stoss and lee locations. We classified profile identification errors into three different types - unidentified profiles, lumped profiles, and split profiles. Occasionally a peak was not detected and this resulted in a dune profile not being included in the analysis. Unidentification of some small dune profiles was a necessary consequence of having to choose a threshold over which a local peak in the elevation data was considered the peak of a dune. At a minimum, the threshold should be over a meter due to the presence of large features in some interdune areas that were not actually associated with a dune. The choice of this threshold was further influenced by the bipartite and tripartite peak structure of individual dune profiles; if the threshold was set too low, than a single dune profile was identified as several profiles. In this work a threshold of two meters was used. Table 4.1 shows the number of unidentified small dune profiles for 10 randomly selected elevation transects from the study area. For each of these transects, the automatically detected dunes were compared to dunes classified by eye. On average less than 10 percent of dunes were not detected. Because dune profile width scales with dune height this Unidentification represented a much smaller fraction of total dune surface along a transect than one would initially assume. An average dune width for all dunes in a profile was on the order of 100 meters, while profile widths for dune profiles with 1-2 meter peaks were typically 30-50 meters. These widths implied that the percentage of unidentified dunes in a profile actually made up 2-4 percent of the total dune surface along a given elevation profile. A lumped profile resulted when two dune profiles were identified as one. This occurrence was uncommon and usually occurred when there was almost no interdune in between successive profiles. A split dune occurred when a single dune was classified as two or more dunes. This over-identification happened because of the multi-peak structure of some profiles. The prevalence of both split and lumped dunes for

72

the manually classified transects can be seen in table 4.1.

The other type of error associated with the profile detection involves assignment errors at the start of the stoss side and the end of the lee side. Due to the gradual transition from interdune to dune at the stoss side, the determination of the beginning of the stoss side of the dune was subject to a certain degree of subjectivity. This was true even in the field. Our approach created an objective measure to determine when the stoss side begins and this led to certain instances where an observer would disagree with the results of the method. Stoss side start identification was further complicated by the wide variety of curvatures represented by the transition from the interdune area to the stoss surface of the dune. The lee side was characterized by a dramatic change in curvature for most profiles and so was arguably less prone to identification errors. To characterize the error range present in both the stoss start and lee stop locations, we compared the performance of the automated profile detection method to a visual assessment of the profile start and stop locations. Fig. 4.6 shows a histogram of the difference in meters between the start and stop locations between the two approaches. The analysis was performed for 100 dunes selected at random. Relative to manual profile detection, the automated method both over-identified and under-identified both the stoss start and lee stop locations. To assess how large this error was relative to the total dune profile, we compared the total amount of stoss start and lee stop discrepancy as a fraction of dune width. Fig. 4.7 shows a histogram of identification errors as a percent of total dune width for the 100 dunes we compared. Most identified dune profiles had identification errors of less than 10 percent with over-identification being more prevalent. While both dune identification and profile start/stop errors were large enough to introduce artifacts into the data, we were still able to use the profile information to make the other measurements presented in the paper. When relevant, the effects of these errors on other measurements will be discussed in the proceeding sections.

4.5.3. Estimating Dune Profile Migration Rates

Once dune profiles were identified, then each individual profile from 2010 was shifted backwards by N meters. N was the shift that maximized the cross-correlation between the dune's 2010 elevation profile and a segment of elevation from the analogous 2009 profile that was of the same length as the 2010 profile. For example, if a dune migrated forward 4 meters during the study period, then the initial correlation was between the the 2010 dune profile and part of the 2009 profile plus 4 data points of either interdune area or a neighboring dune. As the 2010 dune profile was shifted continuously backwards by N steps, the correlation between the two profiles reached a maximum where the shapes overlap without including data from interdune areas or other dunes. For most dunes, the maximum correlation values were high (0.8 was typical), but not 1 because the dunes deformed as they migrated along. The end result of this technique is illustrated in the bottom of Fig. 2. This method assumed that dunes move forward or remain stationary. The method also assumed that a dune did not migrate more than its entire length during the study period. An additional limitation of this method was that calculated displacements were only accurate to the pixel width used in the study (1 m).

Once the value N was found that maximized the cross-correlation, it was recorded as V_c, or the migration rate for that dune profile. The operation of maximizing the cross correlation has been shown to be the equivalent operation of finding the displacement in the case of the simple translation by *Bergonnier et al.* [2005]. The operation we performed was exactly analogous to this method for the 1D case with the exception that vertical deformation affected the correlation. For most of the 1 m sample points along the dune profiles, this deformation was not coherent. Furthermore, noise arising from deformation was high wavelength with the longer wavelength features still being preserved without appreciable change. The performance of this method for determining profile displacement was verified by eye for 50 dunes randomly selected throughout the dune field and found to be accurate to 1 m resolution.

To analyze errors arising from discretizing displacements to an accuracy with 1 m, a displacement error was defined v that represented the difference between the dune displacement calculated to an accuracy of 1 m and the actual dune position. v had a range of -.5-.5 m with a peak magnitude occurring halfway between each successive one meter increment. The shape of v was a sawtooth function and can be visualized in Fig. 4.8. After assuming equal likelihood for all values of v, it was possible to estimate how discretizing would effect the across-wind averaged (width averaged) trend presented in Fig. 4 panel A. In practice, a moving window was used to average all the V_c measurements assigned to all the dune profiles located within a 1241 x 50 m moving area. Because the density of observed dune profiles varied throughout the dune field, the number of values within the averaging window also changed. The density of observations was usually somewhere between 500-1500. The effect of averaging on the error of the final V_c trend can be seen in Fig. 4.9. It was seen that, if one assumed that discretization errors occurred uniformly within a range of v from -.5 and .5, then sampling from this range and taking the mean of this sample produced an average error centered around 0 m with the majority of errors occurring within .015 m. Errors taken evenly from a uniform distribution centered around zero had a tendency to cancel out and produced an average total error clustered around zero.

The effect of dune classification errors on V_c was primarily seen in the unidentified dunes. In the case of split and lumped dunes, the dune was still assigned a value for V_c and was shifted. The effect of unidentified dunes on the width averaged V_c measurement was minimal. If one assumed that unidentified dunes were uniformly distributed through an elevation transect and a representative number of unidentified dunes was taken to be 6 with a width of 50 m on average. For a given width (across-wind) averaged profile in the along-wind direction, the probability of not including a V_c measurement was 2.5 %. The probability of missing two or more measurements in the averaging area was .06 % and so on.

The effect of stoss start and lee stop errors on V_c was negligible in the case of over-identification of a dune profile. This was because the noisy, low signal interdune elevations

did not a have a strong effect on which dune displacement displayed the maximum correlation coefficient. To assess the effect of under-identification errors, 50 dunes were selected at random and the efficacy of the V_c shift was assessed by eye. The portion of the under-identified dune profile that was classified as a dune appeared to be shifted as well as other dunes. This appeared to be because, even in the extreme cases of maximal error, over 80 % of the dune form remained to be correlated.

The end result of the dune migration analysis was a map of V_c values for each individual dune profile that was used to create a variably shifted version of the 2010 DEM where each profile was shifted by its unique V_c. The creation of this shifted DEM was crucial because it allowed us to analyze the deformation of dunes across the entire study area using the techniques described below.

4.5.4. Quantifying Vertical Deformation

McElroy and Mohrig [*McElroy and Mohrig*, 2009] defined a useful metric of vertical dune deformation, which formed the basis for the technique we employed here. A deformation rate or $\prod$ was defined in the main text in Eq. 1. Eq. 1 can be thought of as the net aggradation and/or degradation that occurred at a point on the bed over the sampling duration in the Lagrangian reference frame, or the reference frame that was arrived at when the distance each dune profile travels over the study period was removed. This removal resulted in a shifting of each dune profile back onto its previous years position. The variable x is the along-wind location of the dune profile, η is elevation, and t indicates profiles separated by time. Because it is computed in the reference frame of the migrating dune, $\prod$ represents a local deformation rate for the time step in question.

The dune identification errors discussed above affected $\prod$. Local points on the $|\prod|$ map were not computed. The main effect was seen in unidentified dunes and in dunes that were under-identified. These errors were not prevalent enough to prevent the $|\prod|$ map from being used to explore patterns in the vertical deformation. Zones of coherent deformation were

still clearly visible in Fig. 3. It should also be noted that these types of error should have destroyed the signal of coherent deformation noted in the main text, instead of amplifying apparent coherence. Other errors that affected $\prod$ arose from the discretization error, v, described in the section discussing how V_c is obtained. Here, the magnitude of the error was dependent on slope. Sections of a profile that have a steeper slope showed apparently higher $\prod$ values when v was at its peak. Fig. 4.10 shows how artificially shifting 67 real dune profiles identified from the 2009 DEM at the sub-meter scale and then re-shifting the dune at the 1 m scale to obtain a V_c introduces error into $\prod$. Peak average errors are on the order of .08 m/9mo. In general, these errors introduced artifacts akin to uniform, white noise into the $\prod$ values calculated for the profiles. This noise was large enough to affect the floor of the values observed. However, the main analysis that $\prod$ was used for involves using $|\prod|$ to determine patterns of coherent deformation with average $|\prod|$ values of .83 m/9 mo. This was much higher than the observed noise floor. Our empirical estimate of the error in $\prod$ supports the idea that the noise introduced by discretization was not large enough to destroy the signal of coherent deformation.

Computing $\prod$ as defined above allowed access to the component of deformation associated with the vertical deformation of the free surface of the dune. However, there are other components of the deformation tensor that should be accessed to gain further insight into how the dune field at White Sands is evolving. Namely we would like to get some idea of the amount of planform deformation that was occurring in the dune field.

4.5.5. Quantifying Planform Deformation

To provide an estimate of the local amount of planar deformation we examined both the affine strain tensor, D_{aff}, and a metric, D^2_{min}, commonly used in granular physics. In this approach, the planform shape change of the dune body is thought to be analogous to a strain. This allowed us to separate the shape change into different components. One component, the affine strain, is the shape change associated with linear transformations of the dune outline (simple shear, extension, compression, etc). The other component, the

non-affine deformation, is represented by D_{min}^2. The non-affine deformation is the residual left over after using a best fit value for the local affine strain tensor (*Falk and Langer*, 1998). At any given time t we considered a small cluster of points sampled along a dune outline surrounding a given point on a dune with center position r_c and the displacement of these dunes within the time interval $[t; t' = t + \delta t]$.

We call r_i the relative position of point i in that cluster of points sampled along the dune at time t, while r_i' indicates the respective relative position of the point at time t'. The positions were sampled relative to the center of mass of the cluster at the corresponding time (*Utter and Behringer*, 2008).

If the overall mechanical deformation of the cluster is completely homogeneous between time t and t', then each dune sample point i has, at time t', a relative position given by a simple mathematical mapping (geometrical transformation) from its position at time t; i.e., $r_i'^A = E(t, \delta t, r_c) r_i$, where $E(t, \delta t, r_c) r_i$ is an affine transformation matrix for the cluster of dune sample points around the point at position r_c, at time t.

The estimation of $E(t, \delta t, r_c) r_i$, at each time t, and for each dune point with position r_c was obtained by formulating an optimization problem, consisting of minimizing the least squares error function. This takes the form:

$$D_{\min}^2(t, \delta t, r_c) = \sum_{i=1,\dots,N(r_c)} \left\| r_i' - r_i'^A \right\|^2 \tag{4.4}$$

where $N(r_c)$ is the number of dune sample points belonging to the cluster of dune sample points centered in r_c .

The minimization was done with respect to the elements of E. Its solution led to a best fit of the actual, local deformation with an affine transformation model and an estimate of the residual amount of non-affine deformation, given by the corresponding minimum value of D_{min}^2. The non-affine deformation metric represented the departure from a homogeneous

affine deformation field and was a measure of the plastic, irreversible component of planform deformation in the dune field at that point (*Utter and Behringer*, 2008). In this analysis D_{aff} is a strain tensor that can be separated into components of shear, rotation, etc. while D_{min}^2 is a deformation tensor. Similarly to its effects on $\prod$, the dune identification errors and effect of discretization were sources of noise that do not prevent us from examining first order trends in the patterns of planform deformation.

The map of of both D_{aff} and D_{min}^2 can be seen in Fig. 4.11. Both D_{aff} and D_{min}^2 track each other well with concomitant increases and decreases in each quantity. D_{aff} was also width (cross-wind) averaged along the dune field and this result is presented along with the other width averaged trends in Fig. 4.

4.5.6. Measuring Coherent Deformation

Visual inspection of the $|\prod|$ maps showed frequent patches of coherent deformation in the transverse and barchan portion of the dune field thought to be associated with the instability reported by Elbelrhiti et al(*Elbelrhiti et al.*, 2005). To provide some measure of the frequency of this coherent deformation in different parts of the dune field, we computed the coherent deformation density, ρ_{CD}. To detect coherent blobs of deformation, we used a wavelet based image segmentation method described in *Sengar et al.* (2016). This method was chosen over more commonly used methods because of its performance in dealing with extracting areas of deformation above a threshold value and size above the noisy, in-homogeneous background deformation of the rest of the dune field. For further information on the performance of the method on images of similar noise level to that obtained from the deformation map the reader is referred to *Sengar et al.* (2016).

Once the blobs of deformation above a certain intensity were reliably identified, ρ_{CD} was computed throughout the dune field as $\rho_{CD} = A_{CD}/A_D$. Here A_D is the total dune area that is currently being considered and A_{CD} is the portion of this area that is coherently deforming. ρ_{CD} was then width averaged to give the downwind trend for ρ_{CD} seen in Fig.

4C.

4.5.7. Calculating Vegetation Density

Vegetation density (ρ_{veg}) was calculated using a high resolution, georeferenced, aerial survey of the dune field that was performed in 2004 by the National Park Service. This survey had a resolution of 1 ft per pixel and was performed on a clear day with even illumination conditions. The quality of the aerial images allowed for an automated estimation of the fraction plant cover for a given area dune. To do this, first a threshold was applied to the images. Pixels below a certain grey level were considered to be too dark to be sand. Then Matlab®'s built in image segmentation command was run on the images to connect the darker pixels into blobs. Most of the interdune areas showed up as extremely large blobs and these were removed since we were only concerned with the dune surface. The smaller blobs were then considered to be potential vegetation on the dune surface. A primary challenge of this method was that, in the aerial images, the distinction between the beginning of the stoss side of a dune surface and the end of an interdune were challenging to discern and had a degree of subjectivity. To determine if a patch that was identified as potential vegetation by the thresholding algorithm was on a dune, we looked at the grey level of the pixels around the perimeter of an identified blob. If the average grey level of the perimeter was above a threshold lightness then the patch was interpreted as being on a dune surface. Another challenge was that small patches of vegetation and certain plant types can have the same grey levels as the dune surface itself. These small, sparse patches of vegetation were interpreted as being associated with smaller, less dense stands such as patches of small grass. These smaller, shorter plants were assumed to have less influence on transport processes. Thus, to avoid over-classification of plants relative to dune surfaces, the threshold chosen to classify plant pixels from sand was set higher than the darkest values associated with unvegetated sand surface. This led to a strong cutoff in the detected plant stands with plant stands below a certain density and size not being detected. This should not change the qualitative results of the paper concerning the trends

in the vegetation. This is especially true if one accepts that the highest density plant stands (i.e. the darkest, largest stands) will be the most likely to affect the migration flux through the form drag mechanism proposed in this work. Future studies will need to impose a less stringent threshold on the vegetation and algorithms that can detect more subtle patches of vegetation will need to be devised if the relationship between fraction plant cover and dune morphodynamics is to be quantified beyond associating trends in the relative amount of fraction plant cover throughout the dune field to the migration rate.

The results of the method described above can be seen in Fig. 4.12. As discussed above, it was observed that there was significant overlap in the grey levels associated with very sparse vegetation and the completely unvegetated dune surface. Because of this, it was decided that the threshold for classifying a pixel as a plant would be set to avoid this overlap. To quantify this threshold, 10 square regions of approx. 45 m by 45 m were randomly selected from portions of the dune field with vegetation. The distribution of grey levels of unvegetated portions of these regions was then calculated. This result can be seen in Fig. 4.13. The left hand tail of this distribution was then used as the threshold below which pixels would be classified as plants in our automated method. That there is slight overlap between the grey levels classified as vegetation in the automated method and grey levels classified as dune surfaces arises from the fact that identified plant areas underwent a dilation operation in the code before being included in the data-set as a vegetated area. The results of the automated vegetation classification scheme were also compared to the distribution of grey levels that results when vegetation is classified by eye in the 10 randomly selected regions. The intensity distribution of the eye classified vegetation pixels can be seen in Fig. 4.13 in red. It is apparent that the eye tends to select regions on the dunes whose grey levels significantly overlap with grey levels of unvegetated surface. The automated classification scheme avoids this ambiguity while capturing the darker grey levels that are also classified as belonging to vegetated patches in the visual inspection method.

Once pixels on dune surfaces were classified as either vegetation or non-vegetation, ρ_{veg} was

calculated in a similar manner to ρ_{CD}. ρ_{veg} is given by $\rho_{veg} = A_{veg}/A_D$. Here A_D is the total dune area that is currently being considered and A_{veg} is the portion of this area that is vegetated. Please see the included script for more details on the vegetation detection scheme.

4.5.8. Radially Averaged Power Spectral Density Analysis

To ensure that the wavelength of the coherent deformation structures we observed in Fig. 3 was of a similar length-scale to the wavelengths observed by *Elbelrhiti et al.* (2005), we performed a radially averaged power spectral density analysis in a region of the unvegetated dunes and a region of the vegetated dunes. While the 1D radially averaged result does not give an exact wavelength because of the anisotropy of the coherent deformation structures, it does provide an additional check that what we observed was consistent with a dune forming instability.

The procedure used to obtain the power spectral density plots inset in Fig. 4.14 was as follows. To remove long wavelength, coherent noise a pre-whitening scheme similar to that outlined in *Hyvärinen and Oja* (2000) was employed on the deformation maps. Pre-whitening effectively acted as a high-pass filter on the deformation maps by making all the individual elements in the map uncorrelated to one another. A 2D, discrete fast Fourier transform was then performed on the whitened map. This 2D fft map was then area normalized and converted to a 2D PSD map. A radial averaging scheme was employed on the 2D PSD map to produce the 1D PSD trend that shows the direction-independent mean spectrum for a given wavelength. This entailed selecting a frequency in the 2D PSD map and averaging it in all directions to obtain an idea of the mean intensity at that frequency (*Ruzanski*, 2011). This analysis was done at the dune scale to highlight the presence of sub-dune scale coherent deformation structures in the barchan dunes and their marked absence in the parabolic dunes (see the peak at the 15 m wavelength in the 1D PSD plot for the barchan dune in Fig. 4.14).
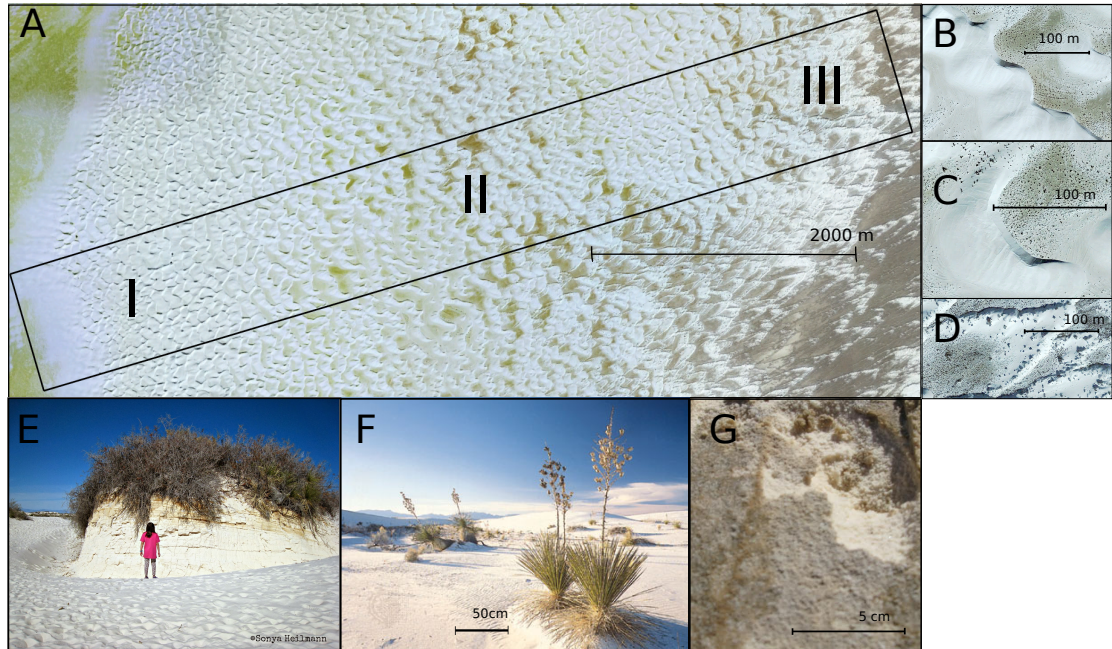
Figure 4.1: Landscape patterns at White Sands National Monument. (A) Aerial photograph of the dune field; black rectangle marks the region of this study. The three zones of distinct dune dynamics and morphology described in the text are indicated as regions I, II, III in the figure. (B)-(D) Representative barchan, transverse, and parabolic dunes, respectively. Varied effects of vegetation across scales include (E) stabilization of soil through roots, (F) sediment deposition due to to wake effects, and (G) growth of surface crusts.
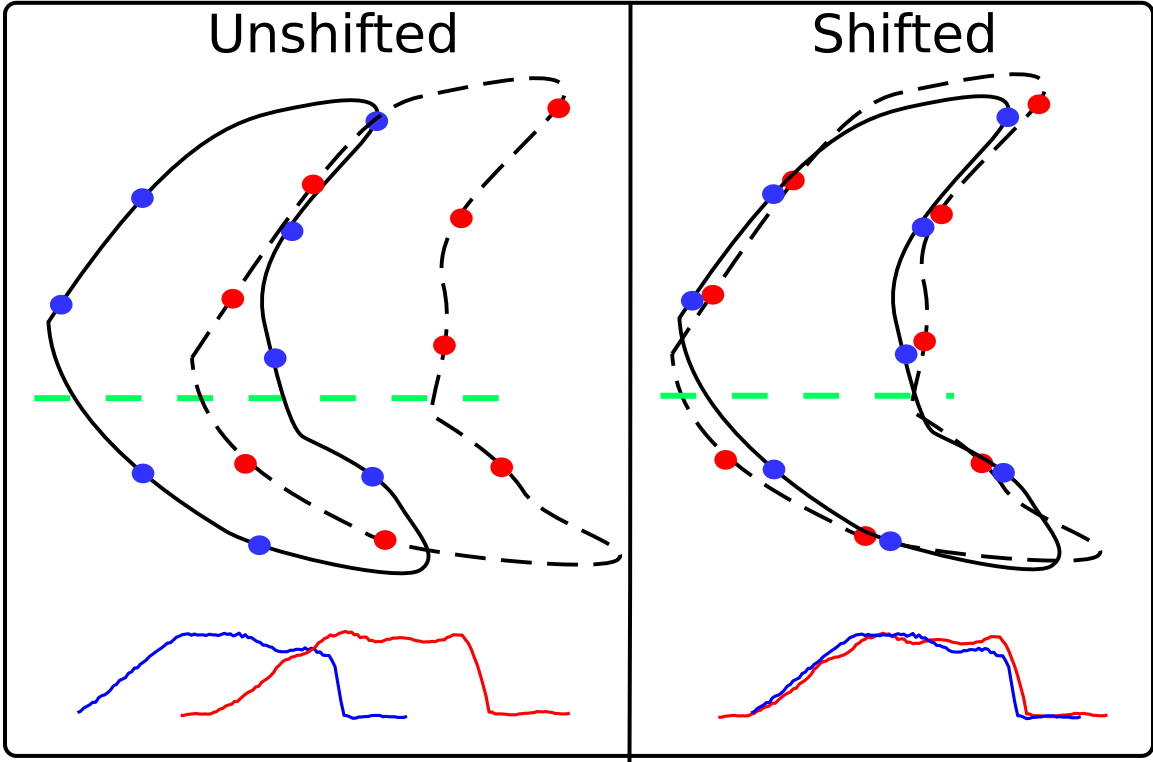
Figure 4.2: Definition sketch of deformation variables. Left "unshifted" shows a dune planform outline sampled at two different years (year one is blue and year two is red for entire figure), and below it is the elevation profile of the dune sampled along the green dashed transect. Right "shifted" shows the outlines and profiles shifted between years 1 and 2 by the net dune migration rate, V_c. Vertical deformation is then measured profile by profile along the dune using $\prod$. Planform deformation is computed using the metric $\mathbf{D_{aff}}$ and $\mathbf{D^2_{min}}$. For details of how deformation quantities are calculated see main text and Supporting Information.
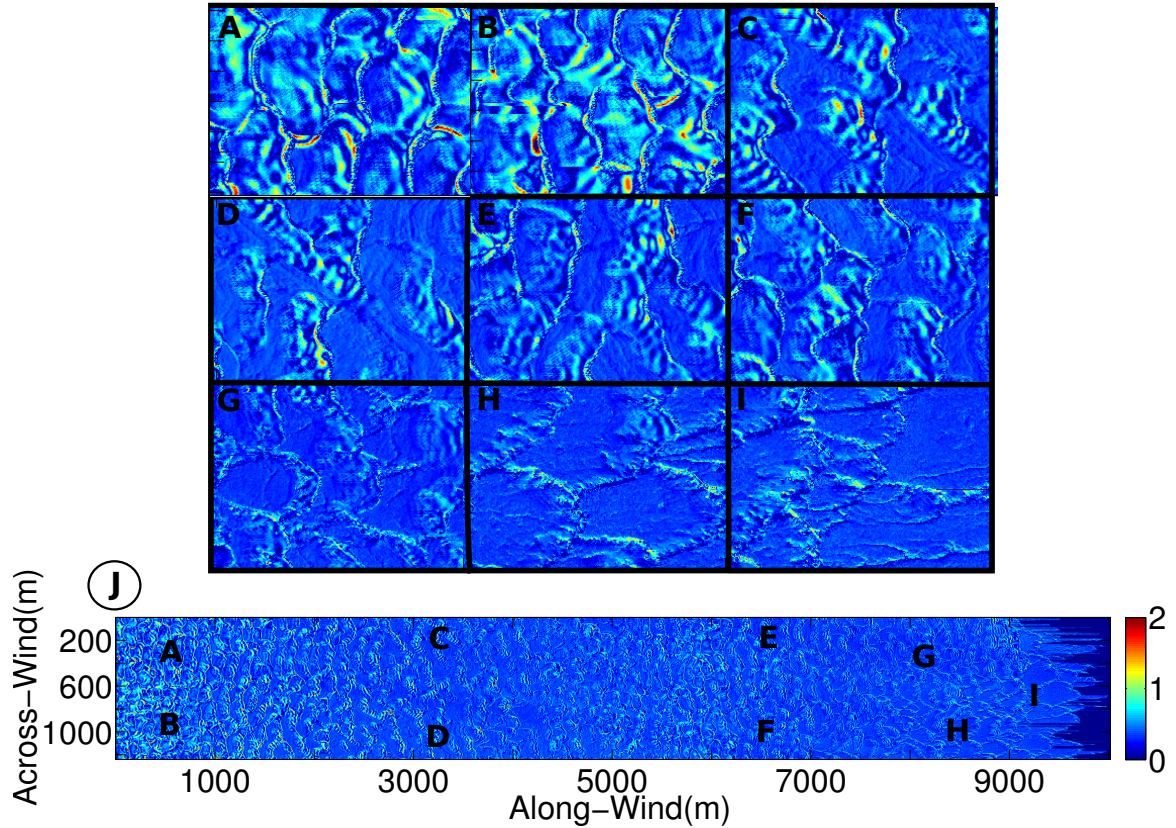
Figure 4.3: Nine regions roughly 100 m by 150 m in area showing patterns of vertical deformation, $|\prod|$, across the dune field. (A-F) laterally-coherent vertical deformation structures are seen on unvegetated transverse and barchan dunes, by mapping $\prod$ for every square meter in the DEM. Though these deformation structures are most intense closest to the upwind margin (A-C) they are still markedly present in the unvegetated barchans (D-F). (G-I) Map of $|\prod|$ for representative parabolic regions of the dune field; the absence of coherent deformation in these panels is typical for vegetated dunes. The bottom panel, J, shows a map of $|\prod|$ for the whole study area. The spatial locations that the regions A-F were taken from is shown on the map. Transverse, barchan, and parabolic zones of dune field are demarcated by I, II, and III. The units of the color-map are in m/9mo and are consistent for both the study area $|\prod|$ map as well as the regions.

85
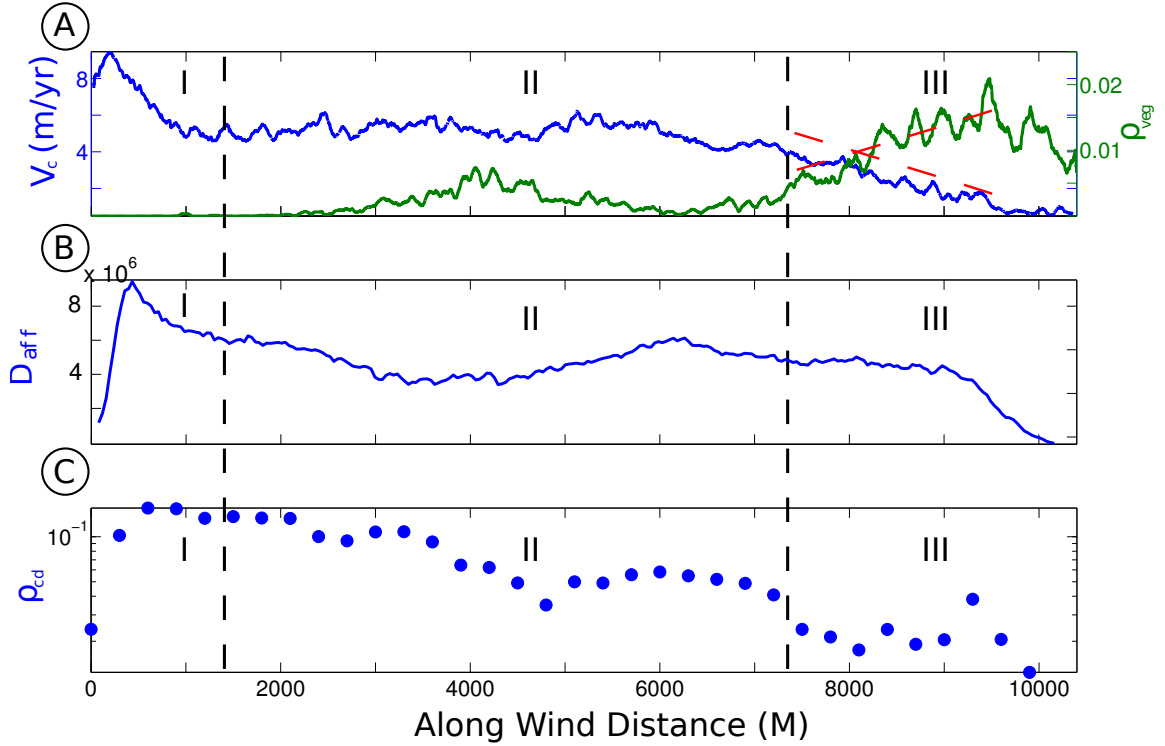
Figure 4.4: Downwind trends in dune kinematics and deformation; all quantities are averaged in the transverse (cross-wind) direction. (A) Dune migration rate V_c (blue) calculated from the 2009-2010 DEMs and vegetation density ρ_{veg} (green) calculated from 2004 aerial image; approximately linear decrease in V_c in the parabolic zone III corresponds to an approximately linear increase in ρ_{veg}, indicated by dashed red lines. V_c and ρ_{veg} are smoothed using a 40 m running average in the transverse direction. (B) Affine deformation D_{aff}, which generally tracks downwind changes in V_c with the exception of the zone II to III transition. D^2_{min} isn't shown because it generally follows D_{aff}. (C) Density of coherent deformation $\rho_{(c)}$, which also generally tracks changes in V_c and D but shows an abrupt drop across the barchan-parabolic transition (vertical dashed line) associated with the disappearance of the surface-wave instability. The transverse, barchan, and parabolic zones of the trends are demarcated by I, II, and III on the plots.
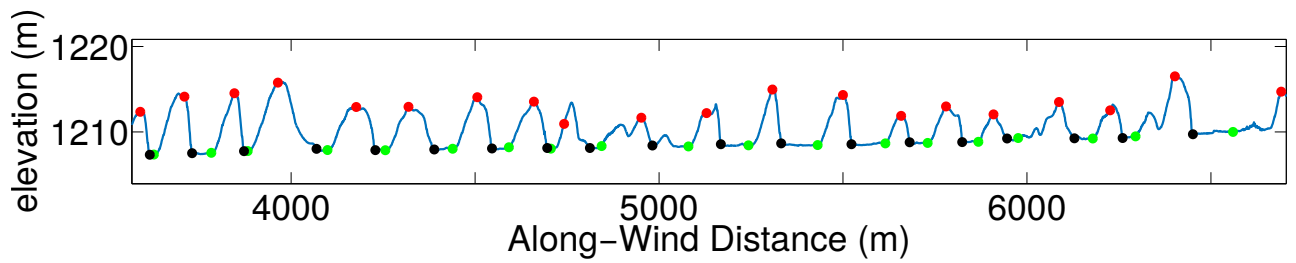
Figure 4.5: Illustration of the results of the dune profile detection algorithm. A ~2.5 km long segment of one 2D elevation profile is shown. Estimated crests of detected dunes are marked in red. The beginning of the stoss side of the dune is marked in green. The lee-side toe is marked in black. In between many profiles, flat interdune regions can be seen (demarcated as the spaces between successive black and green markers).
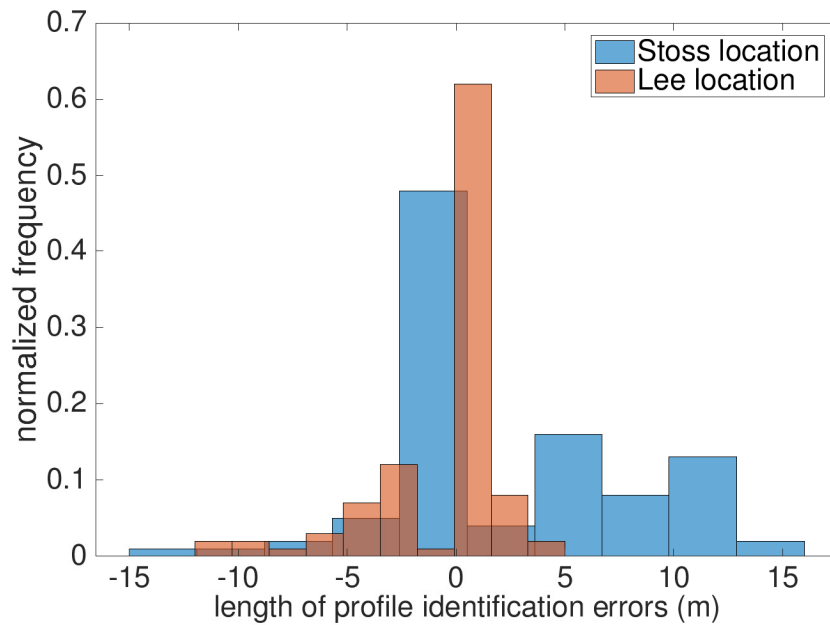
Figure 4.6: Histogram of identification errors introduced by the automated detection scheme for both the beginning of the profile stoss surface and the end of the profile lee. A positive location error of X meters indicates that the stoss/lee position is inclusive of a portion of an interdune surface. A negative location error of X meters indicates that the stoss/lee position truncates a portion of the profile relative to the dune profile selected by eye. 100 dunes were selected evenly from the 2009 and 2010 DEMs.
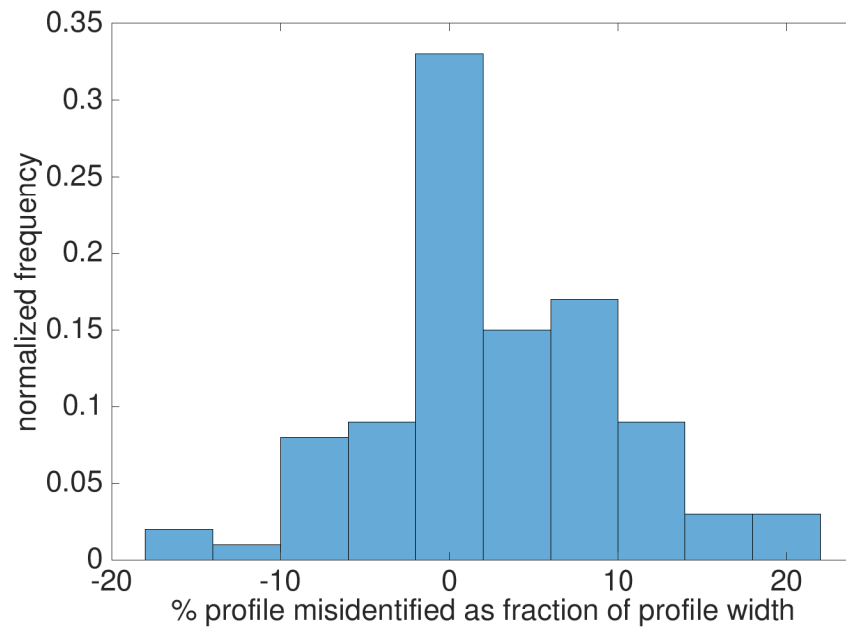
Figure 4.7: % of dune profile misidentified relative to the width of the profile. Positive percentages connote over-identification and the inclusion of interdune elevations. Negative percentages connote under-identification. The analysis here was performed for 50 dunes each from the 2009 and 2010 DEMs.
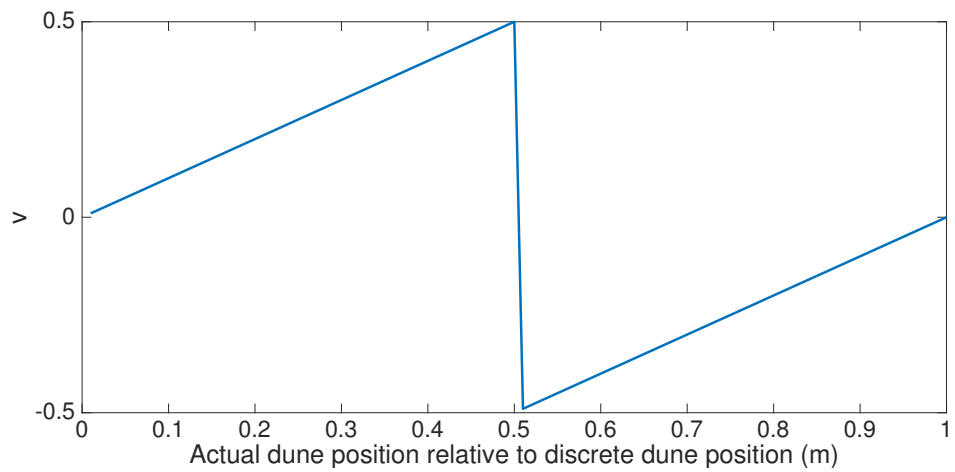
Figure 4.8: A plot of the displacement error v for an idealized dune displacement as the displacement of the dune is shifted from being 0 m away from a displacement resolved to 1m resolution to 1m away. As the real displacement approaches the meter scale values v goes to zero. v reaches a maximum magnitude of .5 m when the actual displacement is .5 m away from either meter scale value.
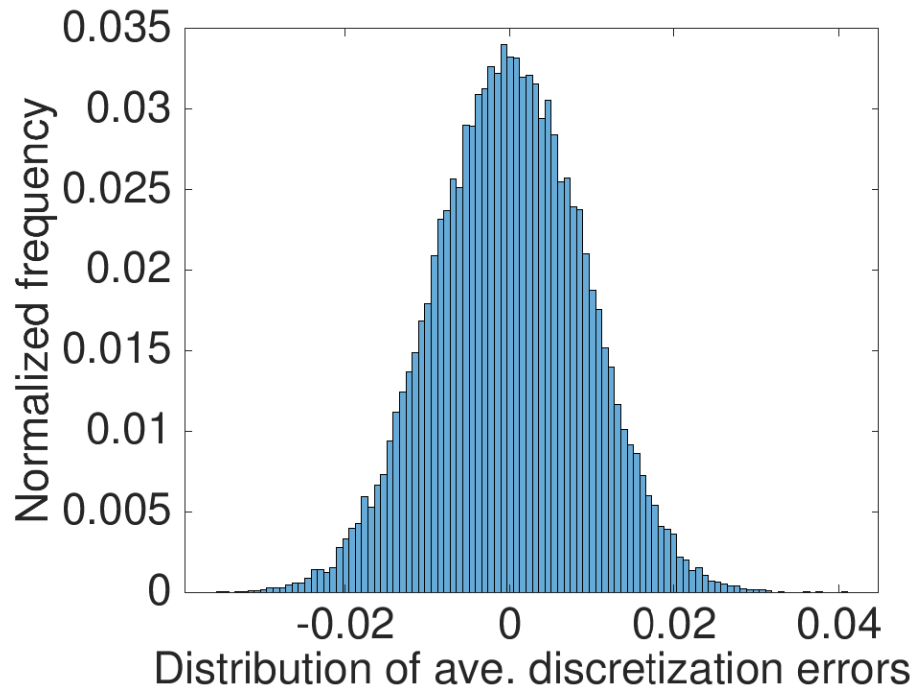
Figure 4.9: A histogram showing the frequency of different magnitudes of average error for a typical width averaged V_c value. The result was obtained by sampling 1000 times (a typical observation density for the area that V_c is averaged over) from the range discretization errors, v, associated with a single dune profile. The mean of this sample was then taken and the distribution of means plotted. The average error that results from width averaging many dune profiles together is centered around zero with the majority of the average error falling between -.015 and .015.
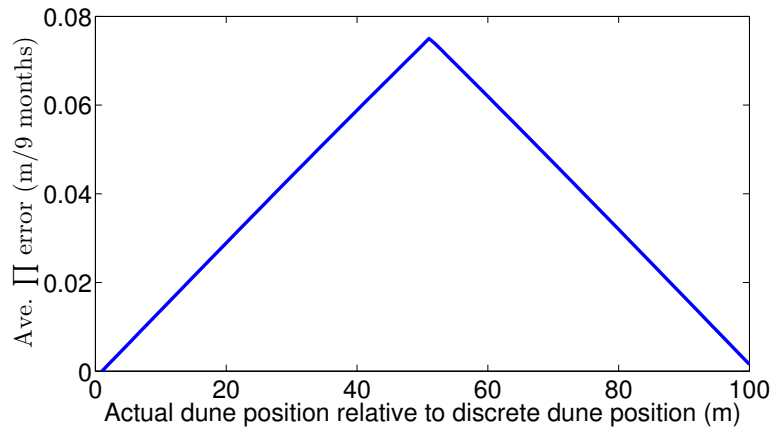
Figure 4.10: An empirical estimate of the average error caused in $|\prod|$ by discretizing V_c to a resolution of 1 m. The x-axis shows an artificially induced displacement shift of 67 dunes sampled relative to a fixed, arbitrary discrete dune displacement. For each sub-meter displacement shift, a V_c accurate to a meter is found that attempts to shift the original dune profile back onto itself. The average $|\prod|$ that results is found. All non-zero values of $|\prod|$ are introduced into the calculation by the displacement discrepancy introduced by discretization and hence any non-zero $|\prod|$ represent an error. At each shift the maximum $|\prod|$ for 67 dunes that have been artificially displaced is calculated and then averaged together. Peak error occurs at approx. .5m away from the initial position at 0m and then declines again as the actual position approaches the next resolvable position.
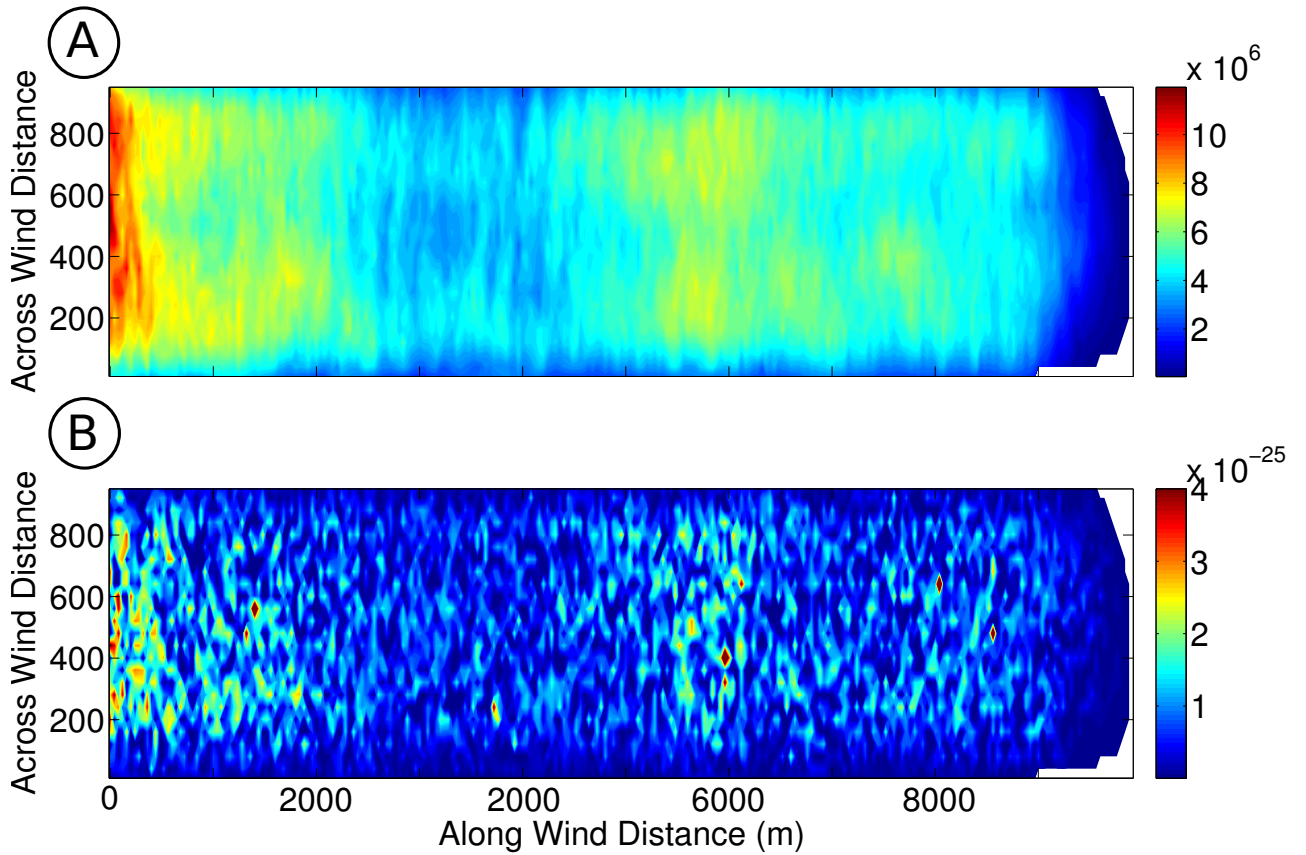
Figure 4.11: Panel A shows a map of affine strain D_{aff}. Panel B shows a map of non-affine deformation D^2_{min}. Zones of high D_{aff} appear to be associated with zones of high D^2_{min}. Transverse, barchan, and parabolic regions of dune field are demarcated by I, II, and III. Primary and secondary peaks in planform deformation are associated with the transverse-barchan and barchan-parabolic transitions, respectively.
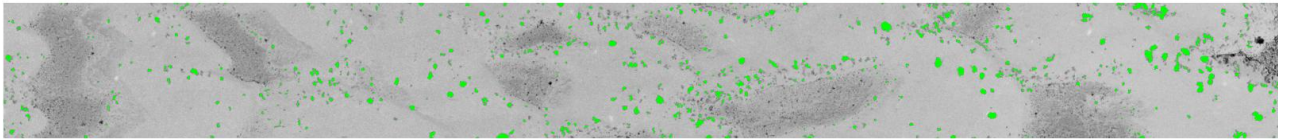
Figure 4.12: The result of the vegetation detection scheme used to calculate ρ_{veg} of dunes, which ignores inter-dune areas. Detected dune plants are shown as light green blobs. Fig. 4.13 shows a comparison of this classification method to that done by eye.
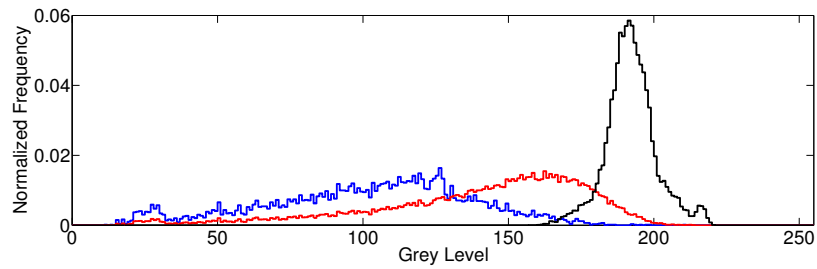
Figure 4.13: Histogram of the grey levels of the aerial images as classified by different methods of plant detection. Grey level 255 are completely white pixels and grey level 0 represents completely black. The Blue histogram shows the frequency at which different grey levels that are classified as vegetation by the automated detection code. The red histogram shows the frequency at which grey levels were classified as vegetation when the analysis was performed by eye on a set of randomly selected vegetated areas of 45m x 45m. The black histogram shows the grey levels of unvegetated portions of the dunes. Note the overlap between the unvegetated portions of the dune field and the eye detected grey levels that were classified as vegetation.
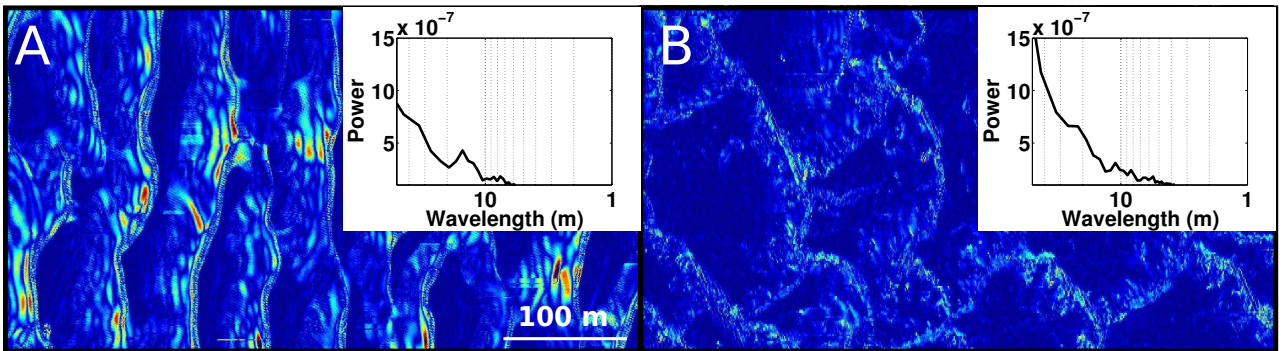
Figure 4.14: Patterns of deformation across the dune field along with spectral analysis of the deformation. (A) Laterally-coherent vertical deformation structures are seen on unvegetated dunes, by mapping $|\prod|$ for every square meter in the DEM; more examples can be seen in Fig. S2. (B) Map of $|\prod|$ for a representative parabolic region of the dune field; the absence of coherent deformation in this panel is typical for vegetated dunes. Insets in panels A and B show radially-averaged, detrended 2D power-spectral density (PSD) plots computed from representative portions of $|\prod|$ maps for a subset of the barchan and parabolic portions of the dune field, respectively. The spike in the spectral density at approx. 15m that is present in panel A is noticably absent in panel B.
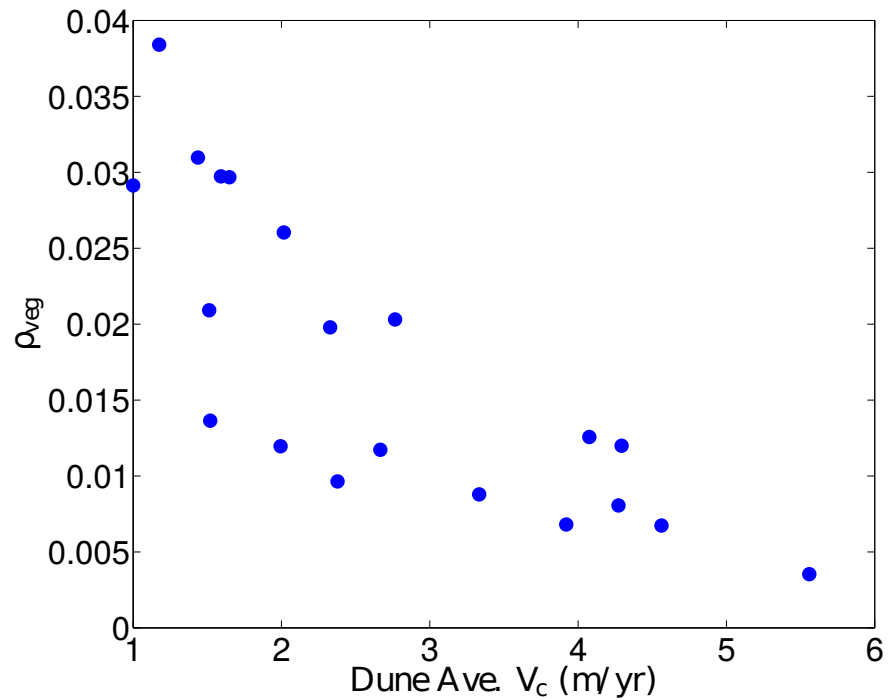
Figure 4.15: A dune-scale analysis of dune migration rate against fraction plant cover. Figure is included to illustrate the robustness of the width-averaged trends reported in the main text. Dunes were arbitrarily selected by hand from various locations in the dune field, and the V_c values of all profiles associated with each dune were then averaged together and compared to the vegetation density, ρ_{veg}, of that dune. Data roughly follow the inverse relation between V_c and ρ_{veg} observed in the width-averaged global data seen in Fig. 4.

Identified profiles	Unidentified profiles	Lumped profiles	Split profiles	Total profiles	% unidentified
65	6	1	0	72	8.3
75	7	1	3	80	8.8
64	6	0	5	65	9.2
67	4	1	2	70	5.7
61	6	1	7	61	9.8
71	5	0	6	70	7.1
67	6	1	1	73	8.2
71	3	0	2	72	4.2
64	7	1	2	70	10.0
60	8	2	2	68	11.8

Table 4.1: Dune profile classification errors for 10 random study area transects

CHAPTER 5 : Summary and Conclusions

5.1. Summary

In this dissertation, I have studied geomorphic changes of state that occur around a threshold. For each state change, the underlying physics of sediment transport has played a dominant role. Given that the chapters cover a broad range of scales, the findings emphasize the importance of physical understanding in understanding change in the landscape at all scales of interest. The work also highlights the frequency with which transport processes interact with other morphological controls to modulate both landscape expression and evolution.

At the grain scale, the threshold of motion determines the transition of grains from the approximately static state to the mobile state. Chapter 2 examined the dynamics of coarse grained sediment transport near this threshold. In particular, I characterized the growth in the intermittency of transport as this threshold is approached. I directly observe a measure of collective entrainment as transport becomes more intermittent. I find strong evidence for a length scale of collective entrainment similar to that posited by *Ancey et al.* (2008b). In my model system, distributions of collective entrainment events are invariant with regard to the mean transport frequency at which grains travel through the system. In contrast, waiting times do vary with transport frequency. As transport is lowered, average waiting times begin to deviate significantly from the naive expectation that the time between transport events is controlled by the frequency with which grains are fed into the system. This result leads us to a first order characterization of transport being dominated by collective entrainment events of a characteristic size similar to the characteristic scale of avalanches on slowly driven sandpiles (*Rajchenbach*, 1990; *Lemieux and Durian*, 2000). As the transport frequency is increased these events merge and transport becomes continuous. Once again, this behavior is analogous to the behavior of sandpiles as described by *Hwa and Kardar* (1992). I also find compelling evidence for the role of collisional momentum transfer as a

dominant driver of all entrainment in my model system (and hence collective entrainment), in agreement with recent models (*Pähtz and Durán*, 2017; *Vowinckel et al.*, 2017).

Chapter 3 was concerned with developing and testing a novel method to assess how the threshold of motion varies in the field. I corroborate previous work that has documented the relationship between a soils shear strength and the threshold of motion (*Léonard and Richard*, 2004). While previous studies focused on fully saturated, highly cohesive soils I analyze the relation between shear strength and incipient motion as the saturation state of one soil is increased. The test probe uses novel, force feedback technology which allows the gathering of surface shear strength measurements in soils which are loosely consolidated with low cohesivity. This appears to be due to the probe's ability to control its force output at high resolution at low absolute force values. I found that both my measure of surface shear strength and an estimate of the soil's threshold of motion appear to increase as the surface moisture of the soil is increased. Though the experiments were performed in the lab, my shear strength test was explicitly designed to be performable by the recently introduced semi-autonomous robotic platform described by *Qian et al.* (2017). Given that this platform has already demonstrated the ability to measure gradients in erodibility (see *Qian et al.* (in prep)), it is hoped that this test will eventually be part of a suite of tests that are each designed to measure different aspects of a soil's erosive response to perturbation.

One of the primary controls on threshold transport in the field is vegetation (*Lancaster and Baas*, 1998). Chapter 4 used the dune field at White Sands National Monument to determine feedbacks between vegetation and sediment transport. I quantified rates of dune profile migration and found further evidence supporting the role of fraction plant cover in slowing down dune kinematics. More interestingly, this approach allowed the use of dune dynamics to reveal the presence of a striped deformation pattern in the unvegetated portion of the dune field that would have been unobservable in the topography. This deformation pattern is related to the instability proposed by *Elbelrhiti et al.* (2005) to be crucial in maintaining the quasi-equilibrium state of barchan dune fields. I demonstrate that the

appearance of vegetation above a threshold level shuts off the instability. Thus vegetation not only slows down dunes but also induces a qualitative shift in transport that helps destroy the equilibrium of the dune field and encourages a shift to a parabolic dune morphology.

5.2. Implications and Future Prospects

5.2.1. Specific Implications and Future Work

This section discusses implications of the work presented in the preceding chapters as well as future work to be done. At the grain scale, the characteristic size of collective entrainment events coupled with my observation that it is the kinetic energy transfer of saltating grains with the bed that drives entrainment suggests that the impact velocity of saltating grains sets the size of collective entrainment events. The velocities of saltators will be primarily controlled by the fluid flow. Future experiments that vary the flow conditions while at low feed rates would allow the verification of this hypothesis. If correct, it would be expected that the characteristic length scale of collective entrainment would grow as flow velocity was increased. In the current experiments, the length scale of transport is larger than the grain scale and hence a non-trivial component of bedload transport. Its future incorporation into general probabilistic frameworks such as those proposed by *Furbish et al.* (2017) has the potential to improve existing models. Personal communication with Furbish has also indicated enthusiasm for incorporating the observation of saltator-bed kinetic energy transfer into future statistical mechanical models. This would imply that future work that examines the role of kinetic energy absorption by the bed due to its interaction with both turbulent structures and grain-bed collisions could improve the mechanical basis of existing models.

The successful experimental calibration of a shear strength strength test performable by a newly developed robotic platform (RHex) to a soils threshold shear stress is only the first step. Another test of the soil erodibility designed to explore the soils erosive response to mechanical disturbance has already demonstrated RHex's ability to map gradients in the

erosive response of the soil that happen concurrently with variations in soil moisture and vegetation (*Qian et al.*, in prep). A sensible next step would be to do a field campaign where the additional test developed in chapter 4 would be performed in tandem with the other erodibility test. Given the portability of the PI-SWERL, it would also be sensible to perform threshold stress measurements to confirm that the threshold still varies in proportion with the shear strength. While these measurements would have the disadvantage of not being able to isolate all the controls affecting the erodibility, it would be an additional test of the robustness of the observed relationship between shear strength and threshold shear stress. If the relationship holds, then additional deployments of RHex that take advantage of its ability to rapidly test large field areas at high spatial resolution should give us novel insight into how erodibility varies with factors such as plant density, grain size and shape, and moisture that could also be measured by RHex.

Spatially resolved, on the ground estimates of the threshold of motion could find immediate applicability towards improving my understanding of vegetation mediated shutdown of the dune instability observed in chapter 5. Knowledge of how the threshold of motion changes as vegetation grows more prevalent in the dune field would allow the estimation of what role, if any, variability in this threshold plays in slowing rates of dune migration and shutting off the duneform instability. Given that the biogeomorphic feedbacks governing the inversion of barchans into parabolics is still poorly understood, it is also possible that biologically controlled alterations in soil properties help encourage this transition (*Yan and Baas*, 2017). Other work that could build off of the observations of chapter 5 could make use of the additional years of elevation data that are available at White Sands to obtain a longer record of the dynamics of the dune field. This record might allow us to observe the ejection of new dunes formed by the observed instability from the horns of barchan dunes. This hypothesis was proposed by *Elbelrhiti et al.* (2005) as one of the ways that the instability I observe at White Sands regulates the mean size of the barchan portion of dune fields. A successful observation of these new barchans would be further confirmation of the role of this instability in modulating dune evolution at White Sands.

There is a fascinating interplay between sediment transport dynamics and larger scale landscape patterns. This thesis has sought to demonstrate that a better understanding of the mechanisms governing this interplay is crucial for understanding shifts in landscape pattern and process. Perhaps most crucially, developing a fuller understanding of the physics of grain scale processes will continue to provide insight as a statistical mechanical description of sediment transport develops. The fields of geology, geography, and environmental science are uniquely situated to benefit from the dramatic growth in the capability of semi-autonomous and autonomous terrestrial and airborne unmanned robotic platforms (*Immerzeel et al.*, 2014; *Qian et al.*, 2017). This advance should allow us to answer increasingly complex questions about how landscapes transition to a new steady state. The ever increasing availability of remote sensing data is also exciting and the results of chapter 4 highlight that the short time dynamics of landscape evolution (dynamics over the yearly to decadal scale) may contain novel information not obtainable from topography alone. As repeat LIDAR and photogrammetric surveys become more common, it will become increasingly possible to use field observations of landscape dynamics to test geomorphological theories. The increasing availability of dynamic information should also make it possible to better observe behavior near abrupt morphological changes of state (such as the dune pattern transition studied in this thesis).

BIBLIOGRAPHY

Albert, I., P. Tegzes, B. Kahng, R. Albert, J. Sample, M. Pfeifer, A.-L. Barabasi, T. Vicsek, and P. Schiffer (2000), Jamming and fluctuations in granular drag, *Physical review letters*, *84*(22), 5122.

Ancey, C., and J. Heyman (2014), A microstructural approach to bed load transport: mean behaviour and fluctuations of particle transport rates, *Journal of Fluid Mechanics*, *744*, 129–168.

Ancey, C., A. Davison, T. Böhm, M. Jodeau, and P. Frey (2008a), Entrainment and motion of coarse particles in a shallow water stream down a steep slope, *Journal of Fluid Mechanics*, *595*, 83–114.

Ancey, C., a. C. Davison, T. Böhm, M. Jodeau, and P. Frey (2008b), Entrainment and motion of coarse particles in a shallow water stream down a steep slope, *Journal of Fluid Mechanics*, *595*, 83–114, doi:10.1017/S0022112007008774.

Baas, A., and J. Nield (2007), Modelling vegetated dune landscapes, *Geophysical Research Letters*, *34*(6).

Bagnold, R. A. (1941), *The physics of wind blown sand and desert dunes*, Methuen, London.

Bagnold, R. A. (2012), *The physics of blown sand and desert dunes*, Courier Corporation.

Baitis, E., G. Kocurek, V. Smith, D. Mohrig, R. C. Ewing, and A.-P. Peyret (2014), Definition and origin of the dune-field pattern at White Sands, New Mexico, *Aeolian Research*, *15*, 269–287.

Bakker, M. M., G. Govers, A. van Doorn, F. Quetier, D. Chouvardas, and M. Rounsevell (2008), The response of soil erosion and sediment export to land-use change in four areas of Europe: the importance of landscape pattern, *Geomorphology*, *98*(3), 213–226.

Barchyn, T. E., and C. H. Hugenholtz (2012), A process-based hypothesis for the barchan–parabolic transformation and implications for dune activity modelling, *Earth Surface Processes and Landforms*, *37*(13), 1456–1462.

Barchyn, T. E., and C. H. Hugenholtz (2013), Reactivation of supply-limited dune fields from blowouts: A conceptual framework for state characterization, *Geomorphology*, *201*, 172–182.

Barchyn, T. E., and C. H. Hugenholtz (2015), Predictability of dune activity in real dune fields under unidirectional wind regimes, *Journal of Geophysical Research: Earth Surface*, *120*(2), 159–182.

Barnocky, G., and R. H. Davis (1988), Elastohydrodynamic collision and rebound of spheres: experimental verification, *The Physics of fluids*, *31*(6), 1324–1329.

Belnap, J., and D. A. Gillette (1998), Vulnerability of desert biological soil crusts to wind erosion: the influences of crust development, soil texture, and disturbance, *Journal of arid environments*, *39*(2), 133–142.

Bisal, F., and J. Hsieh (1966), Influence of moisture on erodibility of soil by wind., *Soil Science*, *102*(3), 143–146.

Bishop, P. (2007), Long-term landscape evolution: linking tectonics and surface processes, *Earth Surface Processes and Landforms*, *32*(3), 329–365.

Bolte, K., P. Hartmann, H. Fleige, and R. Horn (2011), Determination of critical soil water content and matric potential for wind erosion, *Journal of soils and sediments*, *11*(2), 209–220.

Braudrick, C. A., W. E. Dietrich, G. T. Leverich, and L. S. Sklar (2009), Experimental evidence for the conditions necessary to sustain meandering in coarse-bedded rivers, *Proceedings of the National Academy of Sciences*, *106*(40), 16936–16941.

Brunsden, D., and J. Thornes (1979), Landscape sensitivity and change, *Transactions of the Institute of British Geographers*, pp. 463–484.

Cakmur, R., R. Miller, J. Perlwitz, I. Geogdzhayev, P. Ginoux, D. Koch, K. Kohfeld, I. Tegen, and C. Zender (2006), Constraining the magnitude of the global dust cycle by minimizing the difference between a model and observations, *Journal of Geophysical Research: Atmospheres*, *111*(D6).

Celik, I. (2005), Land-use effects on organic matter and physical properties of soil in a southern Mediterranean highland of Turkey, *Soil and Tillage Research*, *83*(2), 270–277.

Charru, F., H. Mouilleron, and O. Eiff (2004), Erosion and deposition of particles on a bed sheared by a viscous flow, *Journal of Fluid Mechanics*, *519*, 55–80.

Chepil, W. (1956), Influence of Moisture on Erodibility of Soil by Wind1, *Soil Science Society of America Journal*, *20*(2), 288–292.

Corenblit, D., et al. (2011), Feedbacks between geomorphology and biota controlling Earth surface processes and landforms: a review of foundation concepts and current understandings, *Earth-Science Reviews*, *106*(3), 307–331.

Cornelis, W., and D. Gabriels (2003), The effect of surface moisture on the entrainment of dune sand by wind: an evaluation of selected models, *Sedimentology*, *50*(4), 771–790.

Crocker, J., J. Crocker, and D. Grier (1996), Methods of Digital Video Microscopy for Colloidal Studies, *Journal of Colloid and Interface Science*, *179*(1), 298–310, doi:10.1006/jcis.1996.0217.

Dade, W. B., and P. F. Friend (1998), Grain-size, sediment-transport regime, and channel slope in alluvial rivers, *The Journal of Geology*, *106*(6), 661–676.

Dai, A. (2013), Increasing drought under global warming in observations and models, *Nature Climate Change*, *3*(1), 52–58.

Dietrich, W. E., and J. T. Perron (2006), The search for a topographic signature of life, *Nature*, *439*(7075), 411–418.

Dinehart, R. L. (1999), Correlative velocity fluctuations over a gravel river bed, *Water Resources Research*, *35*(2), 569–582.

Diplas, P., C. L. Dancey, A. O. Celik, M. Valyrakis, K. Greer, and T. Akar (2008), The role of impulse on the initiation of particle movement under turbulent flow conditions., *Science (New York, N.Y.)*, *322*(5902), 717–20, doi:10.1126/science.1158954.

Drake, T. G., R. L. Shreve, W. E. Dietrich, P. J. Whiting, and L. B. Leopold (1988), Bedload transport of fine gravel observed by motion-picture photography, *Journal of Fluid Mechanics*, *192*, 193–217.

Dregne, H. E., and N.-T. Chou (1992), Global desertification dimensions and costs, *Degradation and restoration of arid lands*, pp. 73–92.

Durán, O., and H. Herrmann (2006a), Modelling of saturated sand flux, *Journal of Statistical Mechanics: Theory and Experiment*, *2006*(07), P07011.

Durán, O., and H. J. Herrmann (2006b), Vegetation against dune mobility, *Physical Review Letters*, *97*(18), 188001.

Durán, O., and L. J. Moore (2013), Vegetation controls on the maximum size of coastal dunes, *Proceedings of the National Academy of Sciences*, *110*(43), 17217–17222.

Durán, O., P. Claudin, and B. Andreotti (2011), On aeolian transport: Grain-scale interactions, dynamical mechanisms and scaling laws, *Aeolian Research*, *3*(3), 243–270.

Einstein, H. A. (1950), The Bed-Load Function for Sediment Transportation in Open Channel Flows, *Soil Conservation Service*, (1026), 1–31.

Elbelrhiti, H., P. Claudin, and B. Andreotti (2005), Field evidence for surface-wave-induced instability of sand dunes, *Nature*, *437*(7059), 720–723.

Elbelrhiti, H., B. Andreotti, and P. Claudin (2008), Barchan dune corridors: field characterization and investigation of control parameters, *Journal of Geophysical Research: Earth Surface*, *113*(F2).

Etyemezian, V., G. Nikolich, S. Ahonen, M. Pitchford, M. Sweeney, R. Purcell, J. Gillies, and H. Kuhns (2007), The Portable In Situ Wind Erosion Laboratory (PI-SWERL): A new method to measure PM 10 windblown dust properties and potential for emissions, *Atmospheric Environment*, *41*(18), 3789–3796.

Ewing, R. C., and G. A. Kocurek (2010), Aeolian dune interactions and dune-field pattern formation: White Sands Dune Field, New Mexico, *Sedimentology*, *57*(5), 1199–1219.

Falk, M., and J. Langer (1998), Dynamics of viscoplastic deformation in amorphous solids, *Physical Review E*, *57*(6), 7192.

Fang, H., Q. Shang, M. Chen, and G. He (2014), Changes in the critical erosion velocity for sediment colonized by biofilm, *Sedimentology*, *61*(3), 648–659.

Fathel, S., D. Furbish, and M. Schmeeckle (2016), Parsing anomalous versus normal diffusive behavior of bedload sediment particles, *Earth Surface Processes and Landforms*, *41*(12), 1797–1803.

Fécan, F., B. Marticorena, and G. Bergametti (1998), Parametrization of the increase of the aeolian erosion threshold wind friction velocity due to soil moisture for arid and semi-arid areas, in *Annales Geophysicae*, vol. 17, pp. 149–157, Springer.

Frette, V., K. Christensen, A. Malthe-Sorenssen, J. Feder, et al. (1996), Avalanche dynamics in a pile of rice, *Nature*, *379*(6560), 49.

Frey, P., and M. Church (2011a), Bedload: a granular phenomenon, *Earth Surface Processes and Landforms*, *36*(1), 58–69, doi:10.1002/esp.2103.

Frey, P., and M. Church (2011b), Bedload: a granular phenomenon, *Earth Surface Processes and Landforms*, *36*(1), 58–69.

Furbish, D. J., P. K. Haff, J. C. Roseberry, and M. W. Schmeeckle (2012), A probabilistic description of the bed load sediment flux: 1. Theory, *Journal of Geophysical Research: Earth Surface*, *117*(F3).

Furbish, D. J., S. L. Fathel, M. W. Schmeeckle, D. J. Jerolmack, and R. Schumer (2017), The elements and richness of particle diffusion during sediment transport at small timescales, *Earth Surface Processes and Landforms*, *42*(1), 214–237.

Ganti, V., M. M. Meerschaert, E. Foufoula-Georgiou, E. Viparelli, and G. Parker (2010), Normal and anomalous diffusion of gravel tracer particles in rivers, *Journal of Geophysical Research: Earth Surface*, *115*(F2).

Gillette, D. (1978), Tests with a portable wind tunnel for determining wind erosion threshold velocities, *Atmospheric Environment (1967)*, *12*(12), 2309–2313.

Gillette, D. A., J. Adams, A. Endo, D. Smith, and R. Kihl (1980), Threshold velocities for input of soil particles into the air by desert soils, *Journal of Geophysical Research: Oceans*, *85*(C10), 5621–5630.

Gomez, B., and J. D. Phillips (1999), Deterministic uncertainty in bed load transport, *Journal of Hydraulic Engineering*, *125*(3), 305–308.

Goossens, D., and B. Buck (2009), Dust dynamics in off-road vehicle trails: measurements on 16 arid soil types, Nevada, USA, *Journal of Environmental Management*, *90*(11), 3458–3469.

Goudie, A., and N. Middleton (2001), Saharan dust storms: nature and consequences, *Earth-Science Reviews*, *56*(1), 179–204.

Goudie, A. S. (2014), Desert dust and human health disorders, *Environment international*, *63*, 101–113.

Gran, K., and C. Paola (2001), Riparian vegetation controls on braided stream dynamics, *Water Resources Research*, *37*(12), 3275–3283.

Gravish, N., and D. I. Goldman (2014), Effect of volume fraction on granular avalanche dynamics, *Physical Review E*, *90*(3), 032202.

Hack, J. T. (1975), Dynamic equilibrium and landscape evolution, *Theories of landform development*, *1*, 87–102.

Hersen, P., and S. Douady (2005), Collision of barchan dunes as a mechanism of size regulation, *Geophysical Research Letters*, *32*(21).

Heyman, J., F. Mettra, H. Ma, and C. Ancey (2013), Statistics of bedload transport over steep slopes: Separation of time scales and collective motion, *Geophysical Research Letters*, *40*(1), 128–133.

Heyman, J., H. Ma, F. Mettra, and C. Ancey (2014), Spatial correlations in bed load transport: Evidence, importance, and modeling, *Journal of Geophysical Research: Earth Surface*, *119*(8), 1751–1767.

Hoffmann, C., R. Funk, R. Wieland, Y. Li, and M. Sommer (2008), Effects of grazing and topography on dust flux and deposition in the Xilingele grassland, Inner Mongolia, *Journal of arid environments*, *72*(5), 792–807.

Houssais, M., C. P. Ortiz, D. J. Durian, and D. J. Jerolmack (2015), Onset of sediment transport is a continuous transition driven by fluid shear and granular creep, *Nature communications*, *6*.

Houssais, M., C. P. Ortiz, D. J. Durian, and D. J. Jerolmack (2016), Rheology of sediment transported by a laminar flow, *Physical Review E*, *94*(6), 062609.

Hwa, T., and M. Kardar (1992), Avalanches, hydrodynamics, and discharge events in models of sandpiles, *Physical Review A*, *45*(10), 7002.

Hyvärinen, A., and E. Oja (2000), Independent component analysis: algorithms and applications, *Neural networks*, *13*(4), 411–430.

Immerzeel, W., P. Kraaijenbrink, J. Shea, A. Shrestha, F. Pellicciotti, M. Bierkens, and S. De Jong (2014), High-resolution monitoring of Himalayan glacier dynamics using unmanned aerial vehicles, *Remote Sensing of Environment*, *150*, 93–103.

Jackson, N. L., and K. F. Nordstrom (1997), Effects of Time-dependent Moisture Content of Surface Sediments on Aeolian Transport Rates Across a Beach, Wildwood, New Jersey, USA, *Earth Surface Processes and Landforms*, *22*(7), 611–621.

Jerolmack, D. J., and T. A. Brzinski (2010), Equivalence of abrupt grain-size transitions in alluvial rivers and eolian sand seas: A hypothesis, *Geology*, *38*(8), 719–722.

Jerolmack, D. J., M. D. Reitz, and R. L. Martin (2011), Sorting out abrasion in a gypsum dune field, *Journal of Geophysical Research: Earth Surface*, *116*(F2).

Jerolmack, D. J., R. C. Ewing, F. Falcini, R. L. Martin, C. Masteller, C. Phillips, M. D. Reitz, and I. Buynevich (2012), Internal boundary layer model for the evolution of desert dune fields, *Nature Geoscience*, *5*(3), 206–209.

Kenneally, G., A. De, and D. E. Koditschek (2016), Design principles for a family of direct-drive legged robots, *IEEE Robotics and Automation Letters*, *1*(2), 900–907.

Keys, A. S., A. R. Abate, S. C. Glotzer, and D. J. Durian (2007), Measurement of growing dynamical length scales and prediction of the jamming transition in a granular material, *Nature physics*, *3*(4), 260–264.

Khan, H. A., and G. M. Maruf (2013), Counting clustered cells using distance mapping, *2013 International Conference on Informatics, Electronics and Vision, ICIEV 2013*, doi: 10.1109/ICIEV.2013.6572677.

Kimiaghalam, N., S. P. Clark, and H. Ahmari (2016), An experimental study on the effects of physical, mechanical, and electrochemical properties of natural cohesive soils on critical shear stress and erosion rate, *International Journal of Sediment Research*, *31*(1), 1–15.

Kimura, R., and M. Shinoda (2010), Spatial distribution of threshold wind speeds for dust outbreaks in northeast Asia, *Geomorphology*, *114*(3), 319–325.

Kocurek, G., and R. C. Ewing (2005), Aeolian dune field self-organization–implications for the formation of simple versus complex dune-field patterns, *Geomorphology*, *72*(1), 94–105.

Kocurek, G., M. Carr, R. Ewing, K. G. Havholm, Y. Nagar, and A. Singhvi (2007), White Sands Dune Field, New Mexico: age, dune dynamics and recent accumulations, *Sedimentary Geology*, *197*(3), 313–331.

Kok, J., et al. (2014), An improved dust emission model–Part 1: Model description and comparison against measurements, *Atmospheric Chemistry and Physics*, *14*(23), 13023–13041.

Kutiel, P., H. Zhevelev, and R. Harrison (1999), The effect of recreational impacts on soil and vegetation of stabilised coastal dunes in the Sharon Park, Israel, *Ocean & Coastal Management*, *42*(12), 1041–1060.

Lancaster, N., and A. Baas (1998), Influence of vegetation cover on sand transport by wind: field studies at Owens Lake, California, *Earth Surface Processes and Landforms*, *23*(1), 69–82.

Langford, R. P. (2003), The Holocene history of the White Sands dune field and influences on eolian deflation and playa lakes, *Quaternary International*, *104*(1), 31–39.

Larsen, L. G., and J. W. Harvey (2010), How vegetation and sediment transport feedbacks drive landscape change in the Everglades and wetlands worldwide, *The American Naturalist*, *176*(3), E66–E79.

Lawler, G. F., and V. Limic (2010), *Random walk: a modern introduction*, vol. 123, Cambridge University Press.

Lemieux, P.-A., and D. Durian (2000), From avalanches to fluid flow: A continuous picture of grain dynamics down a heap, *Physical Review Letters*, *85*(20), 4273.

Léonard, J., and G. Richard (2004), Estimation of runoff critical shear stress for soil erosion from soil shear strength, *Catena*, *57*(3), 233–249.

Liddle, M., and P. Grieg-Smith (1975), A survey of tracks and paths in a sand dune ecosystem. II. Vegetation, *Journal of Applied Ecology*, pp. 909–930.

Liu, A. J., and S. R. Nagel (2010), The jamming transition and the marginally jammed solid, *Annu. Rev. Condens. Matter Phys.*, *1*(1), 347–369.

Loye-Pilot, M., J. Martin, and J. Morelli (1986), Influence of Saharan dust on the rain acidity and atmospheric input to the Mediterranean, *Nature*, *321*(6068), 427–428.

Lu, N., B. Wu, and C. P. Tan (2007), Tensile strength characteristics of unsaturated sands, *Journal of Geotechnical and Geoenvironmental Engineering*, *133*(2), 144–154.

Ma, H., J. Heyman, X. Fu, F. Mettra, C. Ancey, and G. Parker (2014), Bed load transport over a broad range of timescales: Determination of three regimes of fluctuations, *Journal of Geophysical Research: Earth Surface*, *119*(12), 2653–2673.

Macpherson, T., W. G. Nickling, J. A. Gillies, and V. Etyemezian (2008), Dust emissions from undisturbed and disturbed supply-limited desert surfaces, *Journal of Geophysical Research: Earth Surface*, *113*(F2).

Mariotti, G., F. Falcini, N. Geleynse, M. Guala, T. Sun, and S. Fagherazzi (2013), Sediment eddy diffusivity in meandering turbulent jets: Implications for levee formation at river mouths, *Journal of Geophysical Research: Earth Surface*, *118*(3), 1908–1920.

Martin, R. L., and J. F. Kok (2016), Field measurements demonstrate distinct initiation and cessation thresholds governing aeolian sediment transport flux, *arXiv preprint arXiv:1610.10059.*

Martin, R. L., D. J. Jerolmack, and R. Schumer (2012), The physical basis for anomalous diffusion in bed load transport, *Journal of Geophysical Research: Earth Surface*, *117*(F1).

Martin, R. L., P. K. Purohit, and D. J. Jerolmack (2014), Sedimentary bed evolution as a mean-reverting random walk: Implications for tracer statistics, *Geophysical Research Letters*, *41*(17), 6152–6159.

Maurin, R., J. Chauchat, and P. Frey (2016), Dense granular flow rheology in turbulent bedload transport, *Journal of Fluid Mechanics*, *804*, 490–512.

McElroy, B., and D. Mohrig (2009), Nature of deformation of sandy bed forms, *Journal of Geophysical Research: Earth Surface*, *114*(F3).

McKenna-Neuman, C., and W. Nickling (1989), A theoretical and wind tunnel investigation of the effect of capillary water on the entrainment of sediment by wind, *Canadian Journal of Soil Science*, *69*(1), 79–96.

Meng, X.-m., Y.-g. Jia, H.-x. Shan, Z.-n. Yang, and J.-w. Zheng (2012), An experimental study on erodibility of intertidal sediments in the Yellow River delta, *International Journal of Sediment Research*, *27*(2), 240–249.

Nadler, C., and S. Schumm (1981), Metamorphosis of South Platte and Arkansas Rivers, eastern Colorado, *Physical Geography*, *2*(2), 95–115.

Neff, J., et al. (2008), Increasing eolian dust deposition in the western United States linked to human activity, *Nature Geoscience*, *1*(3), 189–195.

Nelson, J. M., R. L. Shreve, S. R. McLean, and T. G. Drake (1995), Role of near-bed turbulence structure in bed load transport and bed form mechanics, *Water resources research*, *31*(8), 2071–2086.

Nikora, V., H. Habersack, T. Huber, and I. McEwan (2002), On bed particle diffusion in gravel bed flows under weak bed load transport, *Water Resources Research*, *38*(6).

Okin, G., D. Gillette, and J. Herrick (2006), Multi-scale controls on and consequences of aeolian processes in landscape change in arid and semi-arid environments, *Journal of Arid Environments*, *65*(2), 253–275.

Pähtz, T., and O. Durán (), The cessation of non-suspended sediment transport across environments, *arXiv preprint arXiv: 1602.07079.*

Pähtz, T., and O. Durán (2017), Fluid forces or impacts: What governs the entrainment of soil particles in sediment transport mediated by a Newtonian fluid?, *Physical Review Fluids*, *2*(7), 074303.

Papanicolaou, A., P. Diplas, C. Dancey, and M. Balakrishnan (2001), Surface roughness effects in near-bed turbulence: Implications to sediment entrainment, *Journal of Engineering Mechanics*, *127*(3), 211–218.

Papanicolaou, A. T. N., D. Knapp, and K. Strom (2002), Bedload predictions by using the concept of particle velocity: Applications, in *Hydraulic Measurements and Experimental Methods 2002*, pp. 1–10.

Parker, G., P. R. Wilcock, C. Paola, W. E. Dietrich, and J. Pitlick (2007), Physical basis for quasi-universal relations describing bankfull hydraulic geometry of single-thread gravel bed rivers, *Journal of Geophysical Research: Earth Surface (2003–2012)*, *112*(F4).

Parteli, E. J., J. S. Andrade Jr, and H. J. Herrmann (2011), Transverse instability of dunes, *Physical review letters*, *107*(18), 188001.

Parthasarathy, R. (2012), Rapid, accurate particle tracking by calculation of radial symmetry centers, doi:10.1038/nmeth.2071.

Pedersen, A., G. Kocurek, D. Mohrig, and V. Smith (2015), Dune deformation in a multidirectional wind regime: White Sands Dune Field, New Mexico, *Earth Surface Processes and Landforms*, *40*(7), 925–941.

Pelletier, J. D. (2015), Controls on the large-scale spatial variations of dune field properties in the barchanoid portion of White Sands dune field, New Mexico, *Journal of Geophysical Research: Earth Surface*, *120*(3), 453–473.

Pelletier, J. D., H. Mitasova, R. S. Harmon, and M. Overton (2009), The effects of interdune vegetation changes on eolian dune field evolution: a numerical-modeling case study at Jockey's Ridge, North Carolina, USA, *Earth Surface Processes and Landforms*, *34*(9), 1245–1254.

Phillips, C. B., and D. J. Jerolmack (2016), Self-organization of river channels as a critical filter on climate signals, *Science*, *352*(6286), 694–697.

Phillips, C. B., R. L. Martin, and D. J. Jerolmack (2013), Impulse framework for unsteady flows reveals superdiffusive bed load transport, *Geophysical Research Letters*, *40*(7), 1328–1333, doi:10.1002/grl.50323.

Phillips, J. D., and C. Van Dyke (2017), State-and-transition models in geomorphology, *Catena*, *153*, 168–181.

Ping, L., C. Narteau, Z. Dong, Z. Zhang, and S. C. du Pont (2014), Emergence of oblique dunes in a landscape-scale experiment, *Nature Geoscience*, *7*(2), 99–103.

Prancevic, J. P., and M. P. Lamb (2015), Unraveling bed slope from relative roughness in initial sediment motion, *Journal of Geophysical Research: Earth Surface*, *120*(3), 474–489.

Qian, F., et al. (2017), Ground robotic measurement of aeolian processes, *Aeolian Research*, *27*, 1–11.

Qian, F., D. Lee, D. Koditschek, and D. Jerolmack (in prep), Rapid characterization of soil erodibility with a field deployable robot, *Journal of Geophysical Research: Earth Surface*.

Rajchenbach, J. (1990), Flow in powders: From discrete avalanches to continuous regime, *Physical Review Letters*, *65*(18), 2221.

Recking, A. (2010), A comparison between flume and field bed load transport data and consequences for surface-based bed load transport prediction, *Water Resources Research*, *46*(3).

Regev, I., T. Lookman, and C. Reichhardt (2013), Onset of irreversibility and chaos in amorphous solids under periodic shear, *Physical Review E*, *88*(6), 062401.

Reich, P., S. Numbem, R. Almaraz, and H. Eswaran (2001), Land resource stresses and desertification in Africa, *Agro-Science*, *2*(2).

Reinhardt, L., D. Jerolmack, B. J. Cardinale, V. Vanacker, and J. Wright (2010), Dynamic interactions of life and its landscape: feedbacks at the interface of geomorphology and ecology, *Earth Surface Processes and Landforms*, *35*(1), 78–101.

Reitz, M. D., D. J. Jerolmack, R. C. Ewing, and R. L. Martin (2010), Barchan-parabolic dune pattern transition from vegetation stability threshold, *Geophysical Research Letters*, *37*(19).

Richard, P., M. Nicodemi, R. Delannay, P. Ribiere, and D. Bideau (2005), Slow relaxation and compaction of granular systems, *Nature materials*, *4*(2), 121–128.

Roberts, S., J. Duperret, A. M. Johnson, S. van Pelt, T. Zobeck, N. Lancaster, and D. E. Koditschek (2014a), Desert RHex Technical Report: Jornada and White Sands Trip, in *University of Pennsylvania Technical Report*.

Roberts, S. F., J. M. Duperret, X. Li, H. Wang, and D. Koditschek (2014b), Desert RHex Technical Report: Tengger Desert Trip, in *University of Pennsylvania Technical Report*.

Rosenfeld, D., Y. Rudich, and R. Lahav (2001), Desert dust suppressing precipitation: A possible desertification feedback loop, *Proceedings of the National Academy of Sciences*, *98*(11), 5975–5980.

Ruzanski, E. (2011), Radially averaged power spectrum of 2D real-valued matrix, [Online; accessed 28-February-2017; https://www.mathworks.com/matlabcentral/fileexchange/23636-radially-averaged-power-spectrum-of-2d-real-valued-matrix].

Scheel, M., R. Seemann, M. Brinkmann, M. Di Michiel, A. Sheppard, B. Breidenbach,

and S. Herminghaus (2008), Morphological clues to wet granular pile stability, *Nature Materials*, *7*(3), 189.

Schlesinger, W. H., J. F. Reynolds, G. L. Cunningham, L. F. Huenneke, W. M. Jarrell, R. A. Virginia, W. G. Whitford, et al. (1990), Biological feedbacks in global desertification., *Science(Washington)*, *247*(4946), 1043–1048.

Schmeeckle, M. W., and J. M. Nelson (2003), Direct numerical simulation of bedload transport using a local, dynamic boundary condition, *Sedimentology*, *50*(2), 279–301.

Schmeeckle, M. W., J. M. Nelson, J. Pitlick, J. P. Bennett, and A. Elastohydrodynamic (2001), Interparticle collision of natural sediment grains in water, *37*(9), 2377–2391.

Schubert, H. (1975), Tensile strength of agglomerates, *Powder Technology*, *11*(2), 107–119.

Schumm, S. A. (1979), Geomorphic thresholds: the concept and its applications, *Transactions of the Institute of British Geographers*, pp. 485–515.

Schumm, S. A. (1985), Patterns of alluvial rivers, *Annual Review of Earth and Planetary Sciences*, *13*(1), 5–27.

Sengar, R. S., A. K. Upadhyay, M. Singh, and V. M. Gadre (2016), Analysis of 2D-gel images for detection of protein spots using a novel non-separable wavelet based method, *Biomedical Signal Processing and Control*, *25*, 62–75.

Shao, Y., M. Raupach, and P. Findlater (1993), Effect of saltation bombardment on the entrainment of dust by wind, *Journal of Geophysical Research: Atmospheres*, *98*(D7), 12719–12726.

Singh, A., K. Fienberg, D. J. Jerolmack, J. Marr, and E. Foufoula-Georgiou (2009), Experimental evidence for statistical scaling and intermittency in sediment transport rates, *Journal of Geophysical Research*, *114*(F1), F01025, doi:10.1029/2007JF000963.

Stark, C. P., E. Foufoula-Georgiou, and V. Ganti (2009), A nonlocal theory of sediment buffering and bedrock channel evolution, *Journal of Geophysical Research: Earth Surface*, *114*(F1).

Stout, J. E. (2007), Simultaneous observations of the critical aeolian threshold of two surfaces, *Geomorphology*, *85*(1-2), 3–16.

Sumer, B. M., L. H. Chua, N.-S. Cheng, and J. Fredsøe (2003), Influence of turbulence on bed load sediment transport, *Journal of Hydraulic Engineering*, *129*(8), 585–596.

Sweeney, M., V. Etyemezian, T. Macpherson, W. Nickling, J. Gillies, G. Nikolich, and E. McDonald (2008), Comparison of PI-SWERL with dust emission measurements from a straight-line field wind tunnel, *Journal of Geophysical Research: Earth Surface*, *113*(F1).

Tal, M., and C. Paola (2007), Dynamic single-thread channels maintained by the interaction of flow and vegetation, *Geology*, *35*(4), 347–350.

Tucker, G. E., and D. N. Bradley (2010), Trouble with diffusion: Reassessing hillslope erosion laws with a particle-based model, *Journal of Geophysical Research: Earth Surface*, *115*(F1).

Utter, B., and R. Behringer (2008), Experimental measures of affine and nonaffine deformation in granular shear, *Physical review letters*, *100*(20), 208302.

Van Pelt, R., T. Zobeck, M. Baddock, and J. Cox (2010), Design, construction, and calibration of a portable boundary layer wind tunnel for field use, *Transactions of the ASABE*, *53*(5), 1413–1422.

Voller, V., and C. Paola (2010), Can anomalous diffusion describe depositional fluvial profiles?, *Journal of Geophysical Research: Earth Surface*, *115*(F2).

Vowinckel, B., V. Nikora, T. Kempe, and J. Fröhlich (2017), Momentum balance in flows over mobile granular beds: application of double-averaging methodology to DNS data, *Journal of Hydraulic Research*, *55*(2), 190–207.

Vrieling, A. (2006), Satellite remote sensing for water erosion assessment: A review, *Catena*, *65*(1), 2–18.

Waldron, L. (1977), The shear resistance of root-permeated homogeneous and stratified soil, *Soil Science Society of America Journal*, *41*(5), 843–849.

Watanabe, M., et al. (2011), Correlation between Asian dust storms and worsening asthma in Western Japan, *Allergology International*, *60*(3), 267–275.

Weaver, C. M., and G. F. Wiggs (2011), Field measurements of mean and turbulent airflow over a barchan sand dune, *Geomorphology*, *128*(1-2), 32–41.

Webb, N. P., and C. L. Strong (2011), Soil erodibility dynamics and its representation for wind erosion and dust emission models, *Aeolian Research*, *3*(2), 165–179.

Webb, R. H. (1983), Compaction of desert soils by off-road vehicles, in *Environmental effects of off-road vehicles*, pp. 51–79, Springer.

Webb, R. H., and H. G. Wilshire (2012), *Environmental effects of off-road vehicles: impacts and management in arid regions*, Springer Science & Business Media.

Wiggs, G., A. Baird, and R. Atherton (2004), The dynamic effects of moisture on the entrainment and transport of sand by wind, *Geomorphology*, *59*(1-4), 13–30.

Willett, S. D., and M. T. Brandon (2002), On steady states in mountain belts, *Geology*, *30*(2), 175–178.

Wolfe, S., and W. Nickling (1996), Shear stress partitioning in sparsely vegetated desert canopies, *Earth Surface Processes and Landforms*, *21*(7), 607–619.

Wolfe, S. A., and W. G. Nickling (1993), The protective role of sparse vegetation in wind erosion, *Progress in physical geography*, *17*(1), 50–68.

Wu, B., and L. J. Ci (2002), Landscape change and desertification development in the Mu Us Sandland, Northern China, *Journal of Arid Environments*, *50*(3), 429–444.

Wyatt, V., and W. Nickiing (1997), Drag and shear stress partitioning in sparse desert creosote communities, *Canadian Journal of Earth Sciences*, *34*(11), 1486–1498.

Xia, J., and P. Dong (2016), A GIS add-in for automated measurement of sand dune migration using LiDAR-derived multitemporal and high-resolution digital elevation models, *Geosphere*, *12*(4), 1316–1322.

Yager, E., J. Kirchner, and W. Dietrich (2007), Calculating bed load transport in steep boulder bed channels, *Water Resources Research*, *43*(7).

Yan, N., and A. C. Baas (2015), Parabolic dunes and their transformations under environmental and climatic changes: Towards a conceptual framework for understanding and prediction, *Global and Planetary Change*, *124*, 123–148.

Yan, N., and A. C. Baas (2017), Environmental controls, morphodynamic processes, and ecogeomorphic interactions of barchan to parabolic dune transformations, *Geomorphology*, *278*, 209–237.

Yang, D., S. Kanae, T. Oki, T. Koike, and K. Musiake (2003), Global potential soil erosion with reference to land use and climate changes, *Hydrological processes*, *17*(14), 2913–2928.

Yong-Zhong, S., L. Yu-Lin, C. Jian-Yuan, and Z. Wen-Zhi (2005), Influences of continuous grazing and livestock exclusion on soil properties in a degraded sandy grassland, Inner Mongolia, northern China, *Catena*, *59*(3), 267–278.

Zender, C. S., H. Bian, and D. Newman (2003), Mineral Dust Entrainment and Deposition (DEAD) model: Description and 1990s dust climatology, *Journal of Geophysical Research: Atmospheres*, *108*(D14).

INDEX